

Stony Brook University



OFFICIAL COPY

The official electronic file of this thesis or dissertation is maintained by the University Libraries on behalf of The Graduate School at Stony Brook University.

© All Rights Reserved by Author.

3D Shape Measurement Based on the Phase Shifting and Stereovision

Methods

A Dissertation Presented

by

Xu Han

to

The Graduate School

in Partial fulfillment of the

Requirements

for the Degree of

Doctor of Philosophy

in

Mechanical Engineering

Stony Brook University

August 2010

Copyright by
Xu Han
2010

Stony Brook University

The Graduate School

Xu Han

We, the dissertation Committee for the above candidate for the Doctor of Philosophy degree, hereby recommend acceptance of this dissertation.

Dr. Peisen Huang, Advisor
Professor, Department of Mechanical Engineering

Dr. Jeffrey Q. Ge, Chairman
Professor, Department of Mechanical Engineering

Dr. Yu Zhou, Member
Assistant Professor, Department of Mechanical Engineering

Dr. Hong Qin, Outside Member
Professor, Department of Computer Science

This dissertation is accepted by the Graduate School.

Lawrence Martin
Dean of the Graduate School

Abstract of the Dissertation

**3D Shape Measurement Based on the Phase shifting and Stereovision
Methods**

By

Xu Han

Doctor of Philosophy

in

Mechanical Engineering

Stony Brook University

2010

Structured light systems have been used in increasingly more applications for 3D shape measurement due to their fast measurement speed, good accuracy, non-contact characteristic, and portability. This dissertation is focused on improving the performance of the 3D shape measurement systems based on digital fringe projection, phase shifting and stereovision techniques. New camera and projector models and calibration algorithms as well as a novel system design based on a combined phase shifting and stereovision method are introduced.

The first part of this dissertation introduces systems based on digital fringe projection and phase shifting techniques. In this research, a color fringe pattern is generated by software and projected onto the object being measured by a digital-light-processing (DLP) projector working in the black and white (B/W) mode. The fringe images are captured by a high speed CCD camera, which is synchronized with the

projector by software. The 3D model is reconstructed by using every three consecutive fringe images.

The previously developed linear calibration method does not take lens distortion into consideration and as a result, has very limited measurement accuracy. In this research, the effect of lens distortion on both the camera and projector is modeled based on careful calibration. Radial and tangential distortion parameters of different orders are analyzed and the right combination of parameters is chosen to provide an optimal performance. Experimental results show that the measurement accuracy has been improved by more than 75 percent (the RMS from 1.4 mm to 0.35 mm) after the implementation of the proposed nonlinear calibration method.

The proposed nonlinear calibration method is implemented in the real-time system to achieve higher accuracy. To enhance the performance of the system, a new real-time system is designed and experimented, which achieves a maximum speed of 60 Hz. A quality map guided phase unwrapping algorithm is developed as well to address the phase ambiguity problem of the previous phase unwrapping algorithm. As a result, phase unwrapping errors caused by discontinuous features are eliminated in most cases, thus significantly enhance the reliability of the system.

In the second part of this dissertation, a novel design, which combines the phase shifting and stereovision techniques, is proposed to eliminate errors caused by inaccurate phase measurement, for example, periodic errors due to the nonlinearity of the projector's gamma curve. This method uses two cameras, which are set up for stereovision and one projector, which is used to project phase-shifted fringe patterns onto the object twice with the fringe patterns rotated by 90 degrees in the second time. Fringe images are taken by

the two cameras simultaneously, and errors due to inaccurate phase measurement are significantly reduced because the two cameras produce phase maps with the same phase errors. One side effect of this method is that the projector calibration is not necessary, which simplifies the calibration of the entire system.

The use of a visibility-modulated fringe pattern is proposed as well to reduce the number of images required by this combined method. This new fringe pattern is sinusoidal in the horizontal direction as in a conventional fringe pattern, but is visibility-modulated in the vertical direction. With this new pattern, we can obtain the phase information in one direction and fringe visibility information in the other direction simultaneously. Since no pattern changing is necessary during the image acquisition process, the image acquisition time can be reduced to less than half of the time previously required, thus making the measurement of dynamically changing objects possible.

A color system is designed to further improve the speed of this system. Color cameras and color projector are introduced in this system. By utilizing these color devices, one color fringe image is sufficient to reconstruct a 3D model instead of three black and white fringe images. The three phase shifting fringe patterns are encoded into the R, G and B channels of the color pattern which is projected onto the object. And the color fringe images taken by color cameras can be separated into three black and white images. By using this technique, we can further improve the speed of the structure light system, and the system will be more resistant to fast moving objects.

Finally, a portable 3D measurement system based on the combined phase shifting and stereovision method is proposed, which can be used to measure large objects. During the whole measurement procedure, the projector is used to project a visibility-modulated

fringe pattern on the object and is relatively fixed to the object. The cameras are moved to as many positions as needed to capture local views. These local views can then be transformed into the same global coordinate system to form the whole 3D model of the big object which can not be measured by one take.

Table of Contents

LIST OF FIGURES	IX
LIST OF TABLES.....	XIII
ACKNOWLEDGMENT	XIV
CHAPTER 1 INTRODUCTION.....	1
1.1 APPLICATIONS AND MOTIVATIONS	1
<i>1.1.1 Medical system</i>	<i>1</i>
<i>1.1.2 Computer graphics and entertainment</i>	<i>2</i>
<i>1.1.3 Recognition.....</i>	<i>2</i>
<i>1.1.4 Robotic vision</i>	<i>3</i>
1.2 RELATED WORKS	3
<i>1.2.1 Optical 3D measurement techniques</i>	<i>4</i>
1.2.1.1 Stereovision.....	4
1.2.1.2 Time-of-flight.....	4
1.2.1.3 Photogrammetry	5
1.2.1.4 Laser scanner.....	5
1.2.1.5 Moiré	6
1.2.1.6 Other techniques.....	6
<i>1.2.2 Structured light techniques.....</i>	<i>7</i>
<i>1.2.3 Real-time system.....</i>	<i>9</i>
<i>1.2.4 Camera model and calibration.....</i>	<i>9</i>
<i>1.2.5 Approaches to measure 360 degree shape of objects.....</i>	<i>10</i>
1.3 OBJECTIVES	11
1.4 DISSERTATION STRUCTURES.....	12
CHAPTER 2 3D SHAPE MEASUREMENT BASED ON THE PHASE SHIFTING TECHNIQUE	14
2.1 PHASE SHIFTING TECHNIQUE	14
<i>2.1.1 Fundamental concept</i>	<i>14</i>
<i>2.1.2 Three-step algorithm</i>	<i>16</i>
<i>2.1.3 Phase unwrapping</i>	<i>18</i>
2.2 SYSTEM SETUP	20
2.3 LINEAR CALIBRATION AND COORDINATE RECONSTRUCTION	25
2.4 SUMMARY	32
CHAPTER 3 NONLINEAR CALIBRATION.....	33
3.1 FUNDAMENTAL CONCEPTS OF LENS DISTORTION	33
3.2 NONLINEAR CALIBRATION OF CAMERA.....	38
3.3 NONLINEAR CALIBRATION OF PROJECTOR	45
3.4 SUMMARY	54
CHAPTER 4 REAL-TIME SYSTEM BASED ON THE NONLINEAR CALIBRATION METHOD	55

4.1	REAL-TIME SYSTEM WITH AN ENCODED COLOR PATTERN	55
4.2	60 Hz SYSTEM	64
4.3	SUMMARY	65
CHAPTER 5 QUALITY MAP GUIDED PHASE UNWRAPPING ALGORITHM		67
5.1	PHASE AMBIGUITY	67
5.2	QUALITY MAP GUIDED PHASE UNWRAPPING	68
5.3	SUMMARY	72
CHAPTER 6 THE COMBINED PHASE SHIFTING AND STEREOVISION METHOD		73
6.1	PHASE ERRORS OF THE PHASE SHIFTING METHOD	74
6.2	COMBINED PHASE SHIFTING AND STEREOVISION METHOD	75
6.2.1	<i>Principles and system setup</i>	76
6.2.2	<i>Pixel matching and 3D model reconstruction</i>	78
6.2.3	<i>Experimental results</i>	80
6.3	USE OF A VISIBILITY-MODULATED FRINGE PATTERN	84
6.3.1	<i>Principles</i>	84
6.3.2	<i>Experimental Results</i>	88
6.4	SUMMARY	91
CHAPTER 7 COLOR SYSTEM BASED ON THE COMBINED PHASE SHIFTING AND STEREOVISION TECHNIQUE		92
7.1	MOTION ERROR OF B/W SYSTEM	92
7.2	COLOR BASED APPROACH	94
7.2.1	<i>Color-encoded fringe pattern</i>	94
7.2.2	<i>Color imbalance and color coupling</i>	94
7.2.3	<i>Use of a color visibility-modulated fringe pattern</i>	97
7.3	EXPERIMENTS	97
7.3.1	<i>System setup</i>	97
7.3.2	<i>Compensation methods</i>	98
7.3.3	<i>Experimental results</i>	99
7.3.4	<i>Discussion</i>	101
7.4	SUMMARY	103
CHAPTER 8 PORTABLE 3D MEASUREMENT SYSTEM.....		104
8.1	PRINCIPLES	104
8.1.1	<i>System setup and measurement strategy</i>	104
8.1.2	<i>Data Registration</i>	106
8.2	EXPERIMENTAL RESULTS	108
8.3	SUMMARY	111
CHAPTER 9 CONCLUSIONS AND FUTURE WORKS		112
9.1	CONCLUSIONS	112
9.2	FUTURE WORKS	115
BIBLIOGRAPHY		117

List of Figures

Figure 2.1: The variation of intensity with the reference phase.....	16
Figure 2.2: The conversion of the phase to modulo 2π	19
Figure 2.3: Phase unwrapping process.....	19
Figure 2.4: Schematic diagram of the system layout.....	20
Figure 2.5: Inside look of the system.....	21
Figure 2.6: Encoded color fringe pattern.....	22
Figure 2.7: System timing chart.....	23
Figure 2.8: Example of 3D reconstruction. (a)-(c) Three fringe images. (d) Wrapped phase map. (e) Reconstructed 3D model. (f) Reconstructed 3D model with texture.....	24
Figure 2.9: Camera coordinate system and world coordinate system.....	25
Figure 2.10: Checkerboard used for calibration. (a) Red/Blue checkerboard. (b) Checkerboard image.....	27
Figure 2.11: World coordinate system in (a) A CCD checkerboard image (b) A DMD checkerboard image.....	27
Figure 2.12: Eight images used to determine CCD and DMD pixel correspondence.....	29
Figure 2.13: Relationship between the three coordinate systems.....	30
Figure 3.1: Example of radial and tangential lens distortion. (a) Radial distortion. (b) Tangential distortion.....	34
Figure 3.2: Checkerboard image before and after lens distortion correction. (a) Before nonlinear correction. (b) After nonlinear correction.....	35
Figure 3.3: Error maps of measured flat board. (a) 3D model of a flat board at a near position. (b) Error map when the flat board is at the near-position. (c) Cross section of the near-position error map at the 450th row. (d) Error map when the flat board is placed at a further position.....	39
Figure 3.4: Error maps after the camera nonlinear calibration algorithm is applied. (a)-(b) The error at a near position. (c)-(d) The error map at a further position.....	43
Figure 3.5: Error maps of the flat board measured in different orientations.....	44
Figure 3.6: Error maps of a flat board measured with different calibration methods: (a) Linear calibration method. (b) Nonlinear calibration on camera only. (c) Nonlinear calibration on both camera and projector with the eight-image	

method. (d) Nonlinear calibration on both camera and projector with the iterative method. (e) Nonlinear calibration on both camera and projector with the cubic equation method.	53
Figure 3.7: 3D reconstruction results obtained by using the nonlinear cubic equation method.....	54
Figure 4.1: Flow chart of the multi-thread real-time 3D shape measurement system.	56
Figure 4.2: (a) Ideal fringe pattern. (b) Modified fringe pattern with higher intensity. (c) Fringe patterns with a short centerline marker. (c) Fringe patterns with a wide centerline marker.....	58
Figure 4.3: Markers in the fringe images.	58
Figure 4.4: Interactive marker-searching window. (a) Default window. (b) Adjusted window.....	60
Figure 4.5: Data modulation of the image with a crosshair marker. (a) 2D image. (b) Data modulation.....	60
Figure 4.6: Automatic searching for the crosshair marker by using epipolar line.	62
Figure 4.7: 3D data texture map. (a) Old texture map. (b) New texture map.....	62
Figure 4.8: Selected 3D models of a real-time measurement sequence of human face expression.....	63
Figure 4.9: Timing chart of the 60 Hz System.....	64
Figure 4.10: Front and back views of the high speed camera.....	66
Figure 4.11: Human face models scanned by the 60 Hz system.....	66
Figure 5.1: Phase ambiguity example. (a) 2D fringe image with phase discontinuity on the lower edge of the step which will cause phase ambiguity. (3) 3D model with phase jump cause by phase ambiguity.....	68
Figure 5.2: Quality map of the board with a step.....	69
Figure 5.3: Quality map guided flood-fill phase unwrapping algorithm.	70
Figure 5.4: 3D model of the step on a board reconstructed by the quality map guided flood-fill algorithm.....	71
Figure 5.5: 3D model of a human face. (a) 2D image. (b) 3D model reconstructed by the old algorithm. (c) The quality map. (d) 3D model reconstructed by the quality map guided flood-fill algorithm.....	71
Figure 6.1: Examples of phase errors. (a) Error caused by nonlinear projector gamma. (b) Error caused by color contrast.	75
Figure 6.2: Schematic diagram of the system layout.	76
Figure 6.3: Absolute phase maps of Zeus statue. (a) Horizontal increasing absolute phase map. (b) Vertical increasing absolute phase map.	77
Figure 6.4: Epipolar constraint used in this method.	79

Figure 6.5: The setup of the combined phase shifting and stereovision system. (a) Cameras set up for stereovision. (b) Projector used to project pattern is separated from the cameras.....	80
Figure 6.6: 3D models of (a) Zeus statue and (b) card box reconstructed by the combined phase shifting and stereovision method.	81
Figure 6.7: Error cross sections of a flat board 3D model. (a) Measured by phase shifting method. (b) Measured by the combined phase shifting and stereovision method.....	82
Figure 6.8: Results comparison of modified patterns. (a) Results measured by traditional phase shifting method. (b) Results measured by the combined phase shifting and stereovision method.....	83
Figure 6.9: (a) Visibility-modulated fringe pattern. (b) Sinusoidal waveforms at two different vertical positions	86
Figure 6.10: Stereo matching procedure. (a) Using the phase maps to find the same phase curve (b) Matching the visibility values to locate the right pixel.	87
Figure 6.11: Results measured with visibility-modulated fringe pattern.....	89
Figure 6.12: Cross sections of a flat board 3D model measured with the visibility-modulated fringe pattern.	89
Figure 6.13: 8 selected 3D models of dynamically changing facial sequence captured by using the combined phase shifting and stereovision method with the visibility-modulated fringe pattern.....	90
Figure 7.1: Schematic diagram of the error caused by object motion.....	93
Figure 7.2: Color imbalance of the three color channels.	96
Figure 7.3: Color coupling appearance in a green fringe image.	96
Figure 7.4: Measurement results of (a) the color phase shifting method, and (b) the proposed combined phase shifting and stereovision color system.	99
Figure 7.5: Measurement results of objects in motion by combined phase shifting and stereovision systems. (a) Results obtained by B/W system. (b) Results obtained by color system.....	101
Figure 7.6: Red channels of two color images taken by different color cameras. (a) Image taken by single-CCD camera. (b) Image taken by 3-CCD camera.....	102
Figure 8.1: Schematic diagram of the portable system.	105
Figure 8.2: Finding corresponding pixel pairs for two local views.	107
Figure 8.3: Pattern with multiple reference lines.	107
Figure 8.4: Experimental results of a plaster statue. (a) The first local view. (b) The second local view. (c) Local views before coordinate translation. (d) Merged local views after coordinate translation.	108
Figure 8.5: Measurement results of a metal part.....	109

Figure 8.6: Measurement results of a plaster seahorse attached on a flat board. (a) Point clouds of 9 local views. (b) The whole 3D model. (c) The central local view. (d) The central local view in the whole model..... 110

Figure 8.7: Experimental results of a fender. (a) The whole 3D model with colored local views. (b) The whole 3D model shown in one color. 111

List of Tables

Table 2.1: 2π phase correction.	18
Table 3.1: Camera intrinsic parameters with different distortion models.....	37
Table 3.2: Camera lens distortion coefficients.....	37
Table 3.3: Camera extrinsic parameters.....	41
Table 3.4: RMS errors of the flat board measured in different orientations. RMS (L): Linear calibration; RMS (CNL): Camera nonlinear calibration.	44
Table 3.5: Projector intrinsic parameters with different distortion models.....	45
Table 3.6: Projector lens distortion coefficients.....	46
Table 3.7: Projector extrinsic parameters.....	46
Table 3.8: RMS errors of the measured flat board in different orientations.	52

Acknowledgment

First I would like to express my sincere gratitude to Professor Peisen Huang, my academic advisor, for his continuous guidance and support during the past a few years. Without his patient instructions and brilliant ideas this dissertation can not be finished so smoothly.

Many thanks to the committee members, Professor Jeffery Ge, Professor Yu Zhou and Professor Hong Qin, for their precious time spent on this dissertation and their valuable suggestions.

I give my special thanks to Song Zhang, who gave me a very helpful guidance at the beginning of my research even after his graduation. And I would like to give my thanks to all my colleagues and friends in the department of Mechanical Engineering and in the Stony Brook University.

Finally, I want to thank my parents and all my families for their constant support and understanding.

Chapter 1 Introduction

In recent years, 3D shape measurement techniques have found wide applications in manufacturing, on-line inspection, biomedical engineering, entertainment, quality control, reverse engineering, etc [1]. Real-time 3D shape measurement, as a new technology breakthrough in this area, has even more potential applications in many areas due to its capability of measuring moving objects [2]. This dissertation presents a major effort in improving the performance of 3D shape measurement systems mainly based on digital fringe projection, phase shifting and stereovision techniques. A novel nonlinear calibration method is developed and utilized in the real-time system to achieve high-accuracy, real-time 3D shape measurement. Systems based on a combined phase shifting and stereovision technique is designed as well to eliminate systematic errors. Finally, this combined technique is used in a portable system which can be used for measurement of large size objects.

1.1 Applications and Motivations

1.1.1 Medical system

3D measurement systems can help in automatic medical systems, for example, laser debridement system. Traditionally, doctors need to operate the system and do all the tedious works themselves to scan the whole wounded areas line by line with a laser head. This repeating work can be highly automated by integrating a real-time 3D sensor to

track the motion of human bodies and locate the wounded areas with 2D image processing and 3D information. The laser head can be calibrated with the 3D sensor, and can communicate with the 3D sensor to obtain the current coordinates for scanning and scan the arrears automatically, such that releases the doctors from the tedious work and achieve a higher reliability.

1.1.2 Computer graphics and entertainment

Computer animation which is widely used in entertainment industry is increasingly generated by means of 3D computer graphics. 3D models of real world objects and human beings are created when making films and video games. 3D measurement system can help to generate 3D models in an easier way, provide higher resolution and make the models more realistic. Motion data sequences such as human being's body language, postures and facial expressions can also be recorded by real-time 3D measurement systems. These raw data can then be transmitted onto the digital 3D model to imitate human beings' behaviors.

1.1.3 Recognition

Current facial recognition and speech recognition techniques are mostly based on 2D image processing. However, a main problem of these techniques is that 2D images provide different features when the images are taken from different perspectives. 3D techniques are more stable in this aspect that, regardless of the perspectives, the final 3D models consist in features. Thus, more accurate and more stable recognition results are

accomplishable by using 3D sensors which provide both 2D images and the corresponding 3D geometries.

1.1.4 Robotic vision

3D sensors can also be built in assistive robotic systems such as rescue robots to obtain the surrounding features and structures [3]. With the information provided by 3D sensors, robot navigation can be realized in cluttered dusty environment like urban search and rescue tasks. Victim identification can also be achieved by human gesture recognition and human emotional state classification with 3D shape information.

1.2 Related Works

Traditional Coordinate Measuring Machines (CMMs) are point-by-point measuring systems. CMMs can not meet all the demands of 3D shape measurement because they are usually slow and can cause potential damage to object surfaces. With the latest development of technologies in digital imaging, digital video projection, and digital image processing, vision-based optical metrology techniques are being utilized more and more extensively. Many methods have been developed based on the stereovision, photogrammetry, time-in-flight, interferometry, and various types of coded structured light techniques, etc. The stereovision method and structured light method based on a phase shifting technique are mainly used for this dissertation research.

In this section, we will give an overview of several well-known optical metrology techniques as mentioned above and will introduce structured light techniques with more details. We will also include some related works involving real-time system, calculation

of absolute phase value, camera models and calibration, and approaches for full body measurement.

1.2.1 Optical 3D measurement techniques

1.2.1.1 Stereovision

Stereovision is one of the most studied techniques [4], in which two cameras take pictures of the same scene, but separated by a distance - simulating the human eyes. It is widely used in mobile robotics for obstacles detection and navigation. By comparing the two images, the best match parts are used to calculate the distance. However, finding the homologous points is a challenging problem and computationally expensive. Several techniques have been developed to provide more efficient and faster stereo matching, such as multi-resolution techniques and correlation based techniques [5]. The stereo matching problem is also brought into time domain by a technique called space-time stereo to reduce matching ambiguity [10].

1.2.1.2 Time-of-flight

The time-of-flight method measures the time that it takes for a particle or object to reach a measurement sensor while traveling over a known distance [11]. Time-of-flight based systems have the advantages of real-time, robust, and capable of operating over very long distances. However, this kind of system usually has a limited resolution of millimeter. High-resolution techniques were also reported can achieve submillimeter resolution [12]. In addition, typical resolution of time-of-flight cameras is usually no more than 320×240 , which is much lower than modern cameras.

1.2.1.3 Photogrammetry

Photogrammetry technique, which typically employs stereo technique for 3D measurement, can provide a very high accuracy as one part in 100,000 or even 1,000,000 [16]. The reconstruction is usually implemented by a least square procedure based on the principle of bundle adjustment [17], [18]. This principle can be used to realize system self-calibration [19], in which case, the 3D coordinates and the system parameters are determined at the same time. However, in a typical photogrammetry system, markers are required to be placed at various locations of the object surface. The concept of virtual landmarks was proposed by G. Notni, et al [22], to solve this problem, which eliminated the need of physical markers by using an extra connecting camera relatively fixed to the object. The phase values of the pixels in the connecting camera were used as the virtual landmarks. Some other methods such as defocusing, scaling and shading are also used for photogrammetry technique.

1.2.1.4 Laser scanner

Laser scanners are active scanners which employ either time-of-flight technique or triangulation relationship in optics. The triangulation laser scanner emits a laser on the object and utilizes a camera to track the laser dot location. Depending on the distance between the laser emitter and the object, the laser dot appears at different places in the camera's field of view. The so called triangulation relationship is referring to the triangle formed by the laser dot, the camera and the laser emitter. In order to speed up the acquisition process, a laser stripe, instead of a single laser dot, is often used and swept across the object. Triangulation laser scanners usually have a very high measurement

frequency of 40 kHz or higher [23], [24]. The typical measurement range is ± 5 to ± 250 mm, and the accuracy is about 1 part in 10,000.

1.2.1.5 Moiré

Moiré technique has been widely applied as a noncontact method for 3D shape contouring [25]. Moiré fringes are formed by the superposition of two gratings. According to the principle used, Moiré technique can be classified into projection moiré and shadow moiré [33], [34]. The key to the former method is two separated gratings, one is a master grating and the other is a reference grating. In the latter method, only one grating is used. However it is usually difficult to apply it for the measurement of large objects.

Snap shot or multiple image moiré systems have been developed for overcoming environmental perturbations, increasing image acquisition speed, and employing phase shift methods for the fringe pattern analyzing. Multiple moiré fringe patterns with different phase shifts are acquired simultaneously using multiple cameras or image-splitting methods [35]. The typical measurement range of the phase shifting moiré method is from 1 mm to 0.5 m with the resolution at 1/10 to 1/100 of a fringe [38].

1.2.1.6 Other techniques

Other widely used and well studied optical 3D measurement techniques include interferometry [39], Laser Speckle Pattern Sectioning [42], shape from shading [45], shape from focus/ defocus [46], [47] and structured light techniques, which are employed in this research and introduced in details in the following section.

1.2.2 Structured light techniques

Structured light technique is an active triangulation technique for measuring the 3D shape of an object by using projected light patterns and a camera system. It is similar to the stereovision technique, except that one of the cameras is replaced by an image projection device [48]. Although many other variants of structured light projection are possible, patterns of parallel stripes are widely used. By projecting a coded fringe pattern onto a 3D shaped surface, the depth information is encoded in the deformed fringe pattern. The shape of the surface can be directly decoded from the deformed fringe pattern images taken by an image acquisition device [1].

The most well-known structured light technique is phase shifting technique, for example, three-step phase shifting technique [49] used in this research. For real-time 3D shape measurement, a three-step algorithm is the optimal choice because it requires the minimum number of fringe images. In most cases, three fringe patterns with 120 degrees phase shift to each other are projected onto the object by a projector. At the meanwhile, a camera which is calibrated with the projector is used to grab fringe images of the object. Then a phase map, which is used to decode the 3D shape, can be calculated from every three fringe images by phase wrapping and unwrapping algorithms. The details of three-step phase shifting technique will be exposed in Chapter 2.

Binary coding is another well-known technique which extracts depth information by projecting multiple binary coded structured light patterns [52], [53]. In this technique, only two illumination levels, 0 and 1, are commonly available. Multiple stripe patterns are projected, and for every pixel its corresponding value in each image is either 0 or 1. A codeword composed of 0s and 1s is obtained for every pixel when the projection

sequence is completed. 3D shape information can be retrieved based on decoding the codeword. This technique is robust to noise. However, the resolution cannot be very high. In order to increase resolution more patterns could be projected which, in another aspect, increases the acquisition time. In general this method is not suitable for high-resolution real-time measurement.

Techniques of multi-level grey coding are developed, in which multiple intensity levels are used to reduce the number of required fringe patterns. References can be found in [54]. The N-ary methods significantly reduce number of fringe images; however, they usually require additional threshold references to obtain high resolution. Binary code technique is actually a special case of N-ary code when N equals 2.

Methods using color-encoded fringe patterns have been proposed for high speed measurement by reducing the required number of fringe images, since a single color image includes more information than a single grey level image. Harding proposed a color encoded moiré technique that can reconstruct the 3D shape by a single snapshot [58]. Zhang and Curless developed a color structured light technique, which projects a pattern of stripes with alternating colors and can recover the 3D shape from one or more images [59]. Jeong and Kim presented a color grating projection moiré method, which can perform 3D contouring with only a single operation [60]. Huang et al. proposed a color phase shifting method, in which three phase-shifted fringe patterns are encoded in the Red, green, and blue channels to form a color fringe pattern [61]. Since only one single color fringe image is sufficient for 3D reconstruction, this technique significantly increases the measurement speed. However, due to phase errors caused by the use of color, the achieved measurement accuracy was limited. Pan et al. continued the work by

introducing both hardware and software based methods to reduce phase errors caused by the use of color [62]. Significant improvement was achieved, but the results were still not ideal.

There are various other structured light techniques have been developed and reported, such as the use of Fourier transform [63], [64], intensity ratio [65], [66], random patterns [67], trapezoidal phase shifting patterns [68], etc.

1.2.3 Real-time system

Real-time 3D shape measurement technique is attracting increasingly more attention in the research community lately due to its ability of capturing the 3D shapes of moving objects. So far a number of approaches have been proposed, which can be classified into two basic categories: single-pattern-based techniques and multiple-pattern-based techniques. Single-pattern-based techniques, as the name suggests, use only one pattern for 3D shape acquisition. This kind of methods usually use color pattern [58][69], as well as Fourier transform [70]. As for multiple-pattern-based techniques, multiple patterns are switched quickly so that images of these patterns can be taken in a relatively short time period [2][71], [72]. Obviously, single-pattern techniques have the advantage of higher achievable measuring speed. However, multiple-pattern techniques usually provide better resolution.

1.2.4 Camera model and calibration

A proper calibration of elements used in any structured light system is the key to accurate 3D reconstruction [73]. Methods based on different approaches have been

developed, such as absolute phase [74], bundle adjustment [19][75][76] and neural networks [77], etc. For any structured light system that uses cameras and projectors, lens distortion, especially the radial distortion, is a common issue. It has to be dealt with if more accurate measurement is to be made. Elaborate lens distortion models with high order terms have been investigated in many cases [78]. However, a lens distortion model with only two radial terms is usually sufficient. In most cases, the lens distortion is actually dominated by the first radial component [81], [82]. A novel calibration method is developed by Zhang and Huang. In this method, the projector is treated as a camera, and the calibration procedure is much simplified [83]. A nonlinear calibration based on this technique is further developed by Huang and Han [84].

1.2.5 Approaches to measure 360 degree shape of objects

To measure objects with large sizes or conduct 360 degree measurement, either a single system taking measurements sequentially at different locations or multiple systems taking measurements simultaneously from different positions are necessary [1]. Once these measurement data or local views are obtained, a registration method is used to transform these local views from their own coordinate systems to a global coordinate system and then stitch them together to form a complete 3D model [85], [86].

Several approaches could be used to determine the transformations between the local views. One is to have the system fixed on a high accuracy mechanical positioning system, which is quite straightforward [87], [88]. However, such a system usually requires equipment with a high cost in order to achieve high accuracy. Another approach is photogrammetry, which can provide a high accuracy without the need for expensive

equipment [89]. However, in a typical photogrammetry system, markers are required to be placed at various locations of the object surface. During the measurement, every local view needs to include some of these markers to establish its relationships with its neighboring views. The use of physical markers makes the procedure time-consuming and complex. To solve this problem, G. Notni proposed the concept of virtual landmarks [22], which eliminated the need of physical markers by using an extra connecting camera. Multiple cameras and projectors are used in his system and the bundle adjustment technique is used to obtain the system parameters and objects coordinates simultaneously.

1.3 Objectives

This dissertation research is focused on improving the performance of the 3D shape measurement systems based on digital fringe projection, phase shifting and stereovision techniques. Some issues need to be addressed in order to make these methods even more accepted. The objectives of this research are listed as following:

- 1) Employ a nonlinear calibration method for cameras and projectors used in the phase shifting system to reduce the error caused by lens distortion.
- 2) Implement the nonlinear calibration method, absolute phase calculation, quality map guided phase unwrapping algorithm and new-generation high speed cameras in the real-time system to simplify the system setup and build up a new real-time measurement system with higher speed and better accuracy.
- 3) Develop new systems based on a combined phase shifting and stereovision method to eliminate the errors caused by the projector's nonlinear gamma curve. Realize the

- measurement of moving objects by applying a novel visibility-modulated fringe pattern.
- 4) Develop a system composed of color devices and use color visibility-modulated fringe pattern to achieve further improve the measurement speed.
 - 5) Develop a system for large objects measurement based on the combined phase shifting and stereovision method.

1.4 Dissertation Structures

Chapter 2 introduces the basic theory of three-step phase shifting technique and describes the setup of a typical 3D shape measurement system based on this technique. This chapter also introduces the linear calibration method previously developed, which is the basis of the nonlinear calibration method.

In Chapter 3, some fundamental concepts of lens distortion are first introduced. Then a nonlinear camera calibration method is proposed, followed by a nonlinear projector calibration method. The results on the measurement accuracy achieved by both the linear and nonlinear calibration methods are compared.

Chapter 4 describes the implementation of the nonlinear calibration method in real-time measurement system. This chapter describes a new method for obtaining the absolute phase information. As a result, the proposed nonlinear calibration method can be utilized in the real-time measurement system to significantly improve the accuracy of the system. This chapter also introduces the next-generation real-time system, which has a 3D shape acquisition speed of 60 Hz.

Chapter 5 introduces a new quality map guided phase unwrapping algorithm, which is designed to eliminate phase unwrapping ambiguities. The chosen quality map

and the new flood-fill algorithm is evaluated and some improved phase unwrapping results are presented.

Chapter 6 introduces a new method based on a combined phase shifting and stereovision technique to eliminate the phase errors caused by the projector's nonlinear gamma curve. Two cameras are set up for stereovision, and the projector is used to project fringe patterns for stereo matching. Since the two cameras produce phase maps with the same phase error, systematic errors are significantly eliminated. The use of a new designed visibility-modulated fringe pattern is also proposed to reduce the required number of fringe images, so that the system can be used to measure moving objects.

In Chapter 7, a color system based on the combined phase shifting and stereovision technique is proposed to further improve the speed of this system. Color cameras and color projectors are utilized in this system. The special issues, such as color imbalance and color coupling, are dealt with by proper methods. Measurement results of both static and dynamic objects are compared with the results taken by the black and white system and the traditional phase shifting system.

Chapter 8 proposes a portable 3D measurement system based on the combined phase shifting and stereovision method which can measure large objects. This system is very simple in structure, and the only mobile part is the two cameras connected by a light metal frame which is easy to handle. Efficient registration method is designed for quick and accurate 3D model generating.

Chapter 9 presents the conclusions of this research and discusses the future works.

Chapter 2 3D Shape Measurement Based on the Phase Shifting Technique

2.1 Phase Shifting Technique

The phase shifting technique used in this research has its root in phase shifting interferometry (PSI), which is a fringe analysis method widely used in optical metrology. PSI simply records a series of interferograms, in which the wavefront phase is encoded, while the interferometer reference phase is changed and recovers the phase just by a point-by-point calculation. The need to locate the fringe centers is thus discarded, simplifying fringe analysis and improving its accuracy. PSI has been widely known by many names including phase measuring interferometry, fringe scanning interferometry and real-time interferometry. But all of them describe the same basic technique.

2.1.1 Fundamental concept

The fundamental concept behind PSI is the introduction of a time-varying phase shift between the reference wavefront and the test wavefront in the interferometer. As a result, a time-varying signal, in which the relative phase between the two wavefronts is encoded, is produced at each measurement point in the interferogram [51] [90].

The reference and test wavefronts in the interferometer can generally be represented by the following expressions:

$$w_r(x, y, t) = a_r(x, y)e^{i[\phi_r(x, y) - \delta(t)]} \quad 2.1$$

and

$$w_t(x, y) = a_t(x, y)e^{i\phi_t(x, y)} \quad 2.2$$

where $a_r(x, y)$ and $a_t(x, y)$ are the wavefront amplitudes, $\phi_r(x, y)$ and $\phi_t(x, y)$ are the wavefront phases, and $\delta(t)$ is a time-varying phase shift introduced into the reference beam. The resulting intensity pattern is

$$I(x, y, t) = |w_r(x, y, t) + w_t(x, y)|^2 \quad 2.3$$

or

$$I(x, y, t) = I'(x, y) + I''(x, y)\cos[\phi_t(x, y) - \phi_r(x, y) + \delta(t)] \quad 2.4$$

where $I'(x, y) = a_r^2(x, y) + a_t^2(x, y)$ is the average intensity and $I''(x, y) = 2a_r(x, y)a_t(x, y)$ is the fringe or intensity modulation. If we define $\phi(x, y)$ to be the wavefront phase difference $\phi_t(x, y) - \phi_r(x, y)$, we obtain

$$I(x, y, t) = I'(x, y) + I''(x, y)\cos[\phi(x, y) + \delta(t)] \quad 2.5$$

which is the fundamental equation for PSI. This result can be illustrated by plotting the intensity as a function of $\delta(t)$, as shown in Figure 2.1. The constant term $I'(x, y)$ is the intensity bias, $I''(x, y)$ is half the peak-to-valley intensity modulation, and the unknown phase $\phi(x, y)$ is related to the temporal phase shift.

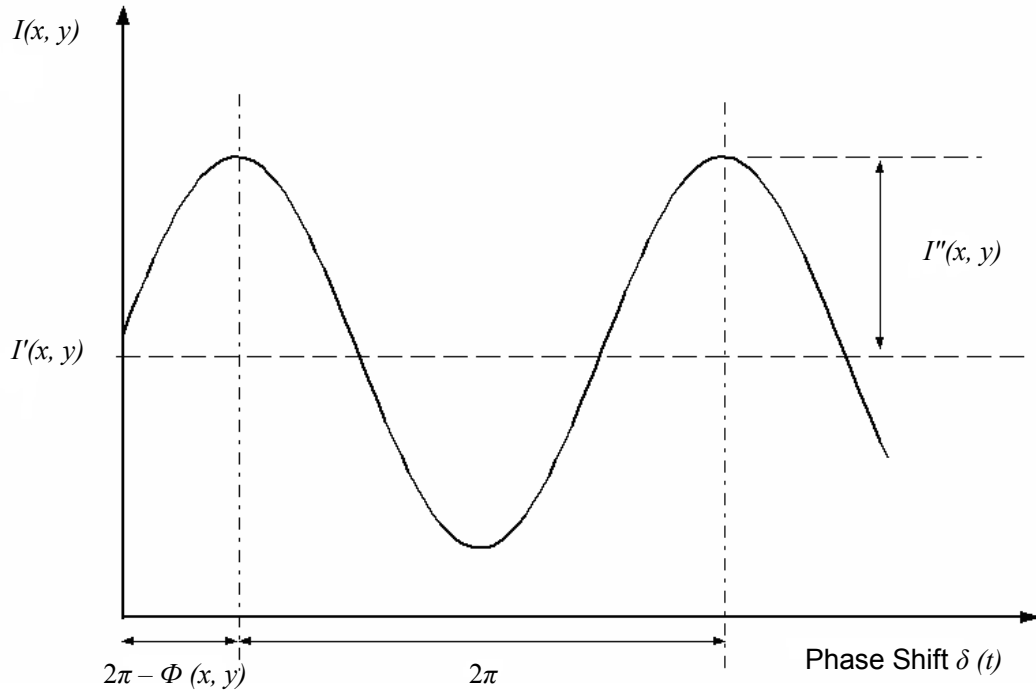


Figure 2.1: The variation of intensity with the reference phase.

2.1.2 Three-step algorithm

All of the commonly used algorithms for PSI share the same characteristic: a series of interferograms are recorded as the reference phase is varied. The wavefront phase is then calculated at each point as the arctangent of a function of the interferogram intensities measured at that point. The final wavefront map is obtained by unwrapping the phases to remove the 2π phase discontinuities.

Since there are three unknowns ($I(x, y), I''(x, y), \phi(x, y)$) in Eq. (2.5), the minimum number of intensity values that is required to reconstruct the wavefront at each measurement point is three. For real-time 3D shape measurement, a three-step algorithm

is the optimal choice because it requires the minimum number of fringe images.

Assuming equal phase steps of size α in Eq. (2.5), or $\delta_i = -\alpha, 0, \alpha$, where $i = 1, 2, 3$, we have

$$I_1(x, y) = I'(x, y) + I''(x, y) \cos[\phi(x, y) - \alpha] \quad 2.6$$

$$I_2(x, y) = I'(x, y) + I''(x, y) \cos[\phi(x, y)] \quad 2.7$$

and

$$I_3(x, y) = I'(x, y) + I''(x, y) \cos[\phi(x, y) + \alpha] \quad 2.8$$

Solving these equations, we can easily find the wavefront phase at each point as:

$$\phi(x, y) = \tan^{-1} \left\{ \left[\frac{1 - \cos(\alpha)}{\sin(\alpha)} \right] \frac{I_1 - I_3}{2I_2 - I_1 - I_3} \right\} \quad 2.9$$

and the average intensity $I'(x, y)$ and intensity modulation $I''(x, y)$ are

$$I'(x, y) = \frac{I_1 + I_3 - 2I_2 \cos(\alpha)}{2[1 - \cos(\alpha)]} \quad 2.10$$

and

$$I''(x, y) = \frac{\{[1 - \cos(\alpha)](I_1 - I_3)\}^2 + [\sin(\alpha)(2I_2 - I_1 - I_3)]^2\}^{1/2}}{2 \sin(\alpha)[1 - \cos(\alpha)]} \quad 2.11$$

respectively. The ratio of these two intensities defines the so called data modulation:

$$\gamma(x, y) = \frac{I''(x, y)}{I'(x, y)} \quad 2.12$$

The most commonly used phase steps for the three-step algorithm are $\pi/2$ and $2\pi/3$. In our case, $\alpha = 2\pi/3$ is used, which results in the following equations for the phase and intensity modulation:

$$\phi(x, y) = \tan^{-1} \left(\sqrt{3} \frac{I_1 - I_3}{2I_2 - I_1 - I_3} \right) \quad 2.13$$

and

$$\gamma(x, y) = \frac{\sqrt{3(I_1 - I_3)^2 + (2I_1 - I_2 - I_3)^2}}{I_1 + I_2 + I_3} \quad 2.14$$

2.1.3 Phase unwrapping

One more operation must be performed before the phase result is ready to be used for wavefront reconstruction. Since arctangent is defined only over the range of $-\pi/2$ to $\pi/2$, the discontinuities that occur in the phase calculation must be corrected. The signs of sine and cosine of the phase are known independently in addition to the tangent value. Table 2.1 shows how to convert arctangent values to phase values between 0 and 2π and Figure 2.2 illustrates this process.

After the above process, the phase map obtained still has 2π discontinuities, which need to be removed as well to finally reconstruct the wavefront. This second process is usually called phase unwrapping and the principle is shown in Figure 2.3.

Table 2.1: 2π phase correction.

Sine	Cosine	Corrected Phase $\Phi(x, y)$	Phase Range
0	+	0	0
+	+	$\Phi(x, y)$	0 to $\pi/2$
+	0	$\pi/2$	$\pi/2$
+	-	$\Phi(x, y) + \pi$	$\pi/2$ to π
0	-	π	π
-	-	$\Phi(x, y) + \pi$	π to $3\pi/2$
-	0	$3\pi/2$	$3\pi/2$
-	+	$\Phi(x, y) + 2\pi$	$3\pi/2$ to 2π

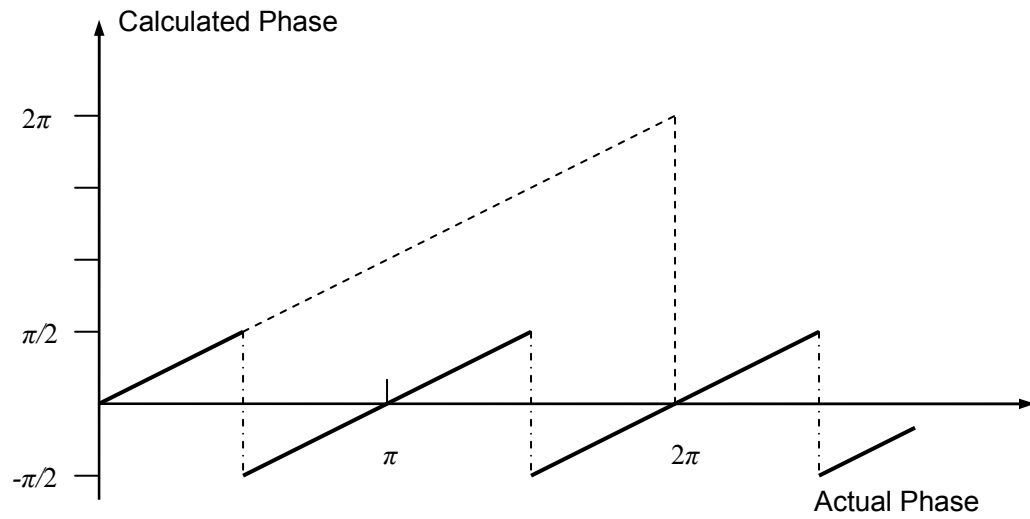


Figure 2.2: The conversion of the phase to modulo 2π .

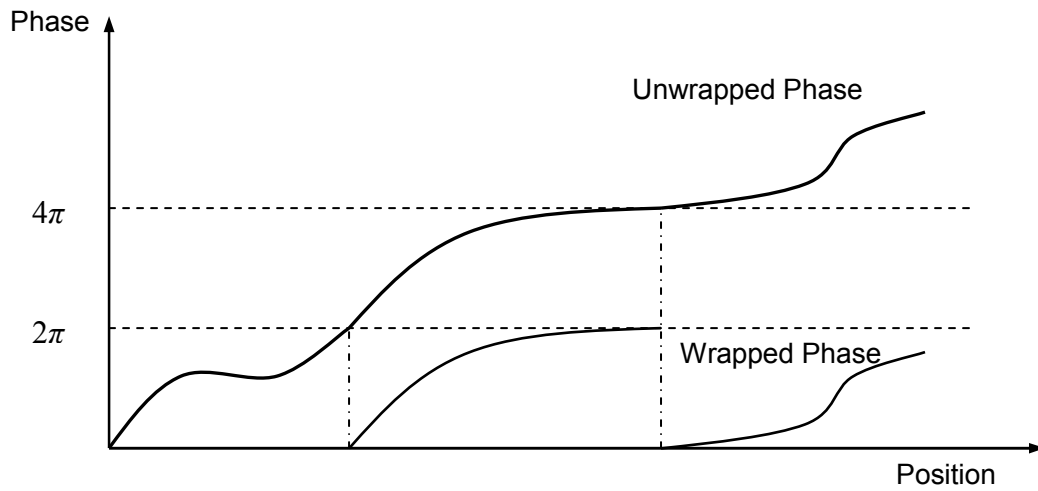


Figure 2.3: Phase unwrapping process.

2.2 System Setup

The 3D shape measurement system described in this chapter is based on the digital fringe projection and phase shifting technique. A digital projector (PLUS U5-632 with a resolution of 1024×768 and a brightness of 3000 lumens) is utilized to project fringe patterns generated by a personal computer onto the object being measured. A CCD camera (Dalsa CA-D6-0512 with a resolution of 532×500) is used to grab fringe images of the object, which are then processed by the computer for 3D shape reconstruction. Figure 2.4 shows a schematic diagram of the system layout. Both the projector and the camera communicate to the same computer, which has dual display outputs. One display output is used for the computer monitor, while the other used for creating the fringe pattern to be projected by the projector. Figure 2.5 is a photograph of the actual system.

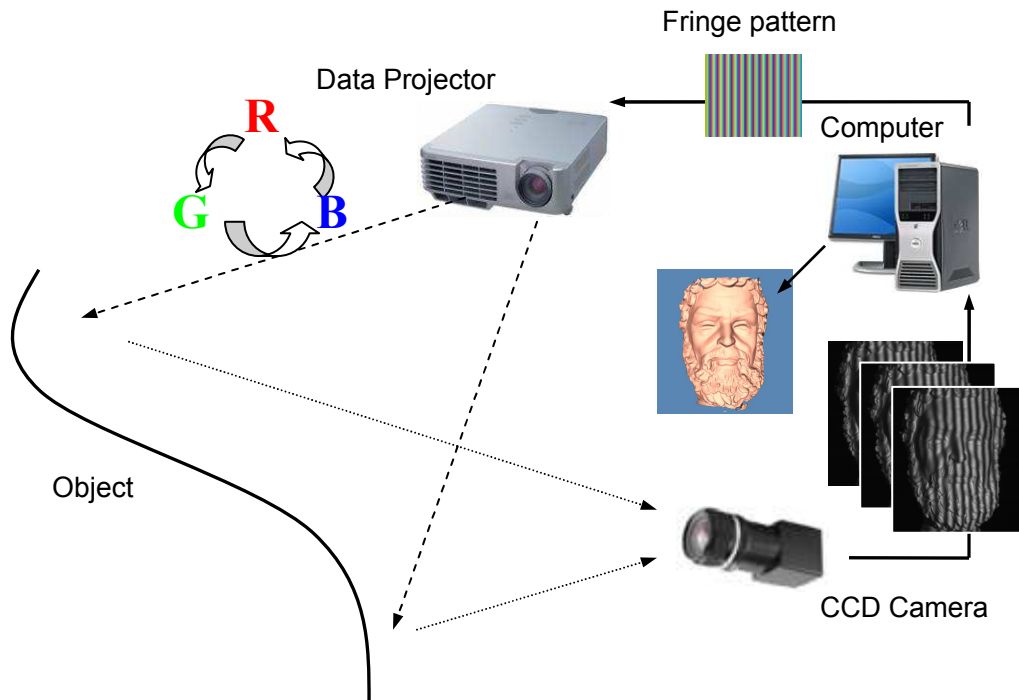


Figure 2.4: Schematic diagram of the system layout.

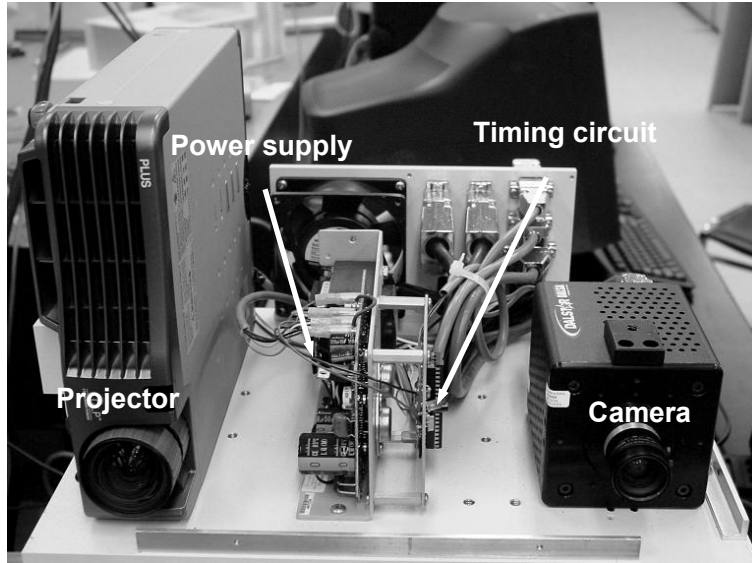


Figure 2.5: Inside look of the system.

Based on the projection mechanism of the projector, we encode the three phase-shifted fringe patterns into the three color channels: red, green, and blue. The projector projects a color image channel-by-channel periodically and at any time, only one channel/color is projected. To prevent the measurement result from being affected by the surface color of the object, the projector is set in black and white (B/W) mode. By using the projector in this way, we can produce a dynamically shifting B/W fringe pattern at a frequency of 360 Hz. If we further use a higher speed camera and synchronize it with the projector, we can capture three phase shifted fringe patterns at a maximum speed of 120 Hz for real-time 3D shape measurement. In this chapter, the system captures the three fringe images at a lower frequency of 30 Hz due to the limited frame rate of the camera being used.

The phase step α is $2\pi/3$, so the fringe intensity functions for each color channel are:

$$I_r(x, y) = a \left[1 + \cos \left(\frac{2\pi}{p} x - \frac{2\pi}{3} \right) \right] \quad 2.15$$

$$I_g(x, y) = a \left[1 + \cos \left(\frac{2\pi}{p} x \right) \right] \quad 2.16$$

and

$$I_b(x, y) = a \left[1 + \cos \left(\frac{2\pi}{p} x + \frac{2\pi}{3} \right) \right] \quad 2.17$$

where p is the fringe pitch and a is the fringe amplitude. Figure 2.6 shows the fringe pattern generated by the computer.

It should be noted that when projected by the aforementioned projector, the fringe patterns lose their color and become B/W. The fringe images captured by the camera can be represented by the following equations:

$$I_r(x, y) = I'(x, y) + I''(x, y) \cos \left[\phi(x, y) - \frac{2\pi}{3} \right] \quad 2.18$$

$$I_g(x, y) = I'(x, y) + I''(x, y) \cos[\phi(x, y)] \quad 2.19$$

and

$$I_b(x, y) = I'(x, y) + I''(x, y) \cos \left[\phi(x, y) + \frac{2\pi}{3} \right] \quad 2.20$$

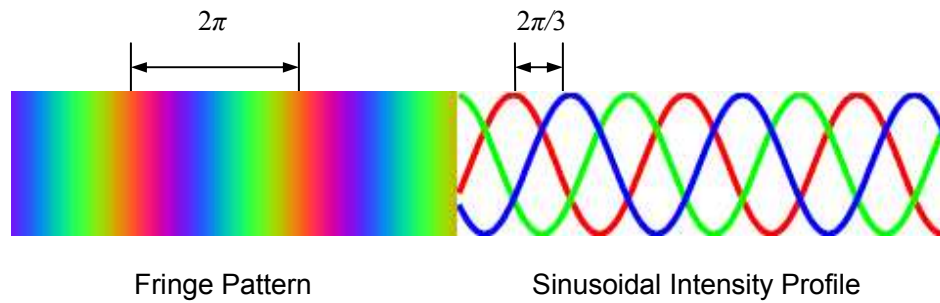


Figure 2.6: Encoded color fringe pattern.

The fringe patterns are projected onto the object sequentially and periodically at a high speed. When grabbing the fringe images, the most important thing is to make sure every single image captured by the camera should have the fringe information of only one channel. Otherwise phase map reconstruction will not be correct. For this reason, the system needs to be synchronized and the exposure time of the camera needs to be set exactly the same as the duration of the projection time for each channel.

The CCD camera utilized in this chapter is controlled by a frame grabber (Matrox Meteor II/Digital). By using Matrox Imaging Library, the camera can be set in the trigger mode, which means only when a trigger signal is generated and sent to the frame grabber, can the camera grab an image. To generate the trigger signal, a simple circuit was designed, which takes the video refresh signal of the projector as the input signal.

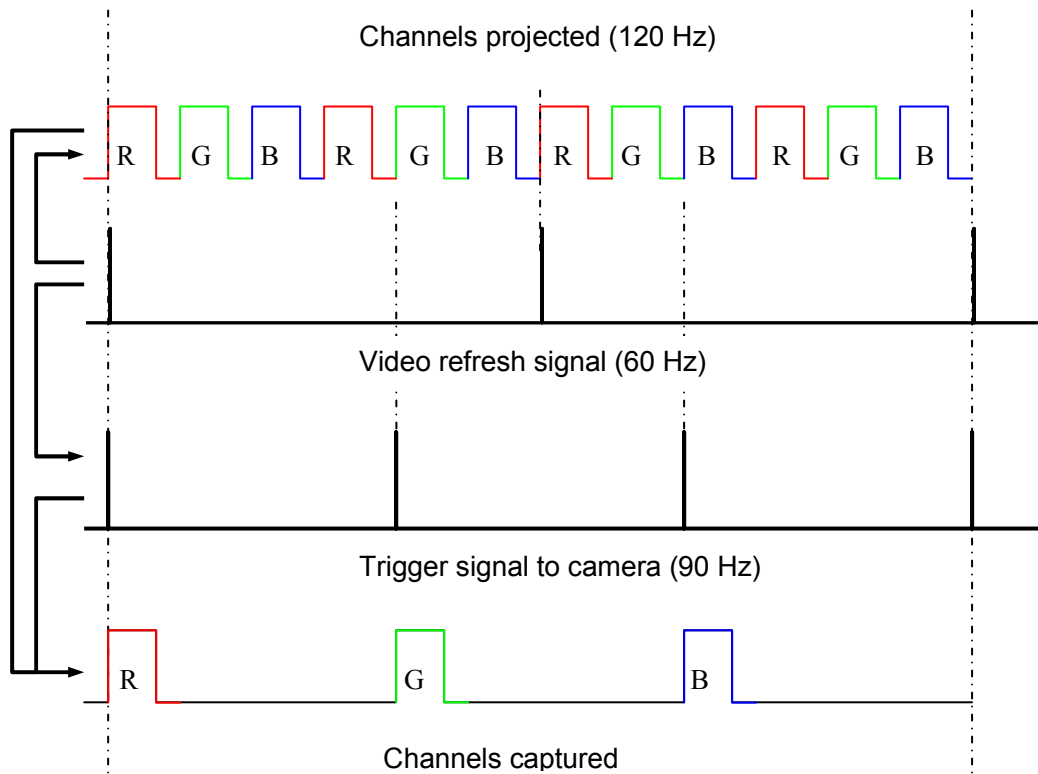


Figure 2.7: System timing chart.

Figure 2.7 shows the system timing chart. For every single refresh pulse, the projector projects Red, green, and blue channels twice. For every four Red, green, and blue cycles, the camera captures three fringe images, which are used to reconstruct one phase map based on the three-step algorithm. Since the video refresh rate is set to 60 Hz, the projecting frequency is 120 Hz and the system can reconstruct 3D shape of an object at a frame rate up to 30 frames per second. Figure 2.8 shows an example of 3D measurement procedure by using this system.

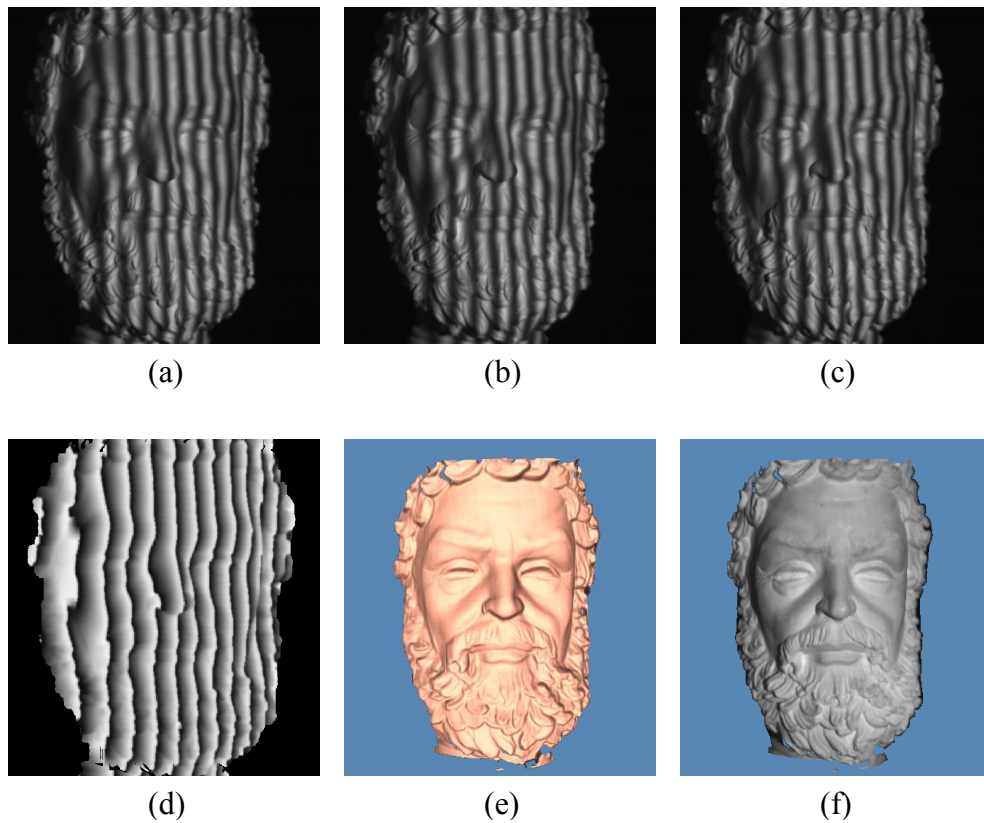


Figure 2.8: Example of 3D reconstruction. (a)-(c) Three fringe images. (d) Wrapped phase map. (e) Reconstructed 3D model. (f) Reconstructed 3D model with texture.

2.3 Linear Calibration and Coordinate Reconstruction

System coordinate reconstruction converts the phase map to x , y , and z coordinates of the object surface. The method described in this section is based on a linear camera calibration method that uses a Matlab toolbox developed by Jean-Yves Bouguet. For projector calibration, a new method is introduced to make a projector “capture” images as a camera. With a series of checkerboard images “captured” by the projector, we can use the same Matlab toolbox to calibrate the projector.

A typical pinhole camera model has several intrinsic parameters including focal length, principle point, skew coefficient and distortions, as well as extrinsic parameters such as the rotation and translation matrices.

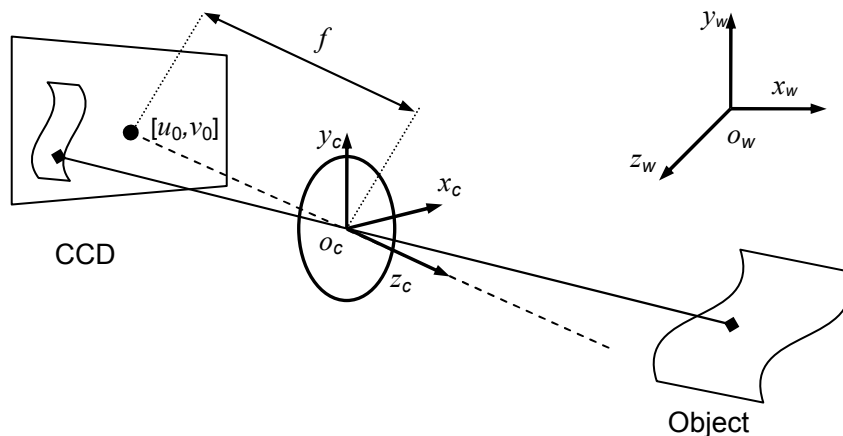


Figure 2.9: Camera coordinate system and world coordinate system.

Figure 2.9 shows the relationship between the camera coordinate system $[o_c \ x_c \ y_c \ z_c]$ and the world coordinate system $[o_w \ x_w \ y_w \ z_w]$. f is the focal length and $[u_0 \ v_0]$ is the principle point. Based on this model, the conversion between a

point on an object and the corresponding projection on the camera sensor can be expressed as:

$$sI = A[R, t]X^w \quad 2.21$$

where $I = [u \ v \ 1]^T$ is the image coordinate matrix, X^w is the world coordinate matrix, A is intrinsic parameter matrix, and $[R \ t]$ is the extrinsic parameter matrix. The intrinsic parameter matrix has the following form

$$A = \begin{bmatrix} f_u & \alpha & u_0 \\ 0 & f_v & v_0 \\ 0 & 0 & 1 \end{bmatrix} \quad 2.22$$

where f_u and f_v are focal lengths along the u and v axes of the image plane respectively, u_0 and v_0 are coordinates of the principle point, and α is the product of skew coefficients defining the angles between the u and v pixel axes and f_u . The extrinsic parameter matrix is composed of the following rotation and the translation matrices:

$$\text{Rotation matrix} \quad R = \begin{bmatrix} r_{11} & r_{12} & r_{13} \\ r_{21} & r_{22} & r_{23} \\ r_{31} & r_{32} & r_{33} \end{bmatrix} \quad 2.23$$

and

$$\text{Translation matrix} \quad t = [t_1 \ t_2 \ t_3]^T \quad 2.24$$

It should be noted that a linear calibration method does not consider lens distortion. A nonlinear calibration method, which takes lens distortion into consideration, will be discussed in Chapter 3.

To obtain the intrinsic and extrinsic parameters of the camera using the Matlab toolbox, a series of checkerboard images are captured. The checkerboard used in this

research consists of 15×15 mm squares in alternating blue and red colors. Figure 2.10 shows the checkerboard pattern and a checkerboard image captured by the camera.

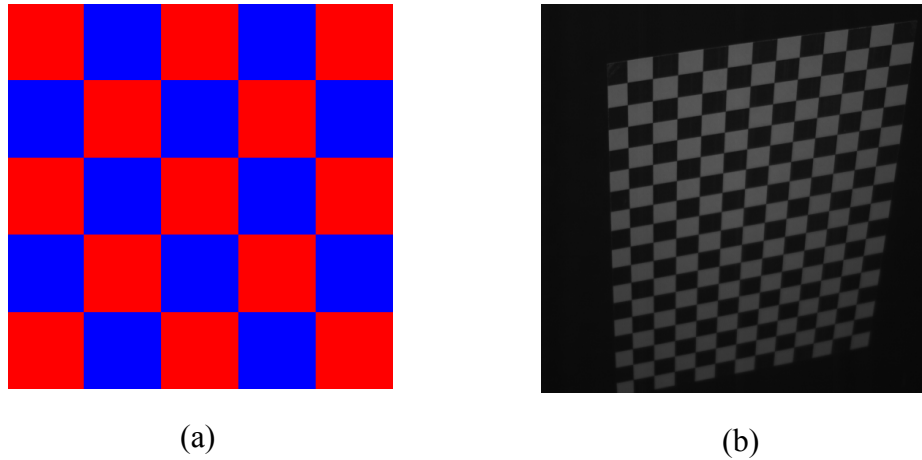


Figure 2.10: Checkerboard used for calibration. (a) Red/Blue checkerboard. (b) Checkerboard image.

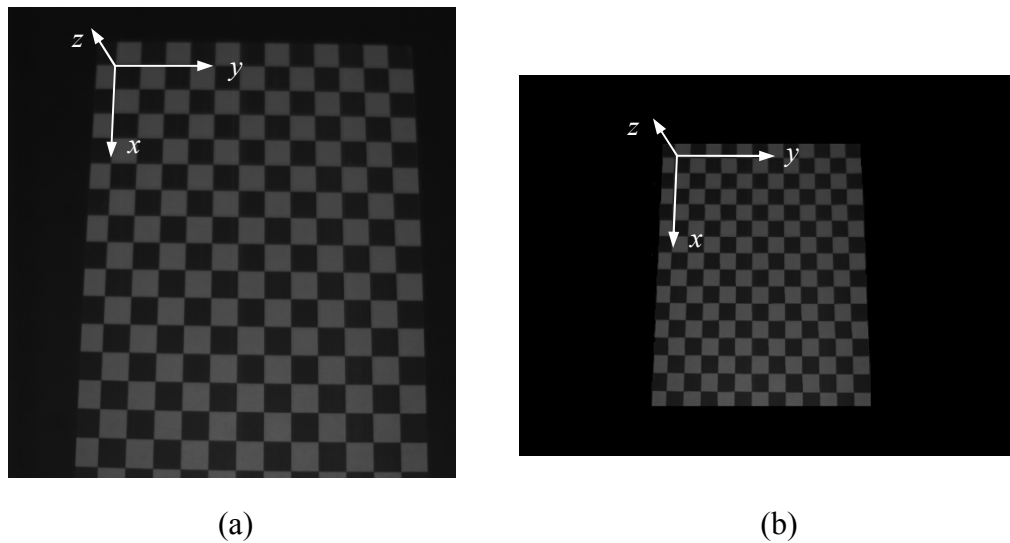


Figure 2.11: World coordinate system in (a) A CCD checkerboard image (b) A DMD checkerboard image.

After extraction of corner coordinates for every checkerboard image, the intrinsic parameters can be obtained in the unit of pixels. Extrinsic parameters are calculated based on an additional checkerboard image. The extraction of corner coordinates needs to be done once more to determine the extrinsic parameters expressed as the rotation and translation matrices. The world coordinate system in the CCD and DMD images are shown in Figure 2.11. The x - y plane is the checkerboard plane and the z -axis is perpendicular to the checkerboard plane pointing outward.

Projector calibration is usually more laborious than camera calibration because the projector cannot capture checkerboard images directly as a camera does. However, after a method for absolute phase measurement is introduced to make the projector “capture” a series of images, the projector calibration procedure becomes much simpler.

In order to calculate the absolute phase, an additional centerline image is captured. This centerline is located in the middle of the DMD chip. Once this centerline image is captured by the camera, the location of the pixels that represent the centerline in the image is first detected. Then, in the phase map reconstructed from the three fringe images, the phase values at the centerline pixels are averaged and this average phase value is subtracted from the phase value of every pixel in the phase map. Thus, an absolute phase map, in which the phase values at the centerline pixels are zero, is generated. This absolute phase map allows us to determine the correspondence between the pixels on the CCD sensor and the pixels on the DMD chip. For each pixel on the CCD sensor, a line, either vertical or horizontal depending on the direction of the projected fringe pattern, on the DMD chip can be identified. To determine the pixel-to-pixel correspondence between the CCD sensor and DMD chip, a total of eight patterns with four in the vertical direction

and four in the horizontal direction are needed to be projected as shown in Figure 2.12. By establishing such a one-to-one map between the CCD sensor and the DMD chip, every pixel in a CCD image is correlated to a DMD pixel. In other words, if we already have a CCD checkerboard image, using the method described above, a corresponding DMD image can be generated, which is regarded as an image “captured” by the projector.

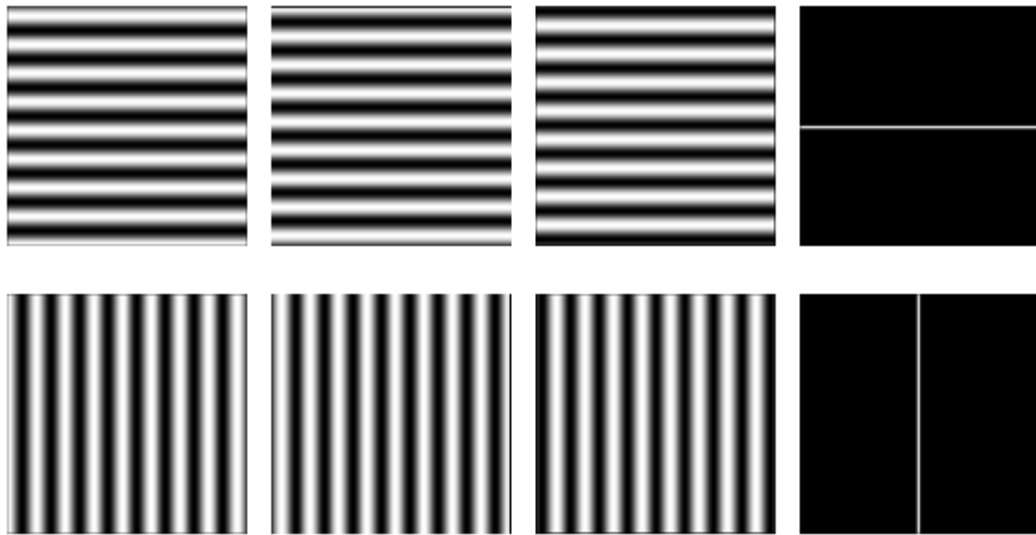


Figure 2.12: Eight images used to determine CCD and DMD pixel correspondence.

After the procedure introduced above, the intrinsic and extrinsic parameters of the projector can be estimated by using the same toolbox used for the camera. It should be noted that in order to establish the coordinate relationship between the camera, the projector, and the world coordinate system, the DMD image used to determine the extrinsic parameters of the projector has to be the DMD image that corresponds to the CCD image used to determine the extrinsic parameters of the camera. Figure 2.13 shows

the relationship between these three coordinate systems. Once the intrinsic and extrinsic parameters of both the camera and the projector are obtained, we can use them to reconstruct the 3D shape of the object. While eight checkerboard images are required during the calibration process, only four images (three fringe images plus a centerline image) are needed for normal measurement.

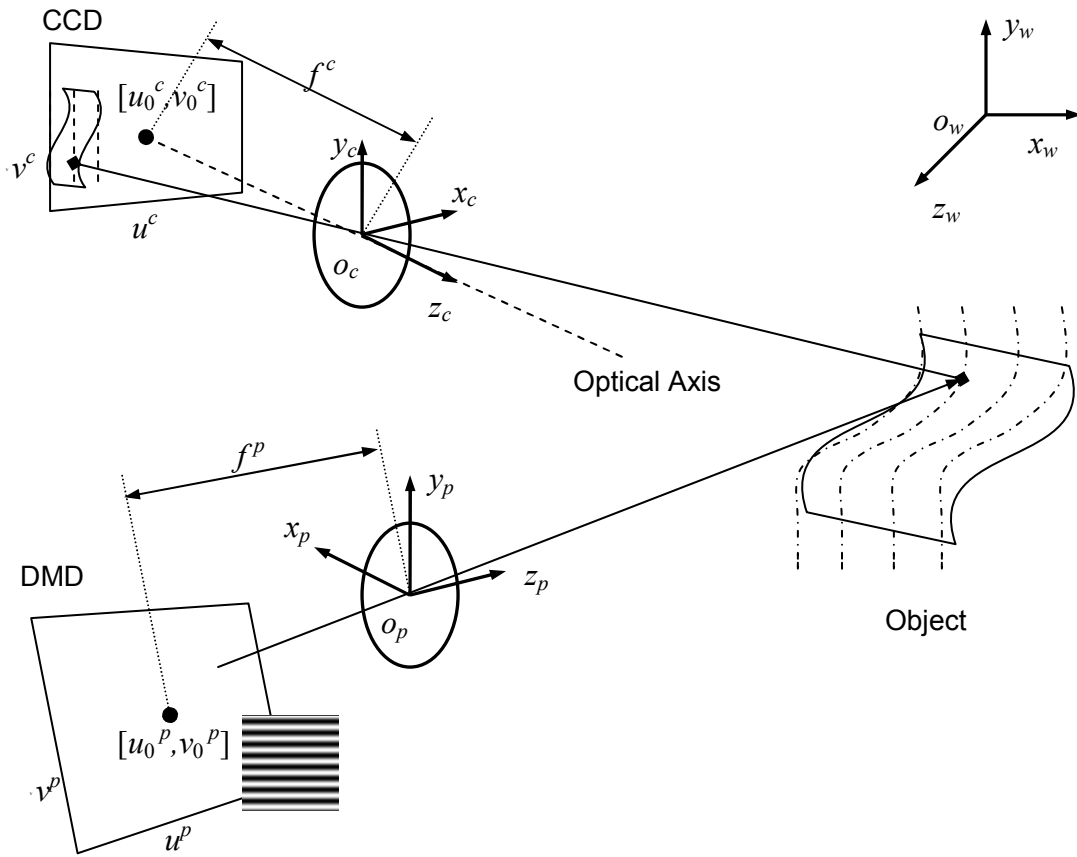


Figure 2.13: Relationship between the three coordinate systems.

For coordinate reconstruction, let us first rewrite Eq. (2.21) in the following form:

$$s^c \begin{bmatrix} u^c & v^c & 1 \end{bmatrix}^T = A^c \begin{bmatrix} R^c & t^c \end{bmatrix} \begin{bmatrix} X_w & Y_w & Z_w & 1 \end{bmatrix}^T \quad 2.25$$

where A^c , R^c and t^c represent the intrinsic and extrinsic parameters of the camera. For any arbitrary pixel, u^c and v^c are its pixel coordinates and are known. A^c and R^c are 3×3 matrices and t^c is a 3×1 matrix. There are three equations in Eq. (2.25) with four unknowns: s^c , X_w , Y_w , and Z_w . For the projector side, we can write the following equation that is similar to Eq. (2.25):

$$s^p \begin{bmatrix} u^p & v^p & 1 \end{bmatrix}^T = A^p \begin{bmatrix} R^p & t^p \end{bmatrix} \begin{bmatrix} X_w & Y_w & Z_w & 1 \end{bmatrix}^T \quad 2.26$$

where A^p , R^p and t^p represent the intrinsic and extrinsic parameters of the projector. There are also three equations in Eq. (2.26) but with additional three unknowns: s^p , u^p , and v^p . Combining Eqs. (2.25) and (2.26), we have six equations with seven unknowns. Therefore, an additional equation is needed in order to solve these equations for X_w , Y_w and Z_w . This additional equation can be found by using the absolute phase method. That is u^p (when vertical fringe patterns are used) or v^p (when horizontal fringe patterns are used) can be determined from the absolute phase value of pixel $\begin{bmatrix} u^c & v^c \end{bmatrix}$. In our system, the fringe pattern is projected vertically due to hardware design. As a result, u^p is determined by the corresponding phase value. With u^p determined, there are now six equations and six unknowns left (s^c , X_w , Y_w , Z_w , s^p , and v^p) in Eqs. (2.25) and (2.26) and therefore the equations can be solved.

2.4 Summary

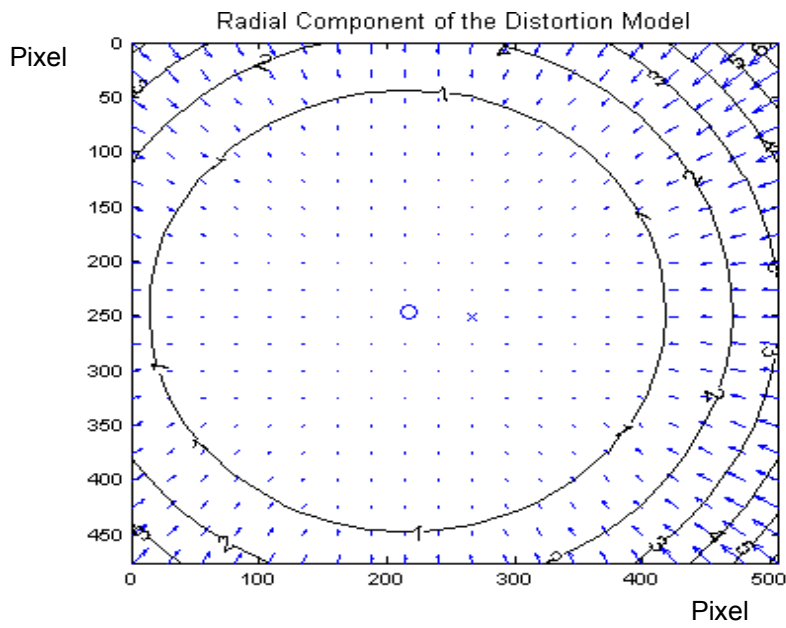
This chapter introduced the fundamental theory of phase shifting algorithm and provided an overview of our system setup. In Section 2.3, the linear calibration method and the 3D reconstruction method were described in details. This linear calibration method is the basis of the nonlinear calibration method to be explained in details in Chapter 3.

Chapter 3 Nonlinear Calibration

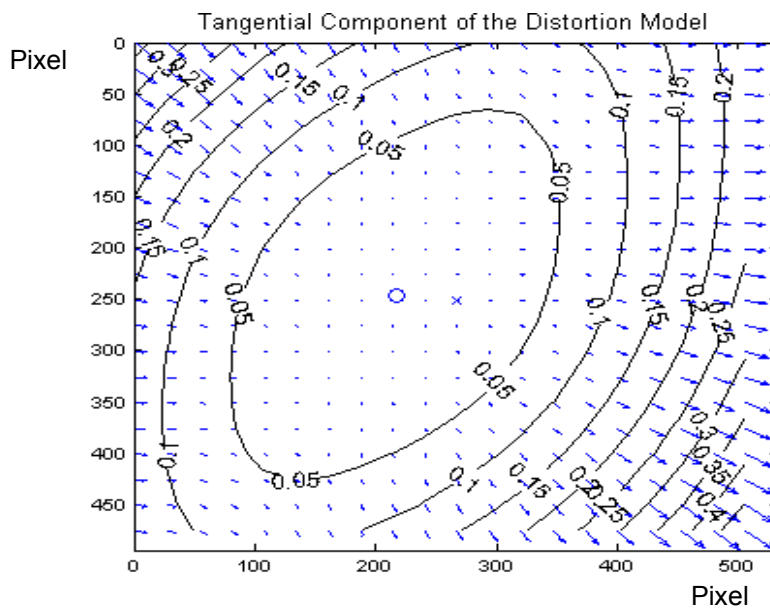
System calibration is usually a complicated and time-consuming procedure, especially when a projector is involved. Unlike camera calibration, projector calibration is less well understood and established. The method introduced in Chapter 2 makes projector calibration much faster and more systematic than previously proposed methods. However, this calibration method uses only a linear model and does not consider lens distortion when computing the intrinsic and extrinsic parameters and reconstructing 3D coordinates. To further improve system accuracy, lens distortion, as the most dominant error source of the system, has to be considered in calibration and coordinate reconstruction. This chapter focuses on the nonlinear calibration of camera and projector. Lens distortion parameters are first determined using the Matlab toolbox and then used in coordinate reconstruction.

3.1 Fundamental Concepts of Lens Distortion

Lens distortions usually can be modeled as radial and tangential distortions, as illustrated in Figure 3.1. Each arrow represents the effective displacement caused by lens distortion. Figure 3.2 shows an example of the original checkerboard image together with the same image after lens distortion is corrected by software. Checking the line and the circle carefully, we notice that lens distortion is most serious in the corner areas. In most cases, lens distortion can be adequately described by the first two terms of radial distortion.

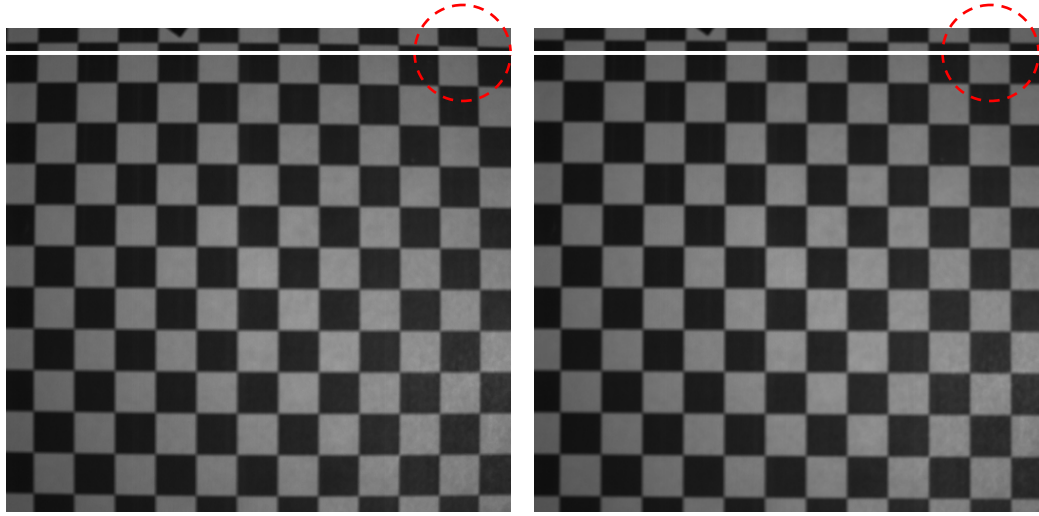


(a)



(b)

Figure 3.1: Example of radial and tangential lens distortion. (a) Radial distortion. (b) Tangential distortion.



(a) Before correction

(b) After correction

Figure 3.2: Checkerboard image before and after lens distortion correction. (a) Before nonlinear correction. (b) After nonlinear correction.

To construct a nonlinear camera model that takes lens distortion into consideration, assume P to be a point on the object surface with a coordinate vector $X^c = [X_c \ Y_c \ Z_c]$ in the camera coordinate system. Let x_n be the normalized projection on the image plane. Then, in a linear model:

$$x_n = \begin{bmatrix} X_c / Z_c \\ Y_c / Z_c \end{bmatrix} = \begin{bmatrix} x \\ y \end{bmatrix} \quad 3.1$$

If we assume $r^2 = x^2 + y^2$, after including the lens distortion the new normalized coordinate x_d is defined as follows:

$$x_d = \begin{bmatrix} x_d(1) \\ x_d(2) \end{bmatrix} = (1 + kc(1)r^2 + kc(2)r^4 + kc(5)r^6)x_n + dx \quad 3.2$$

where dx is the tangential distortion defined as:

$$dx = \begin{bmatrix} 2kc(3)xy + kc(4)(r^2 + 2x^2) \\ kc(3)(r^2 + 2y^2) + 2kc(4).xy \end{bmatrix} \quad 3.3$$

In Eqs. (3.2) and (3.3), kc is a vector that contains both radial and tangential distortion coefficients. Once distortion is applied, the pixel coordinates $[u \ v]$ of the projection on the image plane is:

$$\begin{bmatrix} u \\ v \end{bmatrix} = \begin{bmatrix} f_u(x_d(1) + \alpha x_d(2)) + u_0 \\ f_v x_d(2) + v_0 \end{bmatrix} \quad 3.4$$

or

$$\begin{bmatrix} u \\ v \\ 1 \end{bmatrix} = A \begin{bmatrix} x_d(1) \\ x_d(2) \\ 1 \end{bmatrix} \quad 3.5$$

where A is the camera intrinsic parameter matrix as shown in Eq. (2.22).

Table 3.1 compares the intrinsic parameters when different numbers of distortion coefficients are used. From this table we can see that the intrinsic parameters have an obvious difference between the linear model and the nonlinear model. But between the two nonlinear models (one uses only one distortion coefficient and the other uses four), the difference is not that obvious. Actually, in the latter two models, the parameter fluctuations are within the uncertainties of the estimated parameters.

Table 3.2 shows the first four distortion coefficients along with their estimation uncertainties. The second and the third coefficients are approximately equal to or even larger than the uncertainties, which makes them unreliable. The fourth coefficient is too small compared to the first one, although it is two times larger than its uncertainty. Therefore, this camera nonlinear model can be best described by only the first distortion

coefficient, because the inclusion of any additional coefficient not only would not help but also would cause numerical instability [23].

Table 3.1: Camera intrinsic parameters with different distortion models.

	Linear	Nonlinear $kc(1)$ only	Nonlinear $kc(1)$ to $kc(4)$
f_u	1675.60906	1660.52675	1662.48215
f_v	1671.96606	1656.82137	1659.16998
u_0	255.08628	215.34671	216.78928
v_0	241.57142	250.69715	247.52404
α	0.00000	0.00000	0.00000
$kc(1)$	0.00000	-0.31656	-0.32466

Table 3.2: Camera lens distortion coefficients.

	$kc(1)$	$kc(2)$	$kc(3)$	$kc(4)$
Coefficient	-0.32466	-0.23585	0.00037	0.00161
Uncertainty (\pm)	0.02560	0.64473	0.00038	0.00054

3.2 Nonlinear Calibration of Camera

The lens used on the camera is a 16-mm optical lens. From Eqs. (2.25) and (3.5), the following relationship is obtained:

$$\begin{bmatrix} x_d^c(1) \\ x_d^c(2) \\ 1 \end{bmatrix} = \frac{1}{s^c} [R^c, t^c] \begin{bmatrix} X_w & Y_w & Z_w & 1 \end{bmatrix}^T = \frac{1}{s^c} [X_c \ Y_c \ Z_c]^T \quad 3.6$$

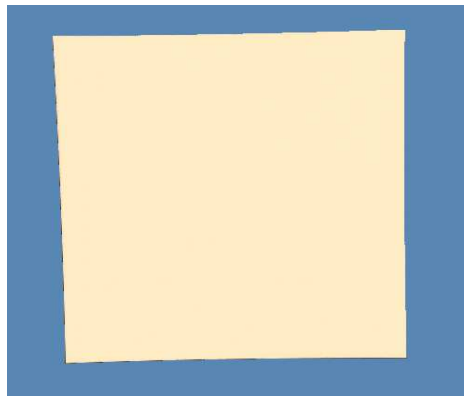
where $[X_c \ Y_c \ Z_c]$ is the coordinates of a point on the object surface in the camera coordinate system. s^c is a constant used to normalize these coordinates. Obviously, in this case $s^c = Z_c$ and the new expression is:

$$\begin{bmatrix} x_d^c(1) \\ x_d^c(2) \\ 1 \end{bmatrix} = \begin{bmatrix} X_c / Z_c \\ Y_c / Z_c \\ 1 \end{bmatrix} = x_n^c \quad 3.7$$

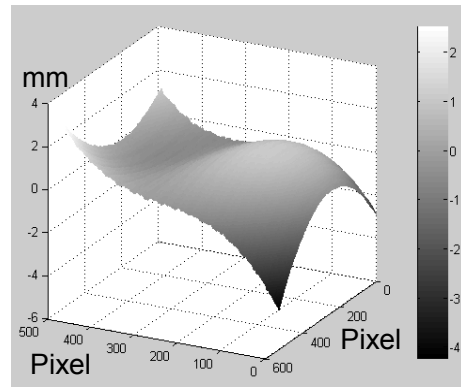
where x_n is the same vector as shown in Eq. (3.1). According to Eq. (3.2), only when $kc(n) = 0$, $n = 1, 2, 3, 4, 5$, Eq. (3.7) is tenable. It is consistent with the fact that the calibration method we used before is a linear method.

To evaluate the effect of lens distortion, a flat white board was scanned from different perspectives. Using a least-square plane fitting method, we found the error map, which is the deviation of the measured data from the fitted plane. Two examples of the error map are shown in Figure 3.3. In these two examples, the flat board is set in the same orientation (approximately perpendicular to the optical axis of the camera), but at different distances from the camera. Notice that the error in the second map is much larger than the first one. This is because the lens distortion effect is proportional to the field-of-view of the camera, which in turn is proportional to the distance between the

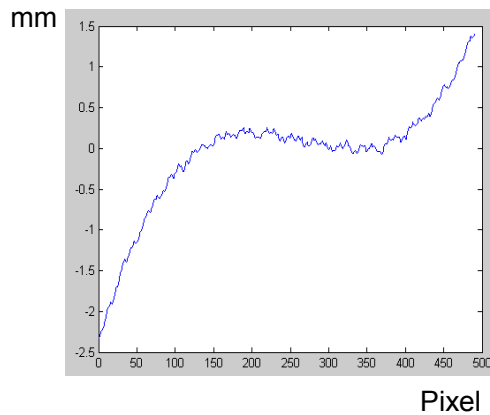
object and the camera. The longer the distance is, the larger the error is. Inside the recommended measurement range of our system, the error caused by lens distortion is usually in a range from 5 to 10 mm if a linear model is used. The error is most severe in the corner areas of the camera image.



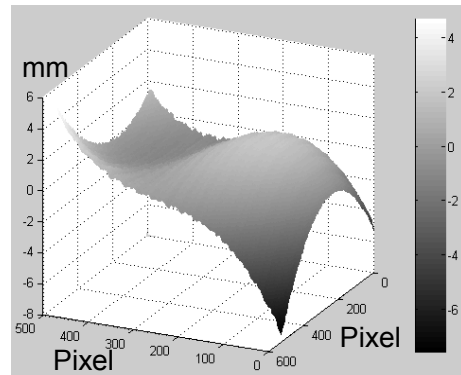
(a)



(b)



(c)



(d)

Figure 3.3: Error maps of measured flat board. (a) 3D model of a flat board at a near position. (b) Error map when the flat board is at the near-position. (c) Cross section of the near-position error map at the 450th row. (d) Error map when the flat board is placed at a further position.

To eliminate the error caused by lens distortion, a reasonable lens distortion model needs to be selected with the right combination of lens distortion coefficients. The second-order symmetric radial distortion model, which uses only the first radial distortion coefficient, is a viable model. It is often used when low distortion optical systems are used, or when only a few checkerboard images are available for calibration. Another commonly used lens distortion model is the 4th order symmetric radial distortion model with no tangential component. In our case, Table 3.2 shows that the tangential components are significantly smaller than the radial components and the estimation uncertainties of the 4th order components are even larger than their corresponding error coefficients. Therefore, the 4th order radial distortion model is not reliable and should not be used. Due to these reasons, the second-order symmetric radial distortion model is selected for this research. According to this model, the normalized coordinates of Eq. (3.2) become:

$$x_d^c = \begin{bmatrix} x_d^c(1) \\ x_d^c(2) \end{bmatrix} = (1 + kc(1)r^2)x_n^c \quad 3.8$$

Once the distortion model is determined, the important issue is how to integrate this distortion model into the reconstruction algorithm. Obviously, Eq. (2.25) cannot be applied directly. Instead, a new relationship can be found from Eqs. (3.1), (3.5) and (3.8). For convenience, Eq. (3.1) is rewritten into the following expression:

$$Z_c \begin{bmatrix} x_n^c(1) \\ x_n^c(2) \\ 1 \end{bmatrix} = \begin{bmatrix} X_c \\ Y_c \\ Z_c \end{bmatrix} = [R^c, \quad t^c] [X_w \quad Y_w \quad Z_w \quad 1]^T \quad 3.9$$

where R^c and t^c are the rotation matrix and the translation matrix given in Table 3.3.

Table 3.3: Camera extrinsic parameters.

Translation matrix	$t^c = [-45.264533 \quad -105.645490 \quad 781.788688]$
Rotation matrix	$R^c = \begin{bmatrix} -0.019888 & 0.998729 & -0.046302 \\ 0.999492 & 0.018708 & -0.025785 \\ -0.024886 & -0.046792 & -0.998595 \end{bmatrix}$

Using the intrinsic parameter matrix A and the pixel coordinates on the image plane $[u \quad v \quad 1]$, through Eq. (3.5), $x_d^c = [x_d^c(1) \quad x_d^c(2) \quad 1]$ can be uniquely determined. By applying Eq. (3.8) to solve for the x_n^c value, Eq. (3.9) can be used to calculate world coordinates $[X_w \quad Y_w \quad Z_w]$.

In Eq. (3.9) there are four unknowns but only 3 linear equations. Therefore, one more equation is needed to solve for the coordinates. Let us first assume that the lens distortion of the projector is not considered. Then Eq. (2.26) can be used to solve the equations. Assuming $[X_w \quad Y_w \quad Z_w]^T = X^w$ and $x_n^c = [x_n^c(1) \quad x_n^c(2) \quad 1]$ and using the expressions in Eqs. (2.23) and (2.24), we have the equations on the camera side:

$$Z_c x_n^c = [R^c, \quad t^c] [X^w, \quad 1]^T \quad 3.10$$

$$Z_c x_n^c = R^c X^w + t^c \quad 3.11$$

$$Z_c x_n^c(i) = \sum_{k=1}^3 R_{ik}^c X_k^w + t_i^c, \quad i = 1, 2, 3 \quad 3.12$$

On the projector side, let $[u^p \quad v^p \quad 1] = I^p$:

$$s^p I^p = A^p [R^p, \quad t^p] [X^w, \quad 1]^T \quad 3.13$$

$$s^p I^p = A^p R^p X^w + A^p t^p \quad 3.14$$

$$s^p I^p = E^p X^w + F^p \quad 3.15$$

where $E^p = A^p R^p$, $F^p = A^p t^p$

$$s^p I_i^p = \sum_{k=1}^3 E_{ik}^p X_k^w + F_i^p, \quad i = 1, 2, 3 \quad 3.16$$

From Eqs. (3.12) and (3.16), we have:

$$HX^w = b \quad 3.17$$

where H is a 3×3 matrix and b is a 3×1 matrix defined as:

$$H_{ij} = R_{3j}^c x_n^c(i) - R_{ij}^c, \quad i = 1, 2 \quad 3.18$$

$$H_{3j} = E_{3j}^p I_1^p - F_{1j}^p \quad 3.19$$

$$b_i = t_i^c - x_n^c(i) t_3^c, \quad i = 1, 2 \quad 3.20$$

$$b_i = F_1^p - I_1^p F_3^p \quad 3.21$$

Then,

$$X^w = H^{-1}b \quad 3.22$$

By using the new algorithm above that takes lens distortion into consideration, the reconstruction of the world coordinates becomes much more accurate. Figure 3.4 shows the error maps after the nonlinear algorithm is applied to the same data as that in Figure 3.3. The error caused by lens distortion has been significantly reduced. When the flat board is not perpendicular to the optical axis, some parts on the flat board are closer to the camera than other parts. Because the coordinate error changes with the distance from the camera to the object, the error maps show in different shapes when the flat board is set in various orientations, as shown in Figure 3.5. Table 3.4 shows the RMS errors of the six 3D models before and after the camera nonlinear calibration algorithm is applied.

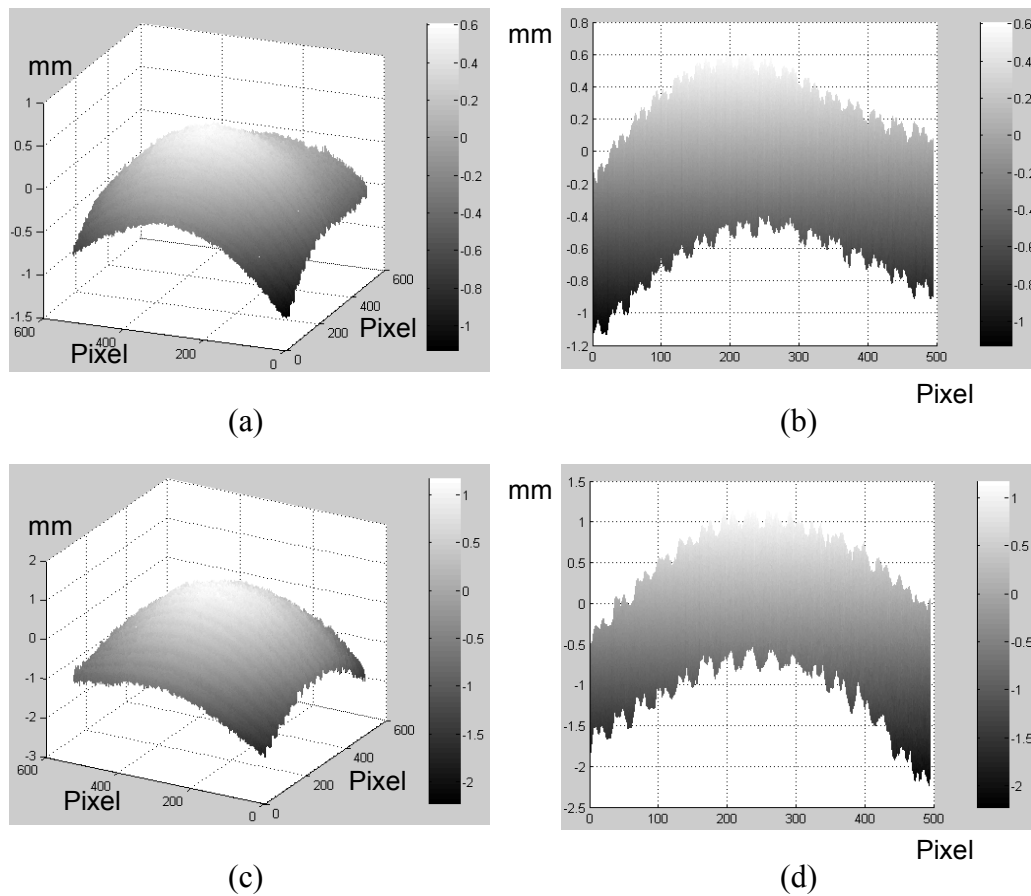


Figure 3.4: Error maps after the camera nonlinear calibration algorithm is applied. (a)-(b) The error at a near position. (c)-(d) The error map at a further position.

From the analysis above, solving linear equations is still the last step of the nonlinear calibration procedure. This is because we included the lens distortion information in the normalized coordinate vectors, but not in the reconstruction calculation. This approach separates the nonlinear part from the linear part, so that the relationship between the camera and the projector is as simple as that of the linear model and the algorithm still has a low complexity.

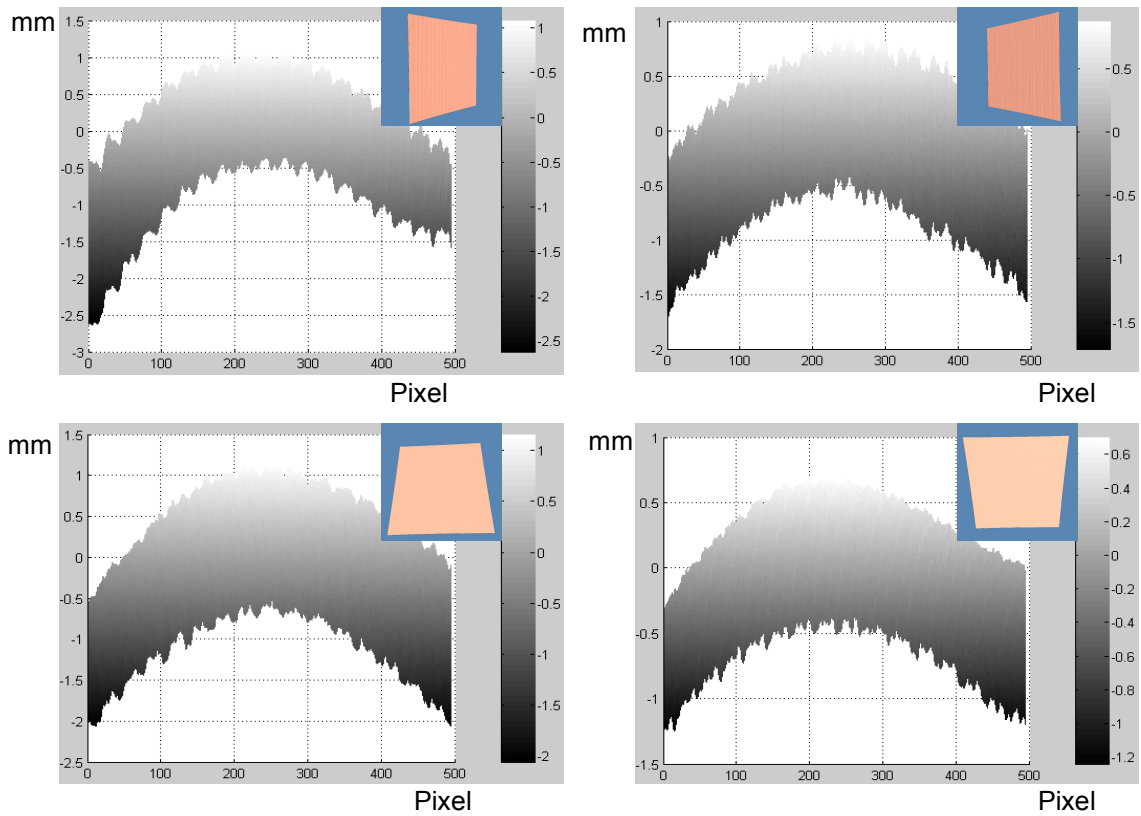


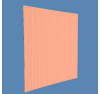





Figure 3.5: Error maps of the flat board measured in different orientations.

Table 3.4: RMS errors of the flat board measured in different orientations. RMS (L): Linear calibration; RMS (CNL): Camera nonlinear calibration.

3D model	RMS (L)	RMS (CNL)	3D model	RMS (L)	RMS (CNL)
#1 	1.2394	0.5853	#2 	0.6899	0.3088
#3 	1.4113	0.6010	#4 	0.6946	0.4597
#5 	1.1683	0.6106	#6 	0.8845	0.3636

3.3 Nonlinear Calibration of Projector

Projector lens has the same lens distortion problem as the camera lens. The fringe pattern is distorted by the lens after being projected. The distortion has already been formed before the fringe reached the object. That is a reverse procedure compared to the camera. Taking the same idea introduced in the case of camera lens, equations of the same format can be written. Combined with the equations for the camera as shown in Eq. (3.12), the projector lens distortion can be corrected in the same way.

To calculate the intrinsic and extrinsic parameters, the method described in Chapter 2 is used to “capture” more than ten projector images of the checkerboard. Then the Matlab calibration toolbox is used to estimate the parameters. The intrinsic parameters with different distortion models are shown in Table 3.5 and the distortion coefficients are listed in Table 3.6.

Table 3.5: Projector intrinsic parameters with different distortion models.

	Linear	Nonlinear only with $kp(1)$	Nonlinear with $kp(1)$ to $kp(4)$
f_u	1602.43870	1596.26610	1599.87654
f_v	1601.42411	1594.03890	1623.89740
u_0	209.66603	208.38563	201.83723
v_0	-139.42807	-168.73926	-191.95255
α	0.00000	0.00000	0.00000
$kp(1)$	0.00000	-0.02722	0.05035

Table 3.6: Projector lens distortion coefficients.

	$kp(1)$	$kp(2)$	$kp(3)$	$kp(4)$
Coefficient	0.05035 (-0.02722)	0.02697	-0.02882	-0.00119
Uncertainty (\pm)	0.03611 (0.00913)	0.04960	0.00735	0.00110

When choosing different distortion models, the distortion coefficients obtained would not be exactly identical. In the case of the camera, this situation is not significant and we could easily choose the optimal distortion model. However, the projector lens distortion coefficients change significantly in different models. When the distortion model with four coefficients is chosen, even the first coefficient is not reliable because the uncertainty is more than 50 percent. For the distortion model with just one coefficient, we can obtain a reliable $kp(1)$ value, which only has a uncertainty of about 25 percent. Therefore, the same second-order symmetric radial distortion model (only $kp(1) = -0.02722$ is utilized) used for the camera lens is applied to the projector lens as well. Table 3.7 lists the extrinsic parameters from this model.

Table 3.7: Projector extrinsic parameters.

Translation matrix	$t^p = [-64.512100 \quad 120.194885 \quad 777.905051]$
Rotation matrix	$R^p = \begin{bmatrix} -0.008372 & 0.999508 & -0.030218 \\ 0.999905 & 0.008699 & 0.010696 \\ 0.010954 & -0.030126 & -0.999486 \end{bmatrix}$

Following the same procedure applied to the camera, through Eq. (3.5), coordinate vector with distortion $x_d^p = [x_d^p(1) \ x_d^p(2) \ 1]$ is calculated first. Then from Eq. (3.23), we obtain the normalized coordinate vector x_n^p in the projector coordinate system.

$$x_d^p = \begin{bmatrix} x_d^p(1) \\ x_d^p(2) \end{bmatrix} = (1 + kp(1)r^2)x_n^p \quad 3.23$$

Using extrinsic parameters to write Eqs. (3.24)-(3.26) as following and combining projector side equation Eq. (3.26) with the camera side equation Eq. (3.12), the world coordinates can be reconstructed.

$$Z_p x_n^p = [R^p, \ t^p] X^w, \ 1]^T \quad 3.24$$

$$Z_p x_n^p = R^p X^w + t^p \quad 3.25$$

$$Z_p x_n^p(i) = \sum_{k=1}^3 R_{ik}^p X_k^w + t_i^p \quad i = 1, 2, 3 \quad 3.26$$

In order to calculate the normalized coordinate vector in Eq. (3.5), pixel coordinates in both u and v directions are required. Even though in the final step only one component of the normalized coordinate vector is useful, both of them have to be known in advance. Therefore, eight images are needed to solve for the pixel coordinates, four images for the u direction and four for the v direction. Figure 3.6 is the final error map of a flat board with nonlinear calibration on both sides, as compared to results of linear calibration and results of nonlinear calibration only on the camera side. The error due to lens distortion is apparently further reduced after applying nonlinear calibration to both the camera and projector lenses. The drawback is that too many images are required and

the fringe patterns need to be switched just for a single 3D data. Therefore, this approach is not feasible for real-time measurement of slowly moving objects.

One way to eliminate the need for these four additional images is to use an iterative reconstruction. With this approach, only four images are captured, three fringe images plus one centerline image. When using Eq. (3.5), only one component of the normalized coordinate vector, or the pixel coordinate in one direction, can be determined. Instead of using four more additional images, we just assume that the unknown pixel coordinate is at the center of the DMD image along the same direction. For instance, in this research the resolution of the projector is 1024×768 pixels, if we do not know the pixel coordinates in the direction which has 768 pixels, we just assume the value to be 384 no matter what it really is. This estimation will definitely introduce reconstruction error to the world coordinate result X^w . However, the X^w obtained from this first iteration is not the final result. Substitute X^w into the following equation to find $X^p = [X_p \ Y_p \ Z_p]$ and then normalize X^p to obtain a new x_n^p :

$$\begin{bmatrix} X_p \\ Y_p \\ Z_p \end{bmatrix} = [R^p, \ t^p] [X_w \ Y_w \ Z_w \ 1]^T \quad 3.27$$

Using x_n^p in Eqs. (3.5) and (3.23) inversely, the pixel position of this point can be recovered in both u and v dimensions. Using these new pixel coordinates to calculate world coordinates again, a new X^w is obtained. After several such iterations, the result will converge. This approach uses an initial guess and borrows the constraint from the camera side to determine the final world coordinates iteratively. According to our experience, iterating just once is adequate to achieve an acceptable accuracy.

Figure 3.6 (d) is the error map obtained after a single iteration. Comparing with the result reconstructed by eight images, neither the error map nor the world coordinates show obvious differences. In this case, however, the projector lens only has a small distortion. Otherwise, only iterating once may not be sufficient to generate an acceptable result.

The first approach needs too many images and the second approach is not that efficient. To solve the problem systematically with no more than four images, a novel approach is proposed, in which a cubic equation is used to replace those linear equations. Rewrite Eq. (3.4) to obtain the relationship between the normalized coordinate vector and the pixel coordinates as follows:

$$x_d^p = \begin{bmatrix} x_d^p(1) \\ x_d^p(2) \end{bmatrix} = \begin{bmatrix} (u^p - u_0^p) / f_u^p \\ (v^p - v_0^p) / f_v^p \end{bmatrix} \quad 3.28$$

Substituting Eq. (3.28) into Eq. (3.23), we have

$$\begin{bmatrix} (u^p - u_0^p) / f_u^p \\ (v^p - v_0^p) / f_v^p \end{bmatrix} = (1 + kp(1)r^2)x_n^p \quad 3.29$$

where $r^2 = (X_p / Z_p)^2 + (Y_p / Z_p)^2$ and $x_n^p = [X_p / Z_p \quad Y_p / Z_p]^T$, $[X_p \quad Y_p \quad Z_p]$ are the coordinates of a point on the object in the projector coordinate system. With four images, only one dimension of the pixel coordinate is known. Using the u -axis, Eq. (3.29) becomes a cubic equation:

$$e = \frac{u^p - u_0^p}{f_u^p} = \left\{ 1 + kp(1) \left[\left(\frac{X_p}{Z_p} \right)^2 + \left(\frac{Y_p}{Z_p} \right)^2 \right] \right\} \frac{X_p}{Z_p} \quad 3.30$$

Eq. (3.30) has three unknowns: X_p , Y_p and Z_p , which are related to X_w , Y_w and Z_w through the extrinsic parameters of the projector. Combining Eqs. (3.11), (3.25), and

(3.30), the coordinates of the object point can be solved in the projector coordinate system. Since the extrinsic parameters are already known, the result can be easily converted into coordinates in the world coordinate system by coordinate transformation.

To show how to solve the equations for the coordinates of the object point, we first rewrite Eq. (3.27) to obtain the relationship between X^w and X^p . That is

$$X^p = R^p X^w + t^p \quad 3.31$$

Solving for X^w , we have

$$X^w = (R^p)^{-1} X^p - (R^p)^{-1} t^p \quad 3.32$$

Substituting Eq. (3.32) into Eq. (3.11) yields

$$Z_c x_n^c = R^c (R^p)^{-1} X^p - R^c (R^p)^{-1} t^p + t^c \quad 3.33$$

Let $C = R^c (R^p)^{-1}$ and $D = -R^c (R^p)^{-1} t^p + t^c$, where C is a 3×3 matrix and D is a 3×1 matrix. We have

$$Z_c \begin{bmatrix} x_n^c(1) \\ x_n^c(2) \\ 1 \end{bmatrix} = C \begin{bmatrix} X_p \\ Y_p \\ Y_p \end{bmatrix} + D \quad 3.34$$

Eq. (3.34) has 3 linear equations and 4 unknowns. Eliminate Z_c first and then reorganize the other 3 unknowns in the following format:

$$\begin{bmatrix} X_p \\ Y_p \end{bmatrix} = \begin{bmatrix} a' \\ a'' \end{bmatrix} Z_p + \begin{bmatrix} b' \\ b'' \end{bmatrix} \quad 3.35$$

where

$$a' = [(c_{33} x_n^c(2) - c_{23})(c_{32} x_n^c(1) - c_{12}) - (c_{32} x_n^c(2) - c_{22})(c_{33} x_n^c(1) - c_{13})] /$$

$$[(c_{32} x_n^c(2) - c_{22})(c_{31} x_n^c(1) - c_{11}) - (c_{32} x_n^c(1) - c_{12})(c_{31} x_n^c(2) - c_{21})] \quad 3.36$$

$$b' = [(d_1 - d_3 x_n^c(1))(c_{32} x_n^c(2) - c_{22}) - (d_2 - d_3 x_n^c(2))(c_{32} x_n^c(1) - c_{12})] /$$

$$[(c_{32}x_n^c(2) - c_{22})(c_{31}x_n^c(1) - c_{11}) - (c_{32}x_n^c(1) - c_{12})(c_{31}x_n^c(2) - c_{21})] \quad 3.37$$

$$a'' = [(c_{33}x_n^c(2) - c_{23})(c_{31}x_n^c(1) - c_{11}) - (c_{31}x_n^c(2) - c_{21})(c_{33}x_n^c(1) - c_{13})] /$$

$$[(c_{31}x_n^c(2) - c_{21})(c_{32}x_n^c(1) - c_{12}) - (c_{31}x_n^c(1) - c_{11})(c_{32}x_n^c(2) - c_{22})] \quad 3.38$$

and

$$b'' = [(d_1 - d_3x_n^c(1))(c_{31}x_n^c(2) - c_{21}) - (d_2 - d_3x_n^c(2))(c_{31}x_n^c(1) - c_{11})] /$$

$$[(c_{31}x_n^c(2) - c_{21})(c_{32}x_n^c(1) - c_{12}) - (c_{31}x_n^c(1) - c_{11})(c_{32}x_n^c(2) - c_{22})] \quad 3.39$$

Substitute Eq. (3.35) into Eq. (3.30) to form a cubic equation with only one unknown Z_p . Rearranging this cubic equation, we obtain a cubic equation of a common form, with one cubic, quadratic, and linear term each as well as a constant term:

$$OZ_p^3 + PZ_p^2 + QZ_p + T = 0 \quad 3.40$$

where

$$O = a' + (a')^3 kp(1) + a'(a'')^2 - e \quad 3.41$$

$$P = b' + 3(a')^2 b' kp(1) + 2a' a'' b'' + (a'')^2 b' \quad 3.42$$

$$Q = 3a'(b')^2 kp(1) + a'(b'')^2 + 2a'' b' b'' \quad 3.43$$

and

$$T = (b')^3 kp(1) + b'(b'')^2 \quad 3.44$$

This cubic equation can be solved by Cardano's method. Once Z_p is obtained, it can be substitute into Eq. (3.34) to solve for X_p and Y_p . The last step of this approach is to use Eq. (3.32) to convert the coordinates in the projector coordinate system $X^p = [X_p \ Y_p \ Z_p]$ back to the coordinates in the world coordinate system $X^w = [X_w \ Y_w \ Z_w]$.

Figure 3.6(e) shows the result of a flat board reconstructed using the cubic equation method. According to these comparisons, the reconstruction accuracy does not change significantly no matter which one of these three approaches is applied. The cubic equation method is our final choice for projector nonlinear calibration. Table 3.8 lists the RMS errors when the flat board is set in different orientations. From the linear calibration method to the nonlinear calibration method, the RMS error has been reduced significantly from more than 1.4 mm to less than 0.35 mm. Figure 3.7 shows several 3D scanning data of some other statues.

Table 3.8: RMS errors of the measured flat board in different orientations.

Position	linear	Camera nonlinear	Iteration nonlinear	Cubic nonlinear	8 images nonlinear
#1	1.2394	0.5853	0.3016	0.2988	
#2	0.6899	0.3088	0.2455	0.2448	
#3	1.4113	0.6010	0.3523	0.3502	
#4	0.6946	0.4597	0.2457	0.2435	
#5	1.1683	0.6106	0.3040	0.3013	
#6	0.8845	0.3636	0.2675	0.2665	
#7(8image)	0.9174	0.4313	0.2467	0.2455	0.2470

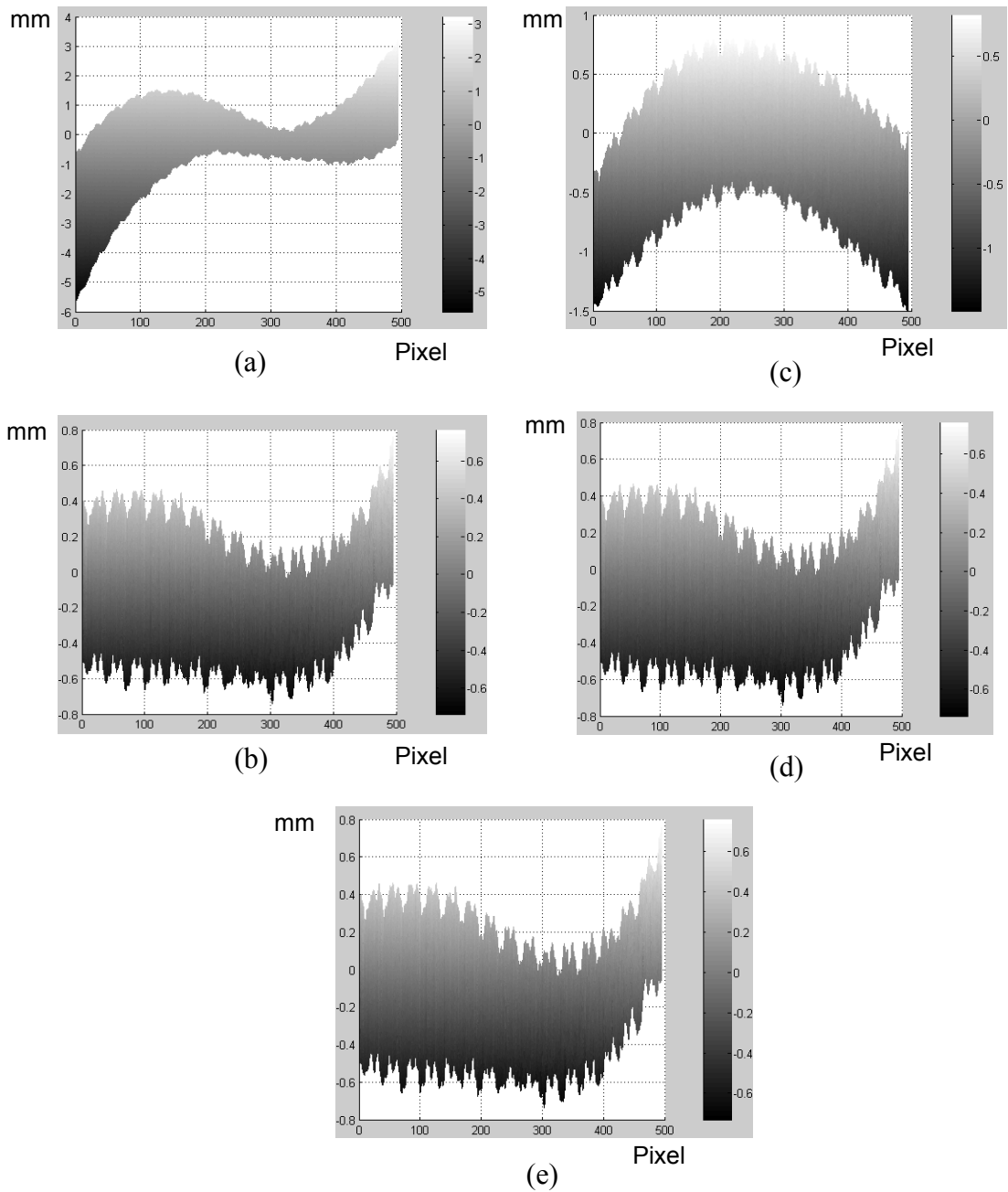


Figure 3.6: Error maps of a flat board measured with different calibration methods: (a) Linear calibration method. (b) Nonlinear calibration on camera only. (c) Nonlinear calibration on both camera and projector with the eight-image method. (d) Nonlinear calibration on both camera and projector with the iterative method. (e) Nonlinear calibration on both camera and projector with the cubic equation method.

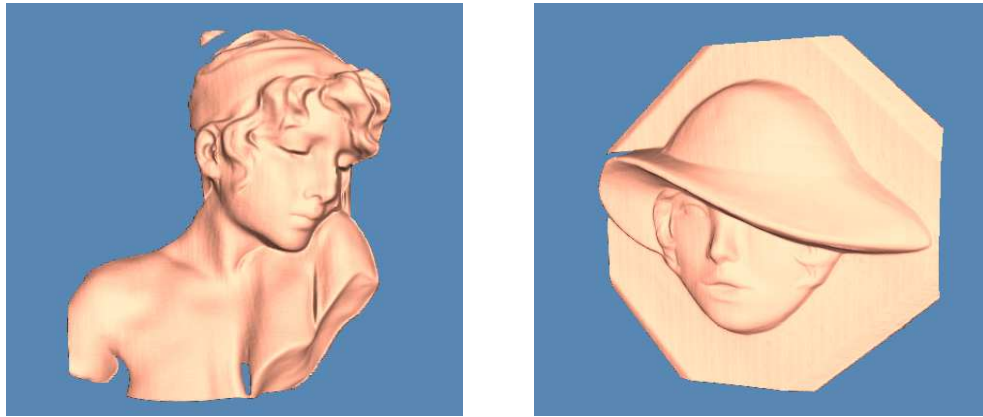


Figure 3.7: 3D reconstruction results obtained by using the nonlinear cubic equation method.

3.4 Summary

In this chapter, nonlinear calibration methods were introduced to correct lens distortion for both the camera and the projector. Results obtained from different calibration models were compared to show the improvement of the system accuracy. The peak-to-peak error caused by lens distortion was reduced significantly from more than 10 mm to less than 3 mm. The RMS error was also reduced from more than 1.4 mm to less than 0.35 mm, a reduction of more than 75 percent. Due to hardware limitation, lens distortion can not be corrected completely. However, the remaining error can be further reduced by error compensation. This research focuses on establishing the nonlinear calibration method. All the results shown in this dissertation are the results after nonlinear calibration with no other error compensations applied. The accuracy enhancement is entirely due to the introduction of the nonlinear calibration method.

Chapter 4 Real-Time System Based on the Nonlinear

Calibration Method

Real-time 3D shape measurement has a huge potential in security, entertainment, manufacturing, etc. due to its capability of scanning moving objects. Generally, there are two approaches for real-time measurement: one is to use a single pattern, a color pattern in most cases, and the other is to use quickly switching multiple patterns. In our research, the real-time system is based on the second approach. A color pattern based on the phase shifting technique is projected by a DLP projector. When the projector switches the red, green and blue color channels rapidly, multiple fringe images can be captured in a short period of time for real-time shape reconstruction.

In order to reach a high speed, the system previously used a fast reconstruction algorithm, which was not as accurate as even the linear algorithm introduced in Chapter 2. This research focuses on the implementation of the most accurate nonlinear algorithm in the real-time system to achieve high accuracy while maintaining the high speed capability.

4.1 Real-Time System with an Encoded Color Pattern

The flow chart of the multi-thread software for the real-time system is shown in Figure 4.1. The first thread grabs fringe images at a speed of 90 frames per second. The second thread retrieves the phase map from the grabbed fringe images. The third thread reconstructs the 3D coordinates and then displays it in on the screen.

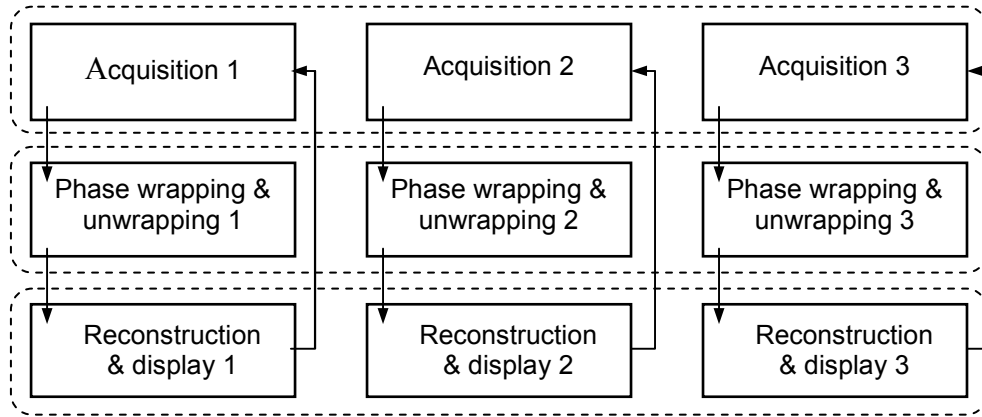


Figure 4.1: Flow chart of the multi-thread real-time 3D shape measurement system.

The centerline image is indispensable when the absolute phase map needs to be determined. However, the projected pattern cannot be switched between the fringe pattern and the centerline pattern fast enough because it takes time for the projector to generate a stable projection. To apply the nonlinear calibration method in real-time measurement, the first issue that needs to be addressed is how to eliminate the need for the centerline pattern while keeping the information it provides, so that no pattern switching is required.

The most straightforward idea is to embed the centerline in the fringe pattern directly. The highlighted centerline can be easily found, but the phase values at the pixels on the centerline cannot be determined because the intensity on these pixels does not change. To keep the phase shifting information, in the meanwhile, highlight the centerline pixels, a short encoded centerline marker is used.

Recall the definition of data modulation in Eq. (2.12), which is the ratio of the intensity modulation and the average intensity or the intensity bias. Data modulation is useful for evaluating the quality of the data that has been collected. A data modulation

near one is good and a data modulation near zero means a bad quality. In order to locate centerline pixels without losing their phase information, the data modulation value of the centerline pixels are intentionally reduced by an appropriate amount so that they can be identified by their relatively lower data modulation values and in the mean time, their phase values can still be retrieved with sufficiently high signal-to-noise ratio.

Rewrite Eqs. (2.6)- (2.8) in the following forms:

$$I_1(x, y) = [I'(x, y) + \delta I] + [I''(x, y) - \delta I] \cos[\phi(x, y) - \alpha] \quad 4.1$$

$$I_2(x, y) = [I'(x, y) + \delta I] + [I''(x, y) - \delta I] \cos[\phi(x, y)] \quad 4.2$$

and

$$I_3(x, y) = [I'(x, y) + \delta I] + [I''(x, y) - \delta I] \cos[\phi(x, y) + \alpha] \quad 4.3$$

where δI is a constant. In the new expression, the maximum intensity is still $I' + I''$, but the minimum intensity is increased by $2\delta I$ and the average intensity is increased by δI . Consequently, the data modulation value at these pixels becomes lower.

When data modulation is below some threshold, signal-to-noise ratio will suffer and as a result, the phase information may not be reliably retrieved. To avoid this problem, the data modulation at the pixels on the marker needs to be maintained at a reasonable level to ensure that these pixels can be distinguished from other pixels and still allow for reliable phase retrieval. Figure 4.2 shows the encoded patterns being used. Figure 4.2 (a) is the original ideal color pattern, which has a modulation near one. Figure 4.2 (b) is the modified pattern based on Eqs. (4.1)-(4.3). Figure 4.2 (c) shows the short marker with 1×20 pixels. Figure 4.2 (d) shows a long marker with a width of 5 pixels and a length the same as that of the fringe pattern. These markers can obviously be noticed in the fringe images as shown in Figure 4.3.

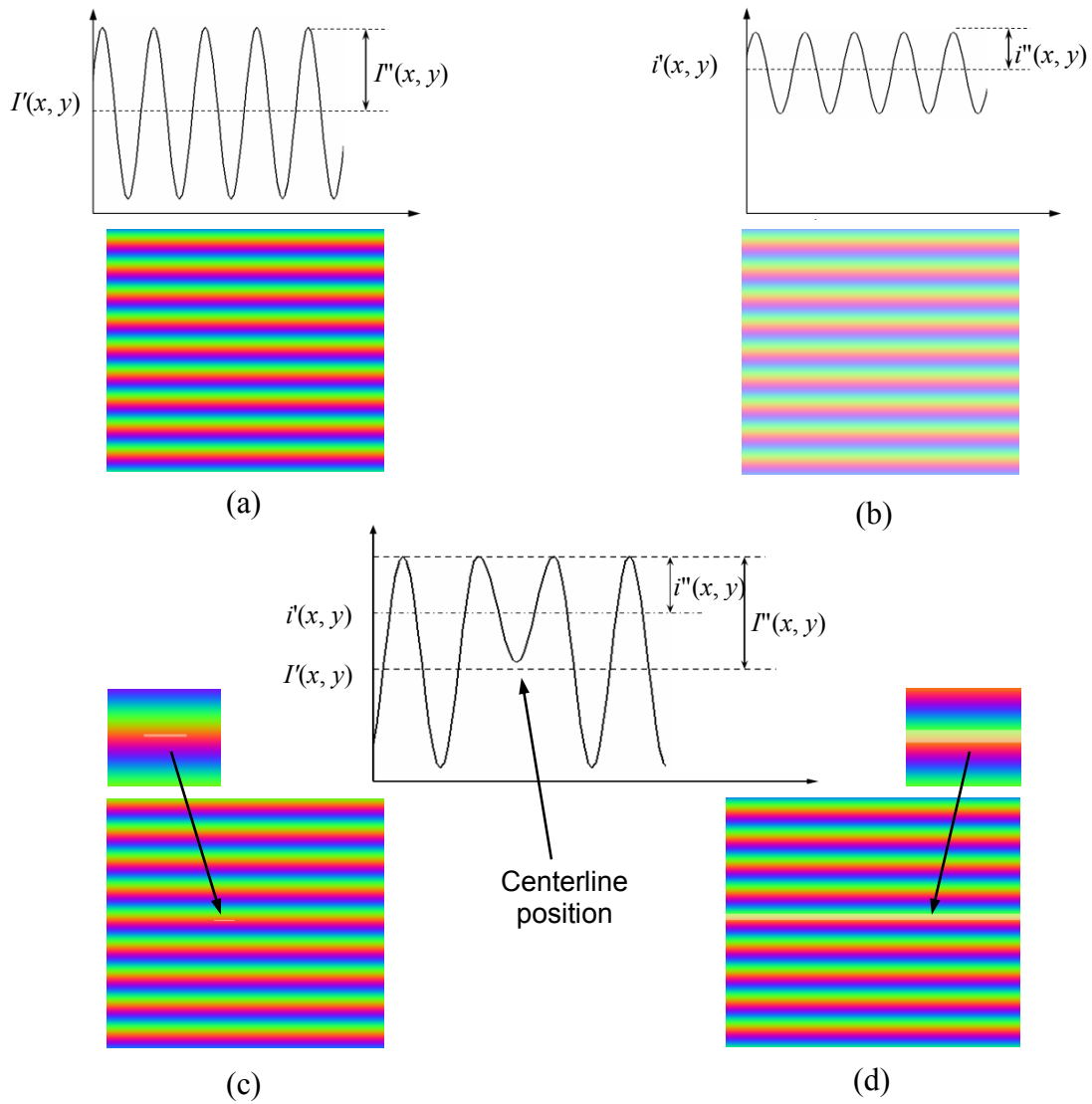


Figure 4.2: (a) Ideal fringe pattern. (b) Modified fringe pattern with higher intensity. (c) Fringe patterns with a short centerline marker. (d) Fringe patterns with a wide centerline marker.

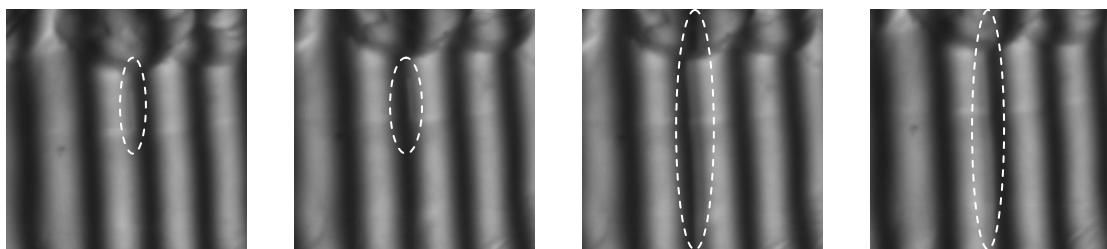


Figure 4.3: Markers in the fringe images.

To search for the location of the marker, data modulation at each pixel needs to be calculated. Actually, according to the relationship between the camera and the projector obtained from system calibration, the marker, which is located at a fixed position of the projector DMD chip, can be mathematically projected onto the camera image plane. Eqs. (2.25) and (2.26) connect the camera and the projector with the world coordinate system. Using this relationship, the marker can be mapped to a line on the camera image plane (if the nonlinear model is used, the line would be a curve). This line is usually called an epipolar line. By searching along this line, we can avoid searching through the entire image, thus improving the speed as well as reliability.

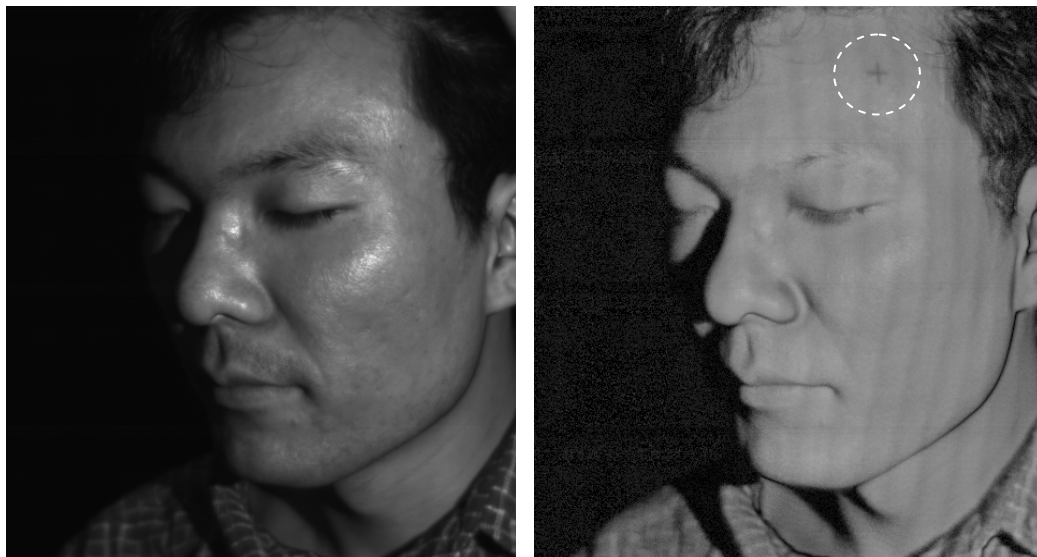
When implementing the searching procedure for the marker, we tried two different approaches. The first approach uses an interactive searching window. Since on a real object there may be areas with low surface reflectivity, shadow, and saturation, where data modulation can be as low as, if not lower than, that at the location of the marker, an interactive searching window avoids potential searching error and improves searching accuracy and reliability. Figure 4.4 shows this interactive searching procedure. In the default window, there may be some noise points. If these points are regarded as part of the marker, the location of the marker cannot be determined accurately, thus introducing error into the calculation of the absolute phase. The second figure shows the searching window after adjustment. The window is now smaller and the noise points are all eliminated. Searching the marker in such a small area also enhances the searching speed.



(a)

(b)

Figure 4.4: Interactive marker-searching window. (a) Default window. (b) Adjusted window.



(a)

(b)

Figure 4.5: Data modulation of the image with a crosshair marker. (a) 2D image. (b) Data modulation.

Another approach is to use a small crosshair marker. As shown in Figure 4.5, this crosshair can be clearly found in the data modulation map even on human models. Because a crosshair marker has a special shape, it can be easily detected by a specially designed filter. The search area is also narrowed down to a long strip along the aforementioned epipolar line. From Eqs. (3.2) and (3.5), we can obtain the normalized coordinate vector x_n^p of the crosshair center. Substituting it into Eq. (3.33), we have

$$\begin{bmatrix} X_c \\ Y_c \\ Z_c \end{bmatrix} = R^c (R^p)^{-1} \begin{bmatrix} x_n^p(1) \\ x_n^p(2) \\ 1 \end{bmatrix} Z_p - R^c (R^p)^{-1} t^p + t^c \quad 4.4$$

After we obtain the coordinates in the camera coordinate system, using Eqs. (3.1), (3.2), and (3.5), the pixel position $[u^c \quad v^c]$ of the center of the crosshair marker on the CCD image can be found as functions of Z_p . Figure 4.6 shows the marker searching procedure. The brighter strip is the searching area, the cross marker is always located in this area.

The texture map needs to be modified because the marker is visible in the texture map obtained by averaging the three fringe images. To remove the marker from the texture map, the summation of the average intensity and intensity modulation is used instead of the average of the three fringe images to generate the texture map. From the result in Figure 4.7, we can see that the marker is completely removed in the new texture map. Figure 4.8 presents some selected 3D models of a sequence of human face scanning data to show the system's capability of measuring moving objects. Smooth facial expression change is captured continuously. These data are taken in a frame rate of 30 frames per second.

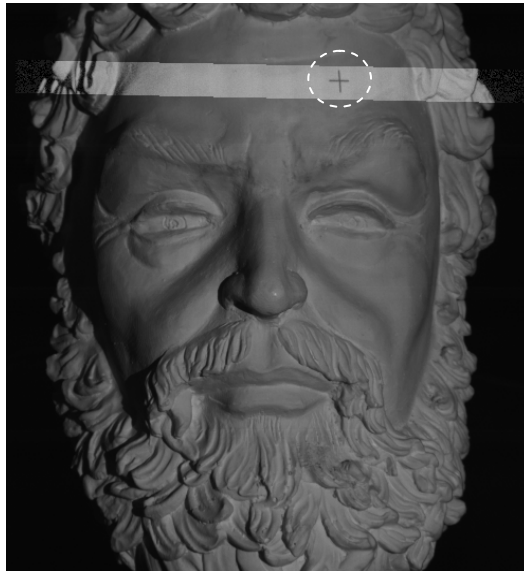


Figure 4.6: Automatic searching for the crosshair marker by using epipolar line.

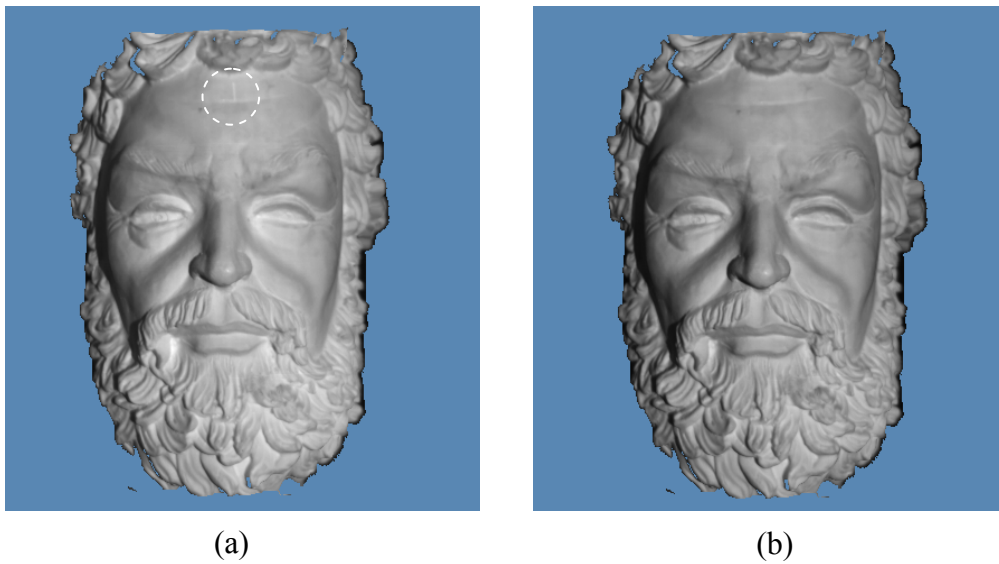


Figure 4.7: 3D data texture map. (a) Old texture map. (b) New texture map.

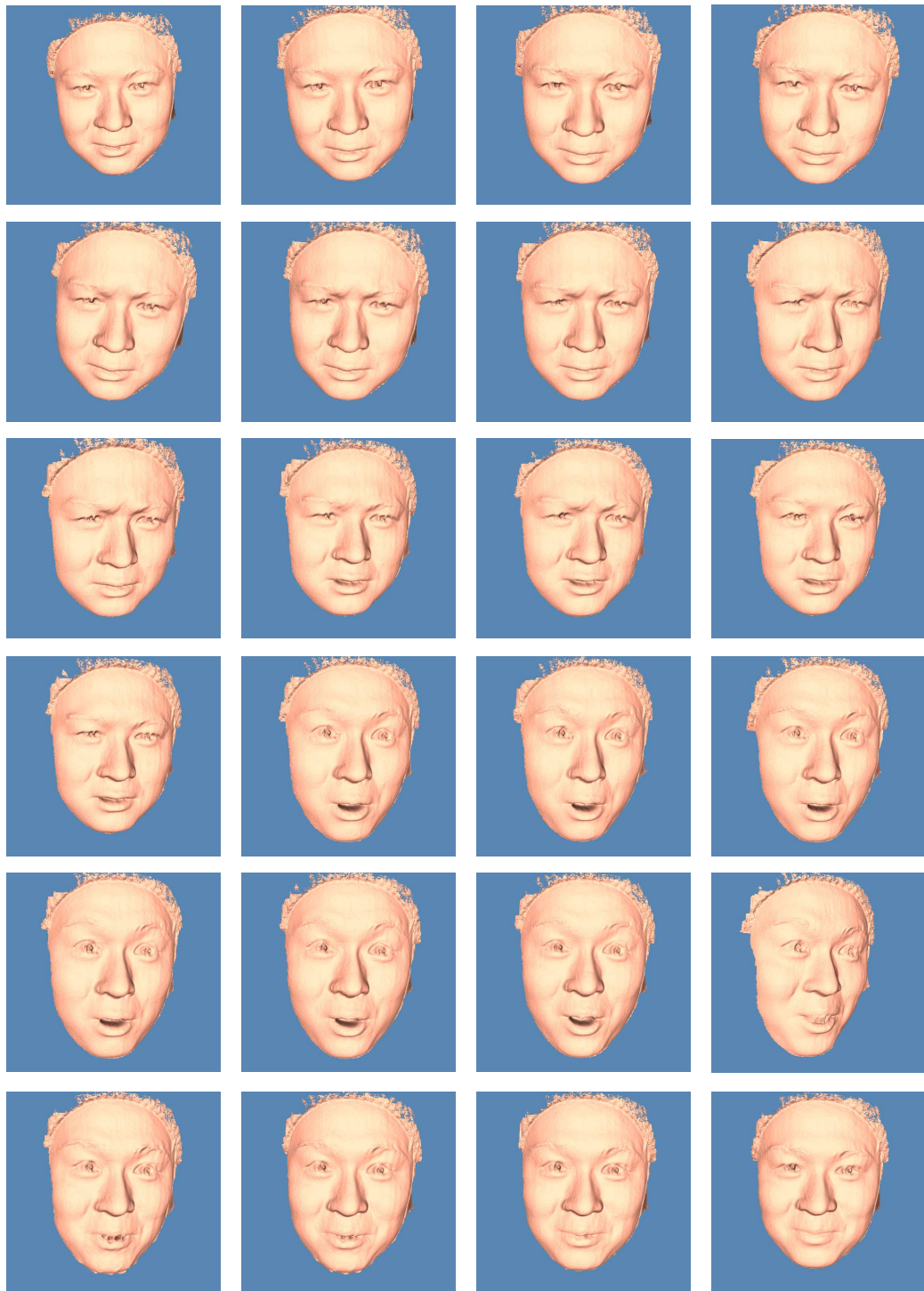


Figure 4.8: Selected 3D models of a real-time measurement sequence of human face expression.

4.2 60 Hz System

The highest potential scanning speed of this real-time system is 120 Hz, which is the refresh rate of the projector. The speed of our current system is limited at 30 Hz due to the speed of the camera used. In this section, we describe the design of the next generation system, which is simpler and has a higher scanning speed of 60Hz.

This new system uses a new camera with a VGA resolution of 640×480 pixels and a new frame grabber (Matrox Solios) for controlling the camera. This new camera has many advantages when compared to the old one. First it can sustain a 180 frames/sec image acquisition speed, which means the achievable 3D reconstruction speed can be up to 60 Hz. Figure 4.9 shows the timing chart of the 60 Hz system with this new camera. The system speed has been doubled as can be seen by comparing this timing chart with that of the 30 Hz system shown in Figure 2.7.

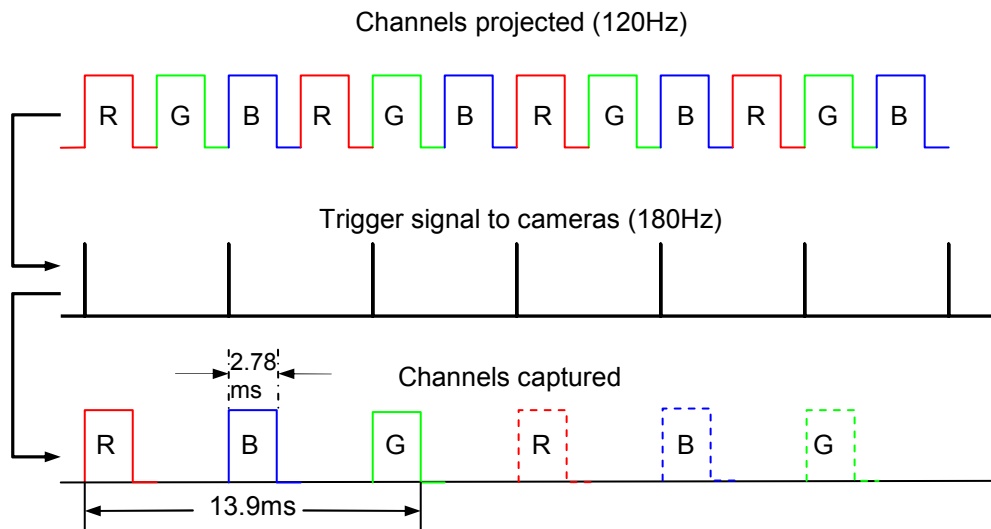


Figure 4.9: Timing chart of the 60 Hz System.

This camera also makes the connection interface with the computer much simpler. In Figure 4.10, the new camera and the old camera are shown together. It can be seen from the back side of the cameras that the new camera only has one cable, in addition to the power cable, while the old one has four. Further more, with this new camera, the trigger signal can be generated by software, thus eliminating the need for the microprocessor-based timing signal circuit. Finally, the power supply is also much simpler than the old one. These advantages allow us to build our next generation system into a faster, simpler, and more reliable system. Figure 4.11 shows human face models taken by this new system.

4.3 Summary

The real-time measurement accuracy was improved significantly by employing the new reconstruction algorithm based on the nonlinear calibration method. A marker embedded in the fringe pattern was used for absolute phase measurement. This design eliminated the need for the additional centerline image previously required, thus making it possible to achieve real-time speed at a higher accuracy. Even though the new algorithm is significantly more complex than the old one, we managed to achieved the same 30 frames per second scanning speed through optimization of the algorithm. A new generation 60 Hz system is also designed. With new high-speed camera and synchronization method, the real-time measurement speed is doubled and the system design becomes simpler, smaller and more reliable.

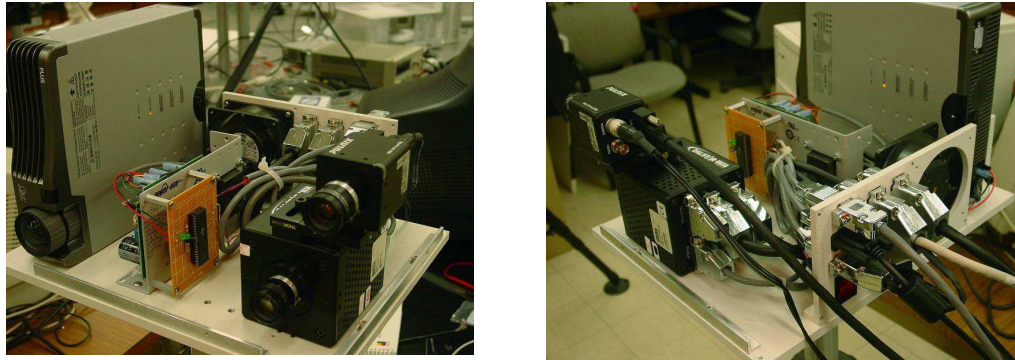


Figure 4.10: Front and back views of the high speed camera.

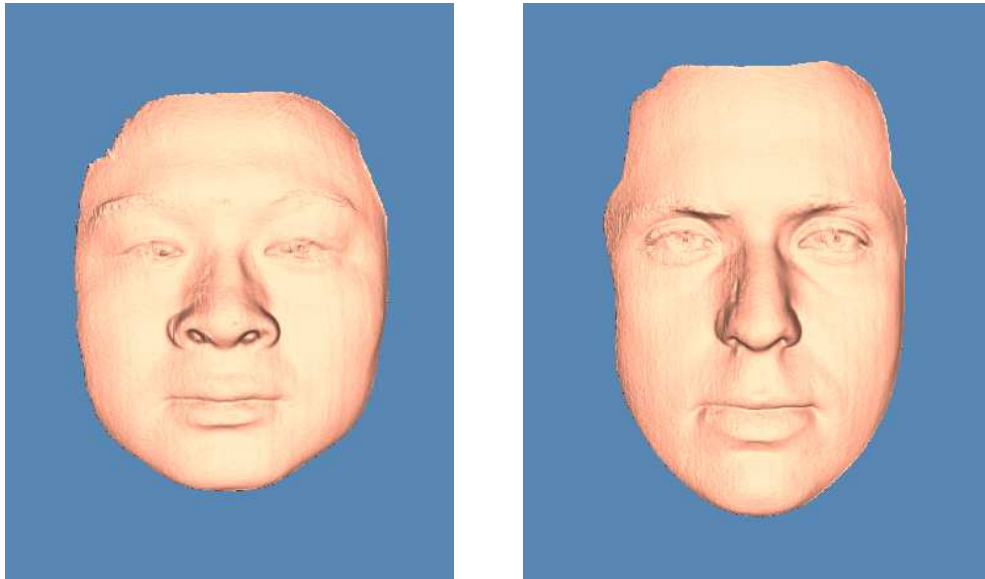


Figure 4.11: Human face models scanned by the 60 Hz system.

Chapter 5 Quality Map Guided Phase Unwrapping Algorithm

The previous phase unwrapping algorithm we used is a simple raster scan like algorithm. When the measured object has discontinuous features such as sharp edges, steps, etc., the problem of phase ambiguity will arise, which leads to discontinuous surface jumps on the reconstructed 3D model. In this chapter, a new phase unwrapping algorithm, namely quality map guided phase unwrapping algorithm, is developed to remove phase ambiguities for correct 3D reconstruction.

5.1 Phase Ambiguity

To create an object, which causes potential reconstruction errors due to phase ambiguity, we attach a two-inch high step to a flat board. This step has three sides perpendicular to the board and the fourth side in a slope. When a fringe pattern is projected onto this object as shown in Figure 5.1(a), phase discontinuity is created, which results in phase ambiguity. In this particular position, the upper side of the step can still be seen with fringe pattern, even though it has a sharp surface. In other words, the flat board and the step are connected on the upper side and the fringe pattern image is continuous. However, on the lower side, the fringe pattern is discontinuous, which causes phase ambiguity and further reconstruction error as shown in Figure 5.1(b). Somewhere along the lower edge, the phase changes are more than 2π , which makes the phase unwrapping algorithm unable to recover the phase correctly. The result is a severe jump in the 3D model reconstructed.

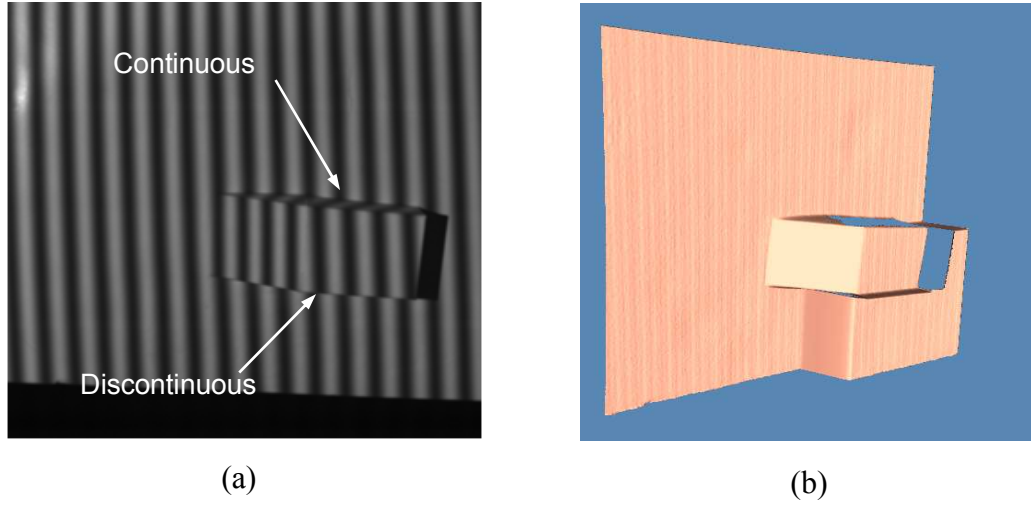


Figure 5.1: Phase ambiguity example. (a) 2D fringe image with phase discontinuity on the lower edge of the step which will cause phase ambiguity. (3) 3D model with phase jump cause by phase ambiguity.

5.2 Quality Map Guided Phase Unwrapping

Quality maps are arrays of values that describe the goodness of pixels in a phase map. Many features can be used as quality maps, such as the correlation map, phase derivative variance, maximum phase gradient, etc. In this research, the quality map used is the phase derivative, which is defined as follows:

$$Q_{i,j} = \sqrt{\Delta_{i,j}^u{}^2 + \Delta_{i,j}^v{}^2} \quad 5.1$$

where $\Delta_{i,j}^u$ and $\Delta_{i,j}^v$ are the phase differences along the u and v axes respectively in the CCD image. Figure 5.2 shows the quality map of the step and the board. From this map, we can see that the lower edge of the step is highlighted with a higher phase difference, which represents a relatively lower quality.

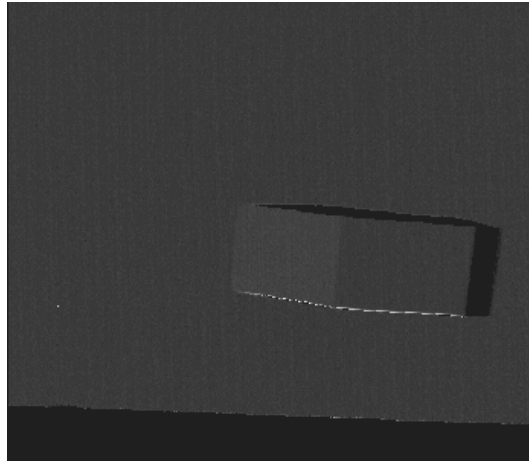


Figure 5.2: Quality map of the board with a step.

After the quality map has been generated, all the pixels can be sorted into groups according to their quality values during the phase unwrapping procedure. The phase unwrapping can be done starting from pixels with the highest quality and ending with pixels with the lowest quality. The flood-fill algorithm will sort and unwrap the phase values at the same time.

Figure 5.3 illustrates the quality map guided flood-fill algorithm. At the beginning, all the pixel groups are empty. A starting pixel is selected and the phase value of this pixel is regarded as the first unwrapped phase value. This starting pixel is then stored in one of the pixel groups according to its quality value. After this, the algorithm processes the remaining pixels in an iterative way, each time taking a pixel out from the pixel group with the highest quality value, unwrapping its four neighboring pixels if they have not been unwrapped yet and putting each of them into one of the pixel groups according to their quality values. When the algorithm selects an unwrapped pixel, it

always starts from the nonempty pixel group with the highest quality value. If there is no pixel in this group, it moves to the pixel group with the second highest quality value, and so on. Eventually the pixel groups will become all empty again, which means all the pixels have already been unwrapped.

By use of this algorithm, the low quality pixels, for example, pixels along the lower edge of the step, as shown in Figure 5.2, are blocked from being processed until all the other pixels are processed. As a result, low quality pixels would not affect high quality pixels and the phase ambiguity problem is solved effectively. Figure 5.4 is the 3D model of the step and the board reconstructed by using the new algorithm. Figure 5.5 shows another experimental result of a human face model. It is obvious from these results that the new phase unwrapping algorithm is highly effective in solving the phase ambiguity problem, thus making 3D reconstruction more accurate.

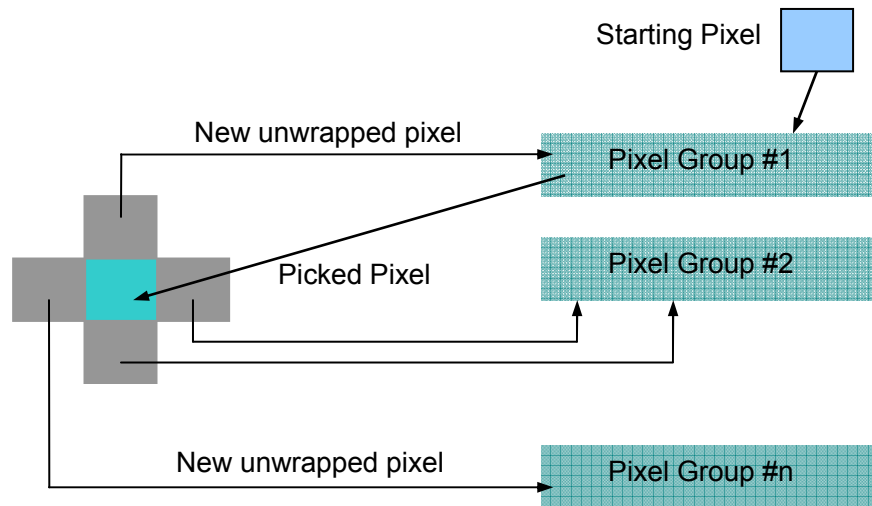


Figure 5.3: Quality map guided flood-fill phase unwrapping algorithm.

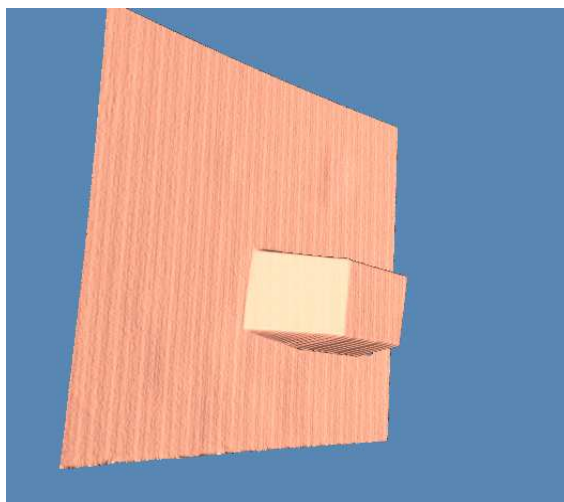


Figure 5.4: 3D model of the step on a board reconstructed by the quality map guided flood-fill algorithm.

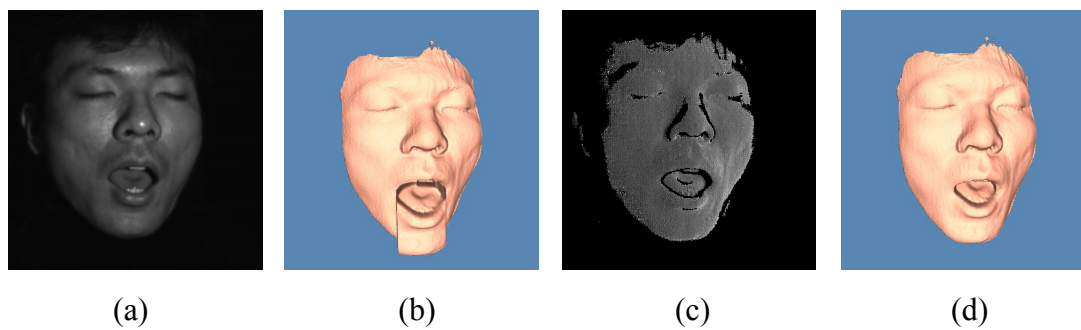


Figure 5.5: 3D model of a human face. (a) 2D image. (b) 3D model reconstructed by the old algorithm. (c) The quality map. (d) 3D model reconstructed by the quality map guided flood-fill algorithm.

5.3 Summary

In this chapter, a new quality map guided flood-fill phase unwrapping algorithm was introduced to eliminate the phase ambiguities caused by phase discontinuities larger than 2π . The reconstruction results obtained by using this new algorithm are shown in two examples. By employing this new algorithm, the problem of erroneous phase jumps is successfully solved in most cases.

Chapter 6 The Combined Phase Shifting and Stereovision

Method

A typical structured light system based on the phase shifting method consists of one camera and one projector. As an active method, the phase shifting method does not require any markers on the object surface. This makes it possible to accurately measure objects without much of textural features, which is usually difficult with the traditional stereovision method.

However, there are a few issues with the phase shifting method that need to be addressed before accurate measurement can be made. One is the sensitivity of its measurement accuracy to the nonlinearity of the projector's gamma curve. Many compensation methods have been developed to solve this problem. Zhang and Huang proposed a method that uses a look-up table (LUT) to intentionally distort the sinusoidal pattern generated in the computer so that the pattern will become sinusoidal once projected by the projector [91]. Zhang and Yau also proposed a method to use a LUT to compensate for the phase error directly [92]. However, in order to build the look-up table, either the projector's gamma curve or the phase error due to the nonlinear gamma curve needs to be calibrated carefully with a time-consuming procedure.

Another issue with the phase shifting method is that the projector needs to be calibrated to determine its intrinsic and extrinsic parameters before measurement, which is typically more complicated than the calibration of a camera. Even though a systematic

calibration method for projector has been developed by Zhang and Huang [83], projector calibration is still not as simple and accurate as camera calibration.

In this Chapter, a new approach to 3D shape measurement is proposed, which combines the phase shifting and the stereovision methods [93], [94]. The aim is to reduce the errors caused by inaccurate phase measurement, for example, the periodic errors due to the nonlinearity of the projector's gamma curve, and also to eliminate the need for projector calibration.

6.1 Phase Errors of the Phase Shifting Method

In a typical phase shifting system, the correspondences between the camera and the projector are found by matching the phase values calculated from the fringe images taken by the camera and the phase values of the ideal fringe pattern generated by the computer before projected by the projector. However, due to various reasons, such as the nonlinear gamma curve of the projector, the fringe patterns projected by the projector and the fringe patterns captured by the camera are not ideally sinusoidal anymore. Commercial projectors are all intentionally designed to have a nonlinear gamma curve for visually pleasing results. Using a projector with a nonlinear gamma curve, the ideal sinusoidal pattern generated in the computer will be distorted when projected onto the object. As a result, errors will be introduced to the phase map, which in turn causes errors in the reconstructed 3D model.

Figure 6.1 (a) shows an example of a reconstructed 3D model, which has periodic vertical noises caused by the nonlinear gamma curve of the projector. Phase measurement errors are also occurred when the object surface has various colors especially for surfaces with large color contrast. As shown at the lower right corner of Figure 6.1 (b), the test

object is a cardboard box with blue background and white letters. On the reconstructed 3D model, we can clearly see the errors around the edges of the letters.

It should be noted that all the results obtained from typical phase shifting method in this chapter are measured and reconstructed without using any error compensation method.

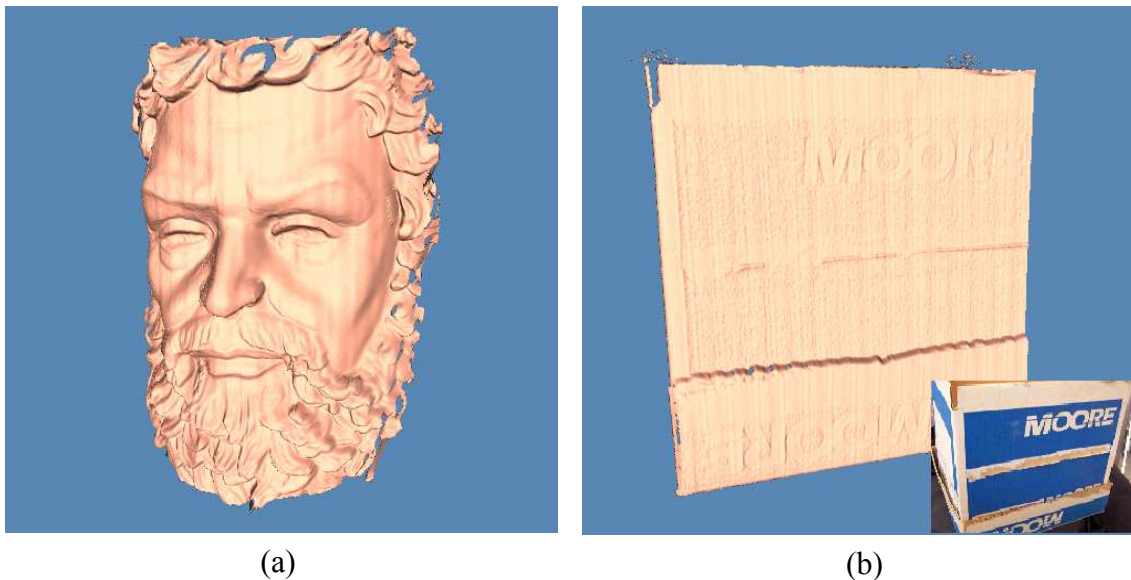


Figure 6.1: Examples of phase errors. (a) Error caused by nonlinear projector gamma. (b) Error caused by color contrast.

6.2 Combined Phase Shifting and Stereovision Method

A new method, which combines the phase shifting and stereovision techniques, is proposed for more accurate 3D shape measurement. This method uses two cameras and one projector and can eliminate errors caused by inaccurate phase calculation such as the periodic phase errors due to the nonlinearity of the projector's gamma curve.

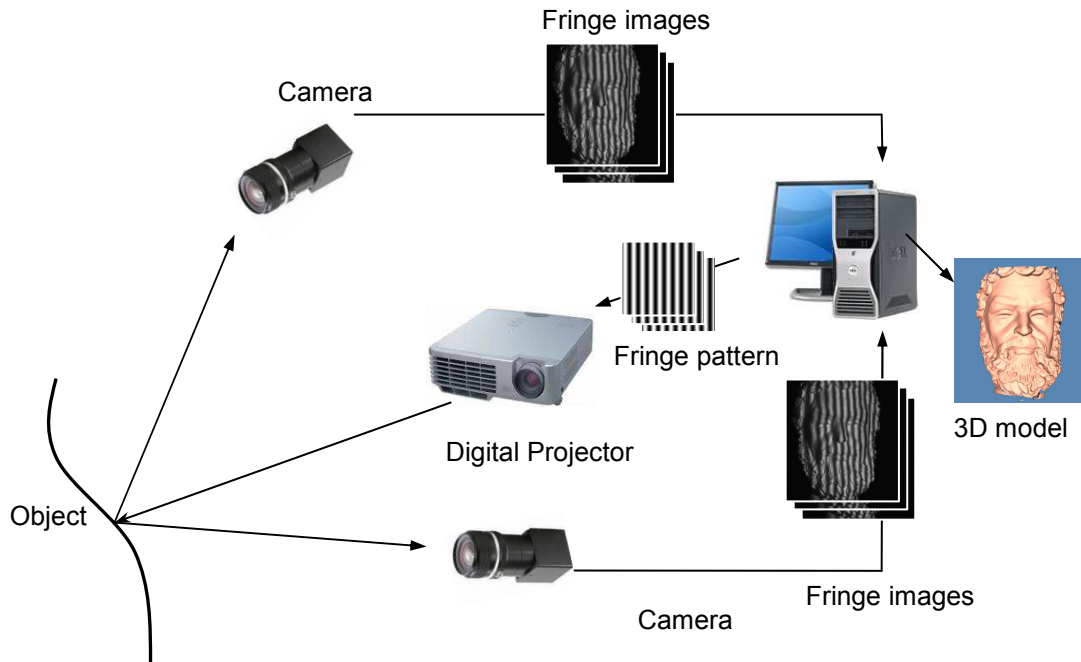


Figure 6.2: Schematic diagram of the system layout.

6.2.1 Principles and system setup

The schematic diagram of the system layout is shown in Figure 6.2. The basic system set up includes two digital cameras, one projector, and one computer. Sinusoidal fringe patterns are generated by the computer and projected onto the object via a digital projector. For better resolution, the phase shifting method with the three-step algorithm is used, which has been introduced in Section 2.1.2. Three fringe patterns are projected horizontally and then vertically. Two centerlines, the horizontal and vertical centerlines, are also projected for absolute phase calculation. Fringe images are taken from two different directions simultaneously by the two cameras arranged as a stereovision pair.

Both cameras are pre-calibrated and their intrinsic and extrinsic parameters are known. The fringe images are then sent to the computer for processing via a frame grabber. Phase wrapping and unwrapping algorithms are applied to obtain the horizontal and vertical phase maps based on the three-step phase shifting algorithm.

These phase maps are then used to assist stereo matching at the pixel level. The coordinates of the object surface are calculated based on triangulation. Since the phase value at each pixel is only used as a reference to assist stereo matching, it does not have to be accurate. Thus the projector does not need to be calibrated, which simplifies the system calibration. Errors due to inaccurate phase values are significantly eliminated because the two cameras produce phase maps with the same phase errors and these errors are cancelled after the matching. Two absolute phase maps of a Zeus statue, one horizontal and one vertical, are shown in Figure 6.3.

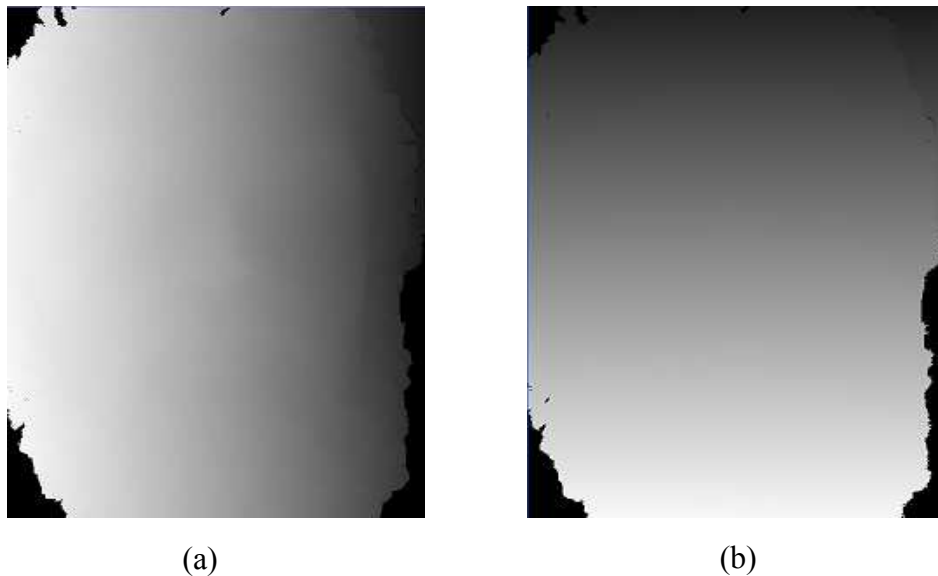


Figure 6.3: Absolute phase maps of Zeus statue. (a) Horizontal increasing absolute phase map. (b) Vertical increasing absolute phase map.

6.2.2 Pixel matching and 3D model reconstruction

In order to obtain accurate pixel matching and eliminate errors due to phase inaccuracy, we match pixels between two cameras in this proposed method instead of between one camera and one projector as in a typical phase shifting method. The projector no longer participates in 3D reconstruction.

As can be seen in Figure 6.3, the phase value is monotonically increasing leftwards in the horizontal phase map, and downwards in the vertical phase map. Since both absolute phase maps are monotonic, it is not hard to find the corresponding points between the two cameras without any ambiguities. For a certain pixel in one camera image, we can simply narrow down the searching field on the other cameras image from 2D area to 1D array by using the horizontal phase maps, and then use the vertical phase values to locate the corresponding pixel in that array.

In a typical stereovision system, assuming the cameras are pinhole cameras, the geometry relations between the two cameras at distinct positions lead to constraints between the image points. This geometry is so called epipolar geometry. A very useful epipolar constraint is shown in Figure 6.4. For an object point C , if the projection of C on camera1 is P_1 , and the projection of C on camera2 is P_2 , then P_2 must lie on a particular line, which is called an epipolar line.

Assume the intrinsic parameter matrices for the two cameras are A^1 and A^2 , and the extrinsic parameters, rotation matrices and translation vectors, are R^1, t^1 and R^2, t^2 respectively, then the linear camera models for camera1 and camera2 can be written as

$$s^1 \begin{bmatrix} u^1 & v^1 & 1 \end{bmatrix}^T = A^1 \begin{bmatrix} R^1 & t^1 \end{bmatrix} \begin{bmatrix} X & Y & Z & 1 \end{bmatrix}^T \quad 6.1$$

and

$$s^2 \begin{bmatrix} u^2 & v^2 & 1 \end{bmatrix}^T = A^2 \begin{bmatrix} R^2 & t^2 \end{bmatrix} \begin{bmatrix} X & Y & Z & 1 \end{bmatrix}^T \quad 6.2$$

where $\begin{bmatrix} X & Y & Z \end{bmatrix}$ is the coordinates for the object point, $\begin{bmatrix} u^1 & v^1 & 1 \end{bmatrix}$ is the projection coordinates of P_1 . Solve $\begin{bmatrix} X & Y & Z \end{bmatrix}$ from Eq. (6.1) and substitute into (6.2) we obtain the equation for epipolar line on camera2.

$$s^2 \begin{bmatrix} u^2 & v^2 & 1 \end{bmatrix}^T = A^2 R^2 R^{1-1} A^{1-1} s^1 \begin{bmatrix} u^1 & v^1 & 1 \end{bmatrix}^T - A^2 R^2 R^{1-1} t^1 + A^2 t^2 \quad 6.3$$

Where s^1 is the independent variable and $\begin{bmatrix} u^2 & v^2 & 1 \end{bmatrix}$ is a point on the epipolar line based on the value of s^1 . Using this linear equation (6.3), the searching area for a certain pixel can be constraint to the adjacent 3 to 5 rows. In this research, the camera resolution is 640×480 pixels. By calculating the epipolar lines, the searching area can be reduced by roughly a hundred times. For better accuracy, the nonlinear second-order symmetric radial distortion model, which has been introduced in Chapter 3, is used for cameras. And the reconstruction procedure is the same procedure as introduced in Chapter 3, except that this time we use the correspondence between two cameras, not one camera and one projector.

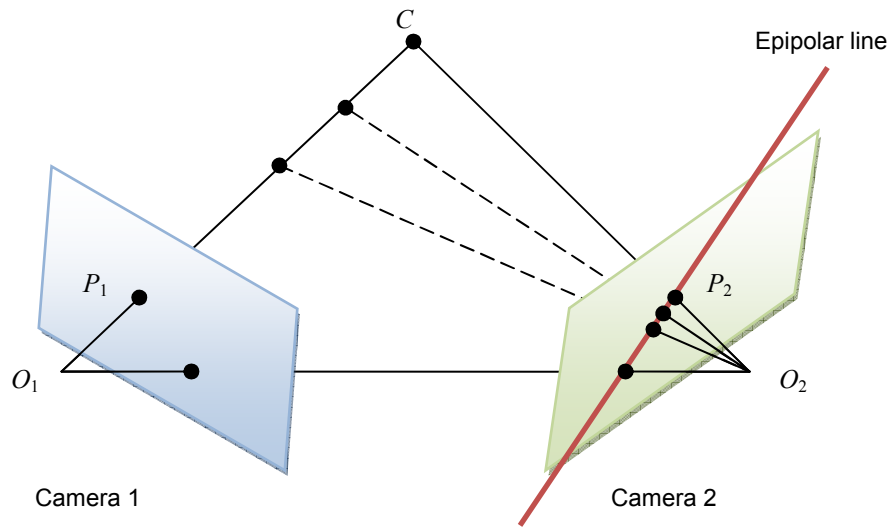
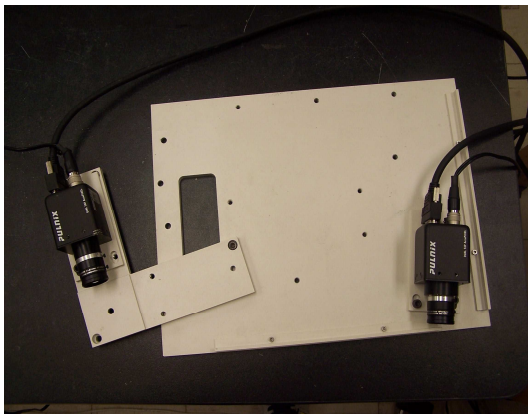


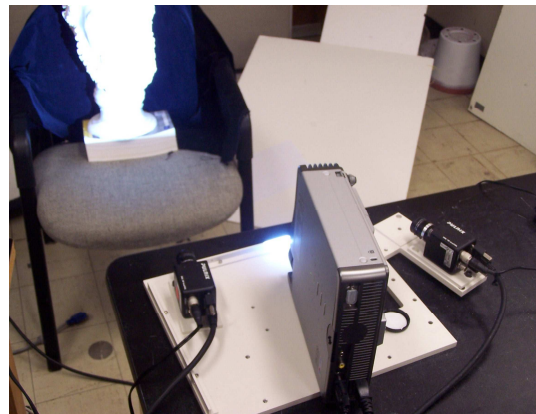
Figure 6.4: Epipolar constraint used in this method.

6.2.3 Experimental results

The experimental setup is composed of two black and white (B/W) cameras (Pulnix TM6740CL) with a resolution of 640×480 pixels and one B/W projector (Plus Vision PLUS-U5-632) with a resolution of 1024×768 pixels. The two cameras are separated by a certain angle and fixed on a metal frame. They are connected to the computer (Dell precision 690) via a frame grabber (Matrox SoliosXCL). This frame grabber has two camera link connectors and allows for simultaneous control of the two cameras. The cameras are pre-calibrated and their intrinsic and extrinsic parameters are obtained by using a Matlab camera calibration toolbox. The projector is separated from the cameras and is not fixed on the frame. During measurement, the projector is set at a position close to the cameras to make sure that the object is well illuminated by the projected light. And the projector is kept still during the measurement. Figure 6.5 shows two photographs of the actual system.



(a)



(b)

Figure 6.5: The setup of the combined phase shifting and stereovision system. (a) Cameras set up for stereovision. (b) Projector used to project pattern is separated from the cameras.

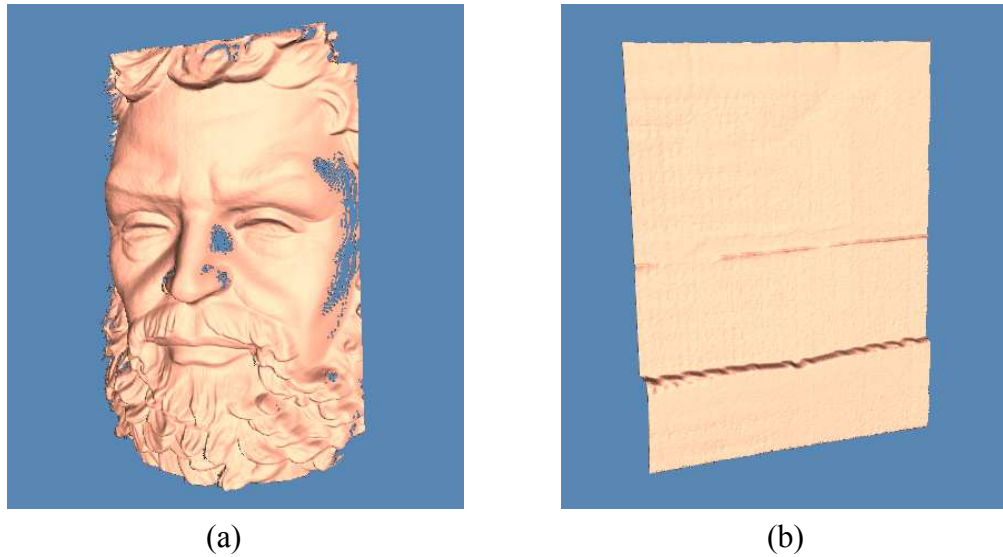
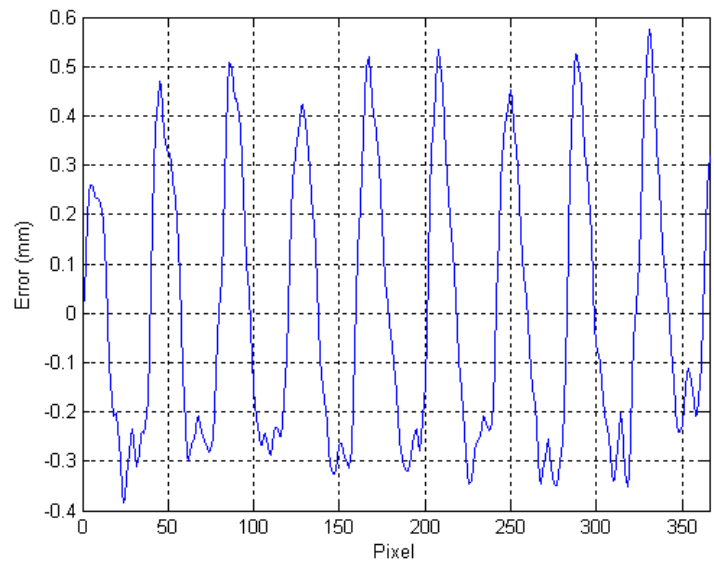


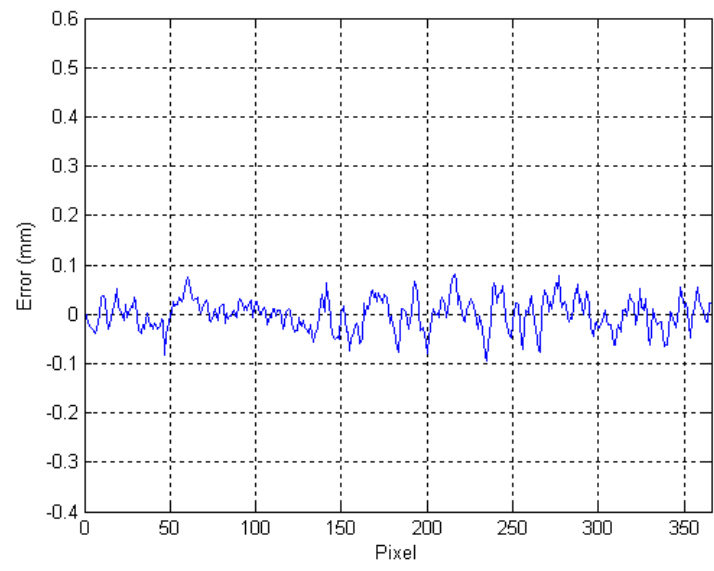
Figure 6.6: 3D models of (a) Zeus statue and (b) card box reconstructed by the combined phase shifting and stereovision method.

Figure 6.6 shows the results of the Zeus statue and the cardboard box measured by the new system. Comparing with results shown in Figure 6.1, the errors caused by projector nonlinearity and color variations are almost totally eliminated.

In order to give a more quantitative comparison, a flat board was measured by both methods. Figure 6.7 (a) shows the error cross section of reconstructed 3D model of the flat board measured by the phase shifting method and Figure 6.7 (b) shows the corresponding result measured by the combined phase shifting and stereovision method. Since the board surface is smoother than the measured results show, the variations shown in the plots can be considered as mostly from measurement errors. The calculation of the RMS values shows an error reduction of almost 9 times from 0.275 mm to 0.032 mm with the new method. The remaining error seems to be more like random error based.



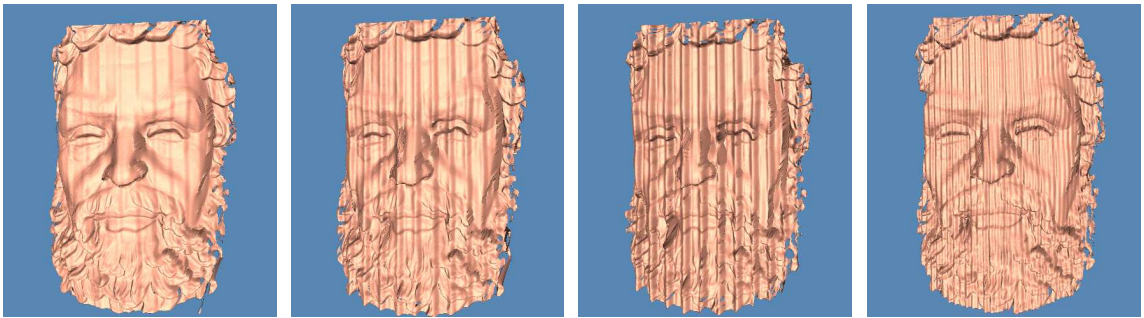
(a)



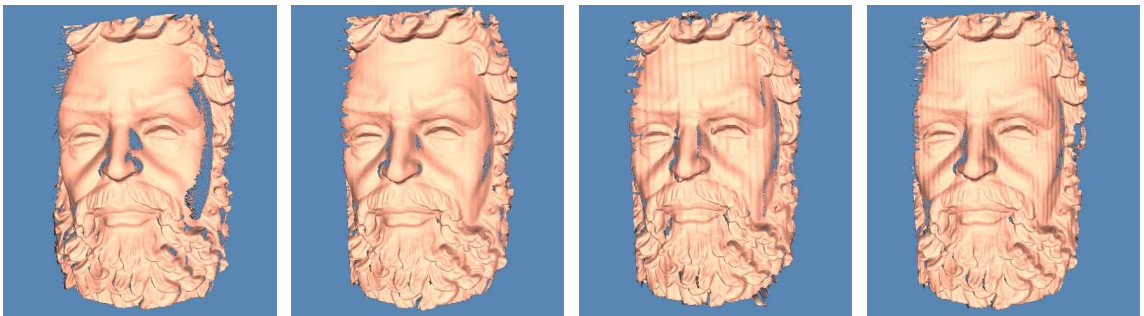
(b)

Figure 6.7: Error cross sections of a flat board 3D model. (a) Measured by phase shifting method. (b) Measured by the combined phase shifting and stereovision method.

To show the robustness of the new method, the fringe patterns were intentionally modified to make the intensities of the three channels imbalanced and the intensity profiles of the patterns non-sinusoidal, which is a simulation of a severe nonlinear gamma curve. Figure 6.8 (a) shows the results obtained by the phase shifting method and Figure 6.8 (b) shows the results obtained by the combined phase shifting and stereovision method under the same condition. From left to right, the first set of results were obtained by fringe patterns with imbalanced intensities of $0.8I_1$, I_2 and I_3 , the second with imbalanced intensities of $0.8I_1$, $0.6I_2$, and I_3 , the third with imbalanced intensities of $0.8I_1$, $0.6I_2$, and $0.4I_3$, and the fourth with randomly introduced nonlinearity.



(a)



(b)

Figure 6.8: Results comparison of modified patterns. (a) Results measured by traditional phase shifting method. (b) Results measured by the combined phase shifting and stereovision method.

In Figure 6.8, compare the first and the second columns, the errors are almost completely eliminated by use of the combined method. In the latter two columns, there are some periodic errors left, but they are much smaller in comparison. In normal situations the errors due to intensity imbalance and gamma curve nonlinearity will not be as significant. The above results nevertheless show the robustness of the new method in terms of measurement precision. Besides, the fact that the new method does not require careful calibration of the projector makes it much easier to implement the method for 3D shape measurement.

6.3 Use of a Visibility-Modulated Fringe Pattern

The combined phase shifting and stereovision method introduced in the last section can effectively eliminate errors caused by inaccurate phase calculation. The disadvantage of this combined method, however, is the doubling of the number of required images for 3D reconstruction, which slows down the image acquisition process and, as a result, makes it difficult to measure dynamically changing objects.

In this section, we propose to use a new visibility-modulated fringe pattern to address the aforementioned shortcoming of the combined method. The aim is to reduce the number of required fringe images to half, so that the combined method can still be applied to measuring dynamically changing objects.

6.3.1 Principles

The layout of the 3D measurement system introduced in this section is the same as shown in Figure 6.2, except that the fringe pattern used is a novel visibility-modulated fringe pattern.

As introduced in Chapter 2, the ratio of the intensity modulation and average intensity defines the fringe visibility or data modulation. Fringe visibility can be used to check the quality of data at each pixel. When its value is close to zero, the fringe has a low visibility, which indicates low data quality. In contrast, when its value is close to one, the fringe has a high visibility, which indicates high data quality. In this section, the fringe visibility is modulated to change periodically for the purpose of stereo matching.

The fringe pattern shown in Figure 6.9 (a) is the newly proposed visibility-modulated fringe pattern. Along the horizontal direction, this color pattern contains the three phase-shifted fringe patterns in its red, green, and blue channels. Along the vertical direction, the fringe visibility is modulated in a triangular shape. Figure 6.9 (b) shows the sinusoidal waveforms at two different vertical positions A-A and B-B as indicated in Figure 6.9 (a). The upper waveform shows a lower average intensity but a higher intensity modulation, which ensures a higher fringe visibility. In contrast, the lower waveform has a higher average intensity but a lower intensity modulation, which means a lower fringe visibility. Theoretically the phase and visibility of a fringe pattern are independent to each other. Therefore, we can calculate the phase value correctly regardless the value of the fringe visibility. In reality, however, lower fringe visibility in general means reduced signal-to-noise ratio. Therefore, the depth of visibility modulation for the fringe pattern needs to be carefully selected, so that it is large enough for stereo matching, in the mean time, not too large to cause significantly increased noise level. With this new pattern, we can obtain the phase information in one direction and fringe visibility information in the other direction simultaneously for stereo matching, so that the second group of fringe images is no longer required.

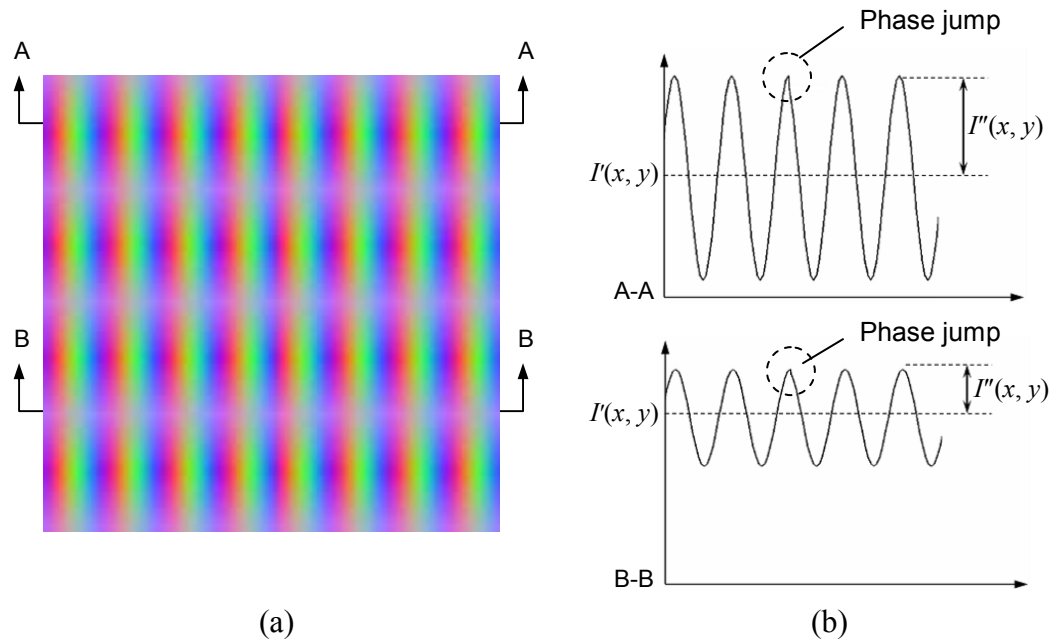
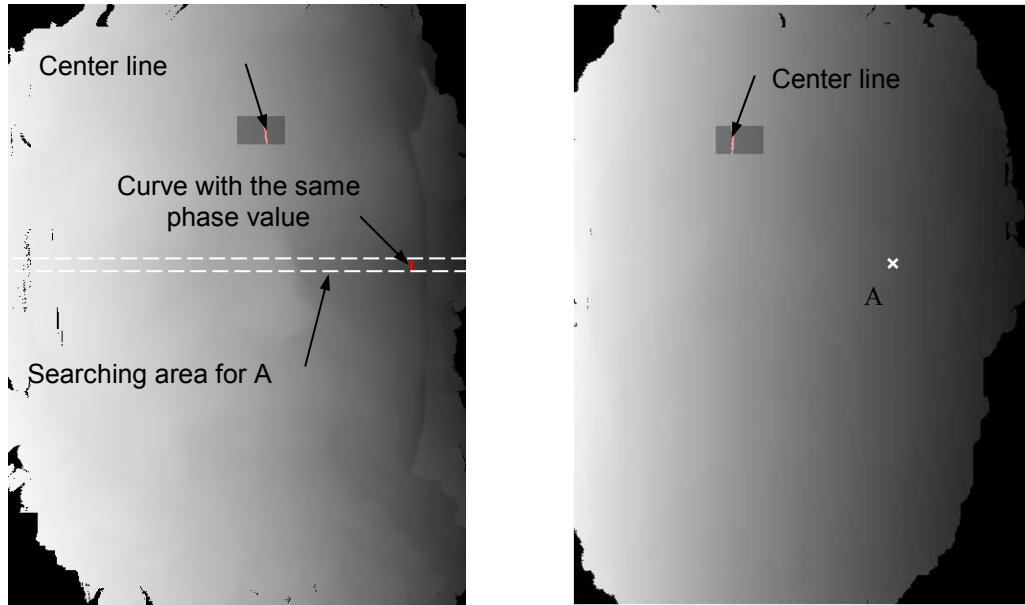
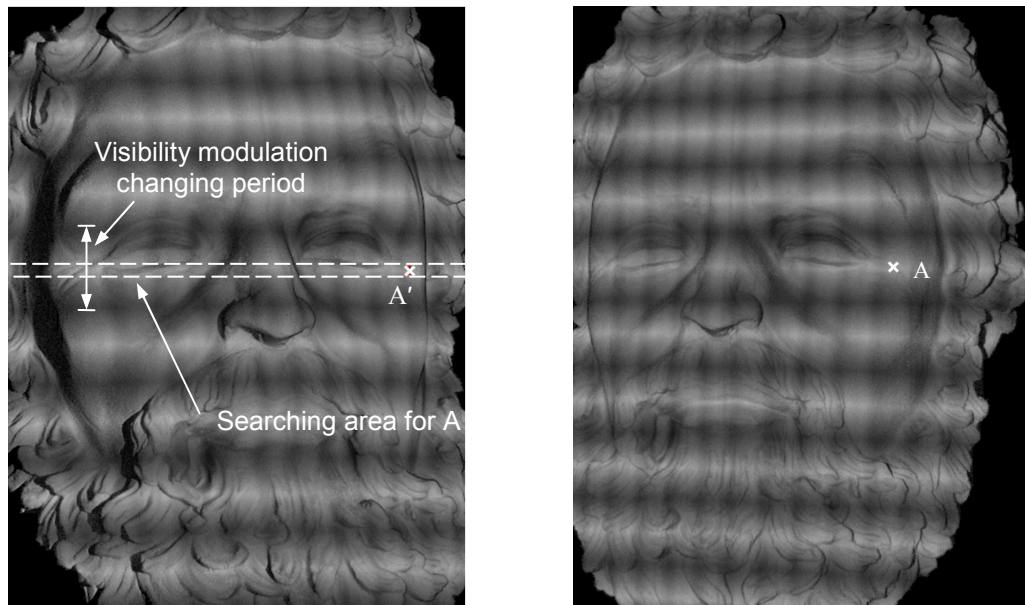


Figure 6.9: (a) Visibility-modulated fringe pattern. (b) Sinusoidal waveforms at two different vertical positions

With phase wrapping and unwrapping algorithms, a horizontally increasing phase map can be obtained from the fringe images. In order to use phase values for stereo matching at the pixel level, the phase maps need to be transformed into absolute phase maps. This means that there have to be some kind of common references in both phase maps. Previously, we used an extra centerline image to provide the reference, which slows down the image acquisition speed. In chapter 4 a crosshair marker with higher data modulation value is used for reference. However, in this new visibility-modulated fringe pattern, the data modulation is already used for other purpose, so the same approach in Chapter 4 is not applicable.



(a)



(b)

Figure 6.10: Stereo matching procedure. (a) Using the phase maps to find the same phase curve (b) Matching the visibility values to locate the right pixel.

In this research, the centerline is embedded in the fringe pattern as a 30-degree phase jump, as shown in Figure 6.9 (b). During the phase wrapping process, this phase jump is detected in a small window as shown in Figure 6.10 (a). By defining the phase values at the phase jump lines to be zero, a common reference in the phase maps from both cameras is established, which makes it possible to convert the phase maps into absolute phase maps. As a result, only three images are required for 3D model reconstruction, which makes possible the measurement of moving objects.

With the absolute phase maps available, for a certain phase value of a pixel A in the image of one camera we can find a curve with the same phase value on the image of the other camera. To avoid matching ambiguity and increase the matching speed, the epipolar geometry of the cameras is used to narrow down the searching area to a narrow strip, which is narrower than the period of the visibility modulation, as shown in the dotted-line-circled areas in Figure 6.10 (a) and 6.10 (b). Once the curve is found in the phase map, the visibility maps are applied to identify the corresponding pixel.

6.3.2 Experimental Results

The experimental setup is the same as introduced in section 6.2.3, except for the fringe pattern used. The reconstruction procedure has not been changed neither and the camera model used is still the second-order symmetric radial distortion model.

To demonstrate the performance of the proposed method in terms of error reduction, the Zeus statue and a cardboard box were measured by using the visibility-modulated fringe pattern. Figure 6.11 shows the results. Compare to Figure 6.1, most of the errors are eliminated by using this new pattern.

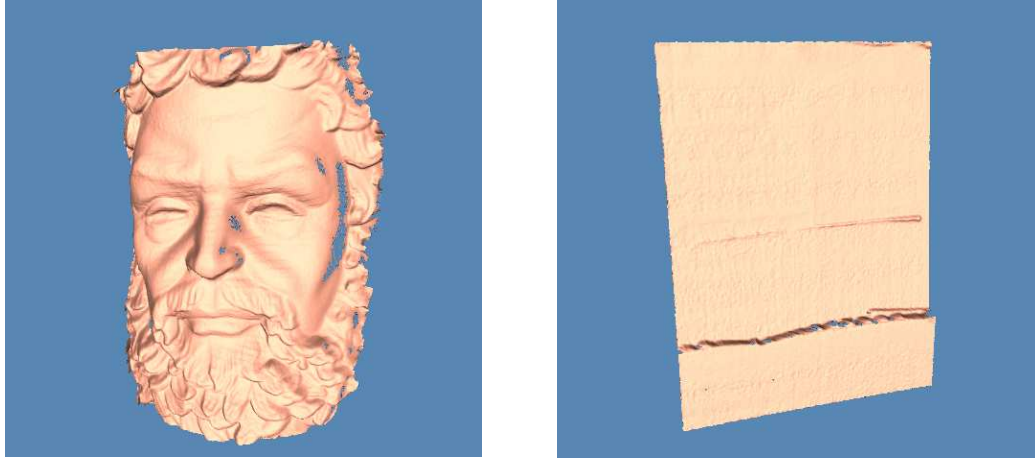


Figure 6.11: Results measured with visibility-modulated fringe pattern.

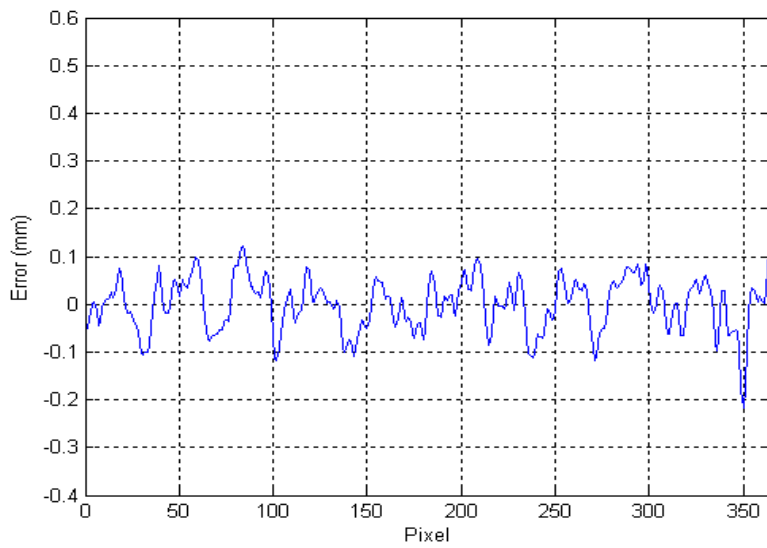


Figure 6.12: Cross sections of a flat board 3D model measured with the visibility-modulated fringe pattern.

The flat board is also measured with this new pattern and a cross section is shown in Figure 6.12. The RMS error is 0.056 mm. Comparing to Figure 6.7 (a), the error is reduced by 5 times which is not as good as Figure 6.7 (b) (which reduced the error by 9 times), however, the acquisition time for reconstructing a single 3D model is largely reduced to 13.9 ms as the timing chart shown in Figure 4.9.

To show the system's ability of measuring dynamically changing objects, we measured a data sequence of human face expression at a frame rate of 60 frames per second for 8 second, which resulted in a total of 480 reconstructed 3D models. Figure 6.13 shows 8 selected frames of all these 3D models, which clearly demonstrate the capability of the proposed method in capturing dynamically changing facial expressions.

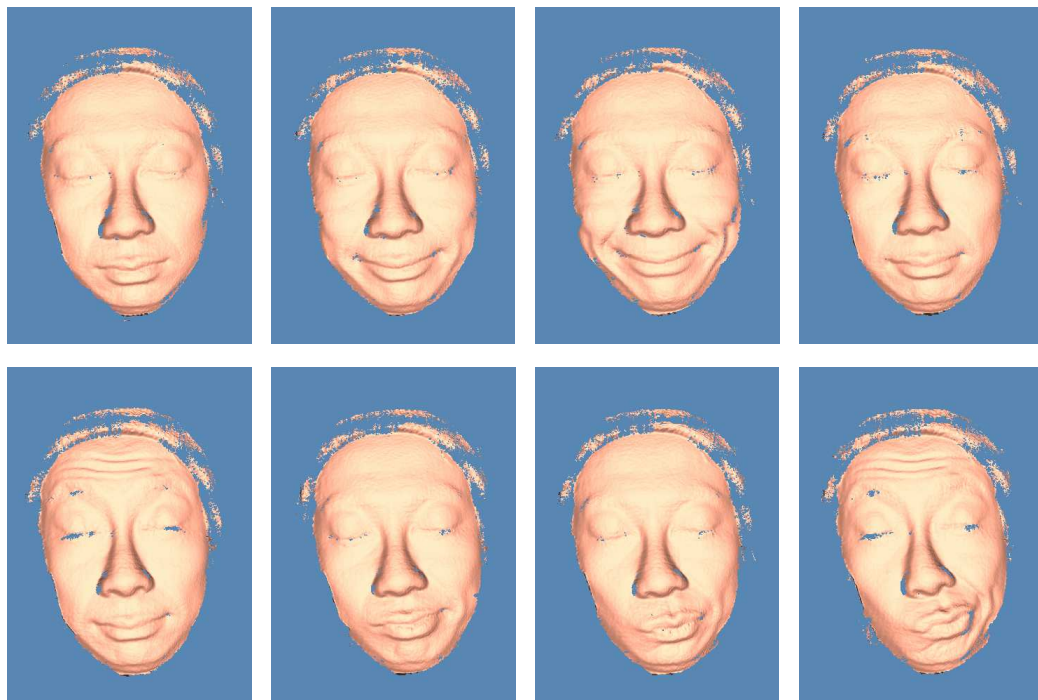


Figure 6.13: 8 selected 3D models of dynamically changing facial sequence captured by using the combined phase shifting and stereovision method with the visibility-modulated fringe pattern.

6.4 Summary

This Chapter has introduced a new method, namely the combined phase shifting and stereovision method, for more accurate 3D shape measurement. This method requires the use of two cameras and one projector. By using this method any errors due to inaccurate phase measurement could be significantly reduced. Experimental results showed that the typical periodic error due to projector nonlinearity was almost completely eliminated. The use of visibility-modulated fringe pattern has also been proposed. By using this new fringe pattern, the image acquisition time for three contiguous fringe images could be reduced to 13.9ms, thus made the measurement of moving objects possible.

Chapter 7 Color System Based on the Combined Phase

Shifting and Stereovision Technique

Real-time systems have been developed in previous researches as introduced in Chapter 4 and Chapter 6, which demonstrate the capability of measuring slowly moving objects, such as human facial expressions. However, when measuring rapidly moving objects, these B/W systems showed significant measurement errors due to their sequential nature of fringe image acquisition.

As introduced in Section 1.2.2, methods using color-encoded fringe patterns have been reported previously for use in measuring rapidly moving objects. In this chapter, we further the work on the color phase shifting method by adopting the combined phase shifting and stereovision method. In particular, we propose to use a color visibility-modulated fringe pattern and color devices to reap the accuracy advantage offered by the combined phase shifting and stereovision method, while keeping the speed advantage of a color phase shifting system [95].

7.1 Motion Error of B/W System

Since multiple images are required for the phase shifting method, the object is usually needed to be motionless. If the images can be captured fast enough, slowly moving objects can be measured. In the real-time system, three phase-shifted fringe patterns are encoded in the red, green, and blue channels to form a color fringe pattern.

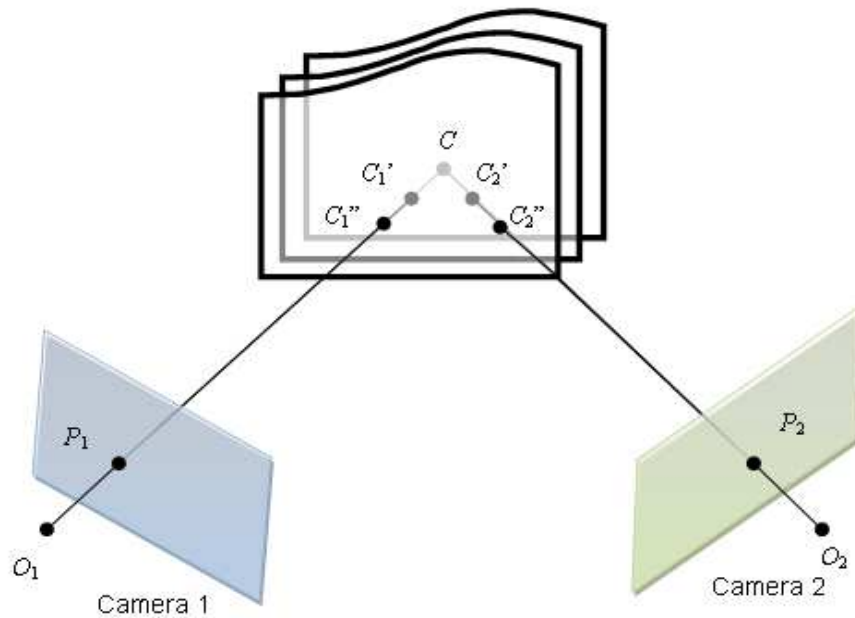


Figure 7.1: Schematic diagram of the error caused by object motion.

When this pattern is projected onto the object by a digital-light-processing (DLP) projector working in B/W mode, the three color channels are projected in grayscale sequentially and periodically. By synchronizing the camera and projector, the three fringe images can be captured in 13.9ms. At this speed, slowly moving objects, such as human face with expression changes, can be recorded as shown in previous chapters. However, for fast moving objects, errors due to object motions still appear on the reconstructed 3D models.

Figure 7.1 shows the schematic diagram of the causing of motion errors in the combined phase shifting and stereovision method proposed in Chapter 6. In order to

recover the phase map, three fringe images are needed for each camera. As illustrated, for the measurement of a certain point C , due to the object position changing, the actually points taken by camera1 are C , C_1' and C_1'' , and the corresponding points taken by camera2 are C , C_2' and C_2'' respectively. The traditional phase shifting system also has this problem, except that that kind of system only uses one camera.

7.2 Color Based Approach

7.2.1 Color-encoded fringe pattern

The problem caused by object motions can be solved by using a color liquid-crystal-display (LCD) projector and one or more color cameras. Different from DLP projectors, LCD projectors project the three color channels simultaneously. The three phase-shifted fringe patterns can be encoded in the red, green, and blue color channels to form a color fringe pattern and projected at the same time. Then only one color image needs to be taken by the color camera. The red, green, and blue components of this color image can be separated to generate the three fringe images for phase map calculation. Since only one image is captured by the camera, the image acquisition time is significantly reduced and therefore object motions will have much less effect on the measurement results.

7.2.2 Color imbalance and color coupling

The speed advantage of the color system comes with problems associated with the use of color, which need to be solved before accurate measurements can be made. One of

the major problems is color imbalance. Figure 7.2 shows the cross sectional intensities of three color fringe images. In this case, the single color fringe patterns were generated with the same intensity and projected onto a white board via an LCD color projector. The fringe images were captured by a color camera. As can be seen in this figure, the green fringe image has a much larger intensity over the red and blue fringe images. This intensity discrepancy is called color imbalance, which exists in both the camera and projector. The color imbalance problem can result in significant phase errors in the measurement results. Compensation methods have been developed in the past. For example, Pan and Huang proposed a method that used a look-up-table (LUT) to solve this problem [62].

Color coupling, which is caused by the spectrum overlapping of the color channels, is another issue that needs to be addressed. The color channels are usually intentionally designed to have spectrum overlaps in order to prevent color-blind regions. As a result, the red, green, and blue channels of a color fringe image cannot be separated completely. Color coupling is usually severe between green and red channels as well as green and blue channels. It is relatively weaker between the red and blue channels. Figure 7.3 shows the cross sections of a green fringe image. As can be seen in the figure, the red and blue components also have intensities that are not negligible. The color coupling problem can be solved by using either compensation algorithms or specially designed color filters to change the color spectra of the camera [61], [62].

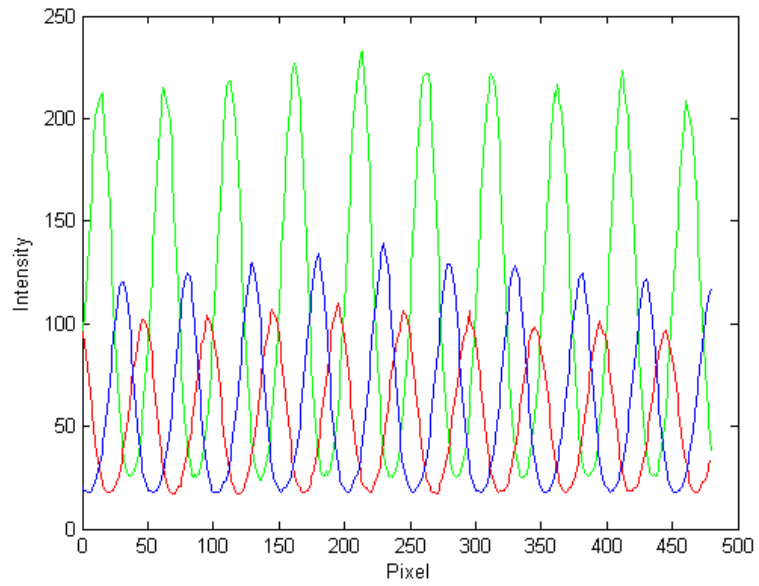


Figure 7.2: Color imbalance of the three color channels.

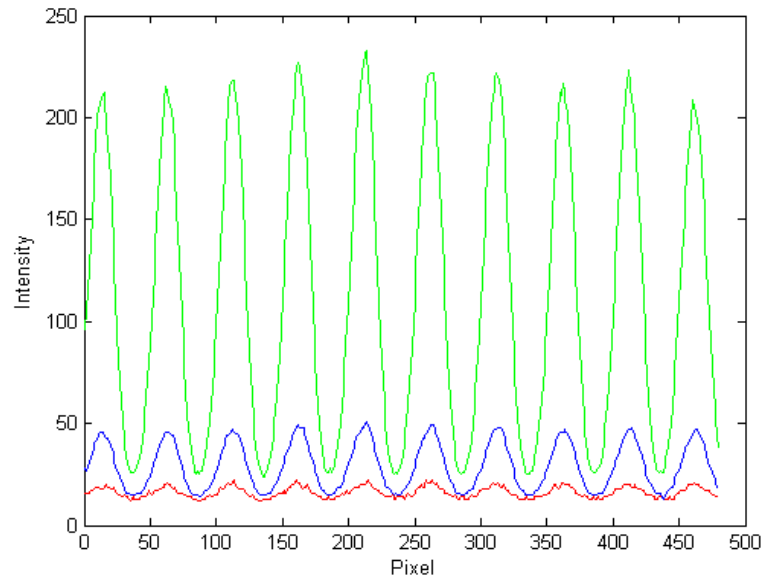


Figure 7.3: Color coupling appearance in a green fringe image.

7.2.3 Use of a color visibility-modulated fringe pattern

The color 3D shape measurement system is composed of a color LCD projector which is used to project the visibility-modulated fringe pattern and two color cameras which are used to capture the fringe images of the object. In this system, each camera only needs to take on color fringe image for 3D reconstruction. Then each color fringe image can be separated into three grayscale fringe images for calculation of the phase values. In this way, we can significantly reduce the image acquisition time and make the system more suitable for measuring objects in motion.

In general, the color imbalance and color coupling problems cause significant errors in the traditional phase shifting method. Fortunately, the same thing does not happen in the case of the combined phase shifting and stereovision method. We will show in the next section that errors caused by color imbalance and color coupling are significantly reduced in the same way as the errors caused by phase miscalculation due to the projector's nonlinearity in the B/W system.

7.3 Experiments

7.3.1 System setup

The color system has the same configuration as the B/W system shown in Figure 6.2, except that all the devices used are color devices and the projector works in color mode. The cameras are single-CCD Bayer cameras with a resolution of 640×480 pixels. The projector is an LCD projector with a resolution of 1024×768 pixels. The two cameras are pre-calibrated by using the Matlab camera calibration toolbox and are fixed

in position relative to each other. A frame grabber is used to synchronize and control the cameras. The projector is neither calibrated nor fixed relative to the cameras. It can be placed at any position as long as it can properly illuminate the object.

7.3.2 Compensation methods

Use of the combined phase shifting and stereovision method can significantly reduce the systematic phase errors. However, when the nonlinearity of the projector's gamma curve or the color imbalance is too large, there will be slight errors left on the reconstructed 3D model, as illustrated in Figure 6.8. To further reduce the phase errors and obtain optimal results, a basic compensation for the nonlinearity of the projector's gamma curve is adopted. An LUT was built to generate a calibrated fringe pattern. Since we only need a rough calibration, this procedure is needed to be done for only once and the result is recorded.

To solve the severe color imbalance problem, the intensities of three different channels are multiplied by three different coefficients. Also, when the pattern is generated, the green channel is assigned with a lower intensity than the other two channels. Even though the imbalance ratios are not quite the same over different grayscale levels, experiment shows that this simple adjustment is sufficient for the combined phase shifting and stereovision method to rectify the color imbalance issue.

As for the color coupling problem which is not as severe as color imbalance in our case, no compensation was done at all. From the measurement results, which will be shown in the next section, the color coupling issue will not affect the measurement performance, when the combined method is applied.

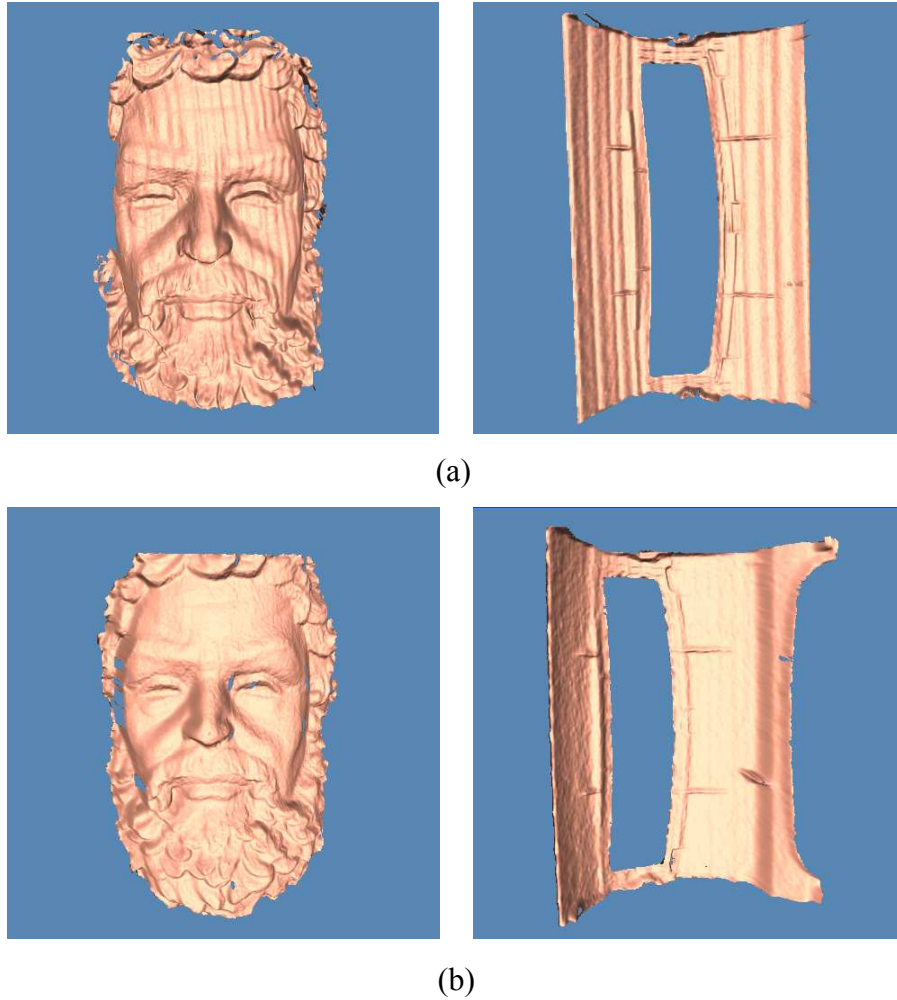


Figure 7.4: Measurement results of (a) the color phase shifting method, and (b) the proposed combined phase shifting and stereovision color system.

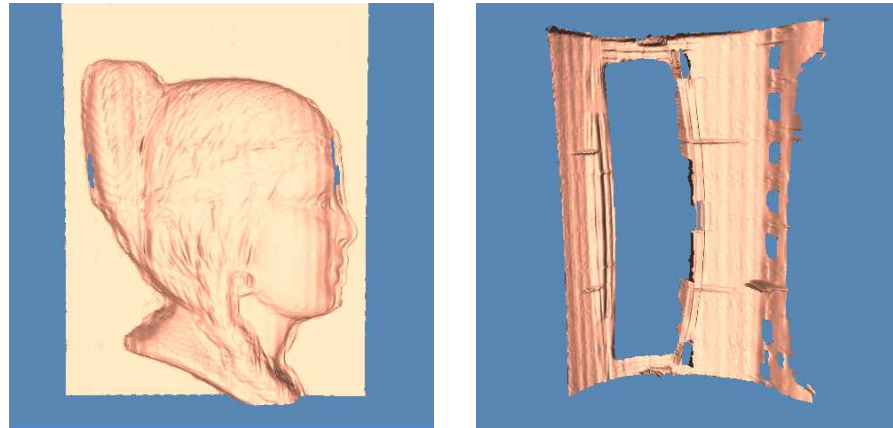
7.3.3 Experimental results

Figure 7.4 shows the advantage of the color combined phase shifting and stereovision method over the traditional color phase shifting method. The Zeus statue and a plastic part, which was painted in white, were measured to show the effectiveness of

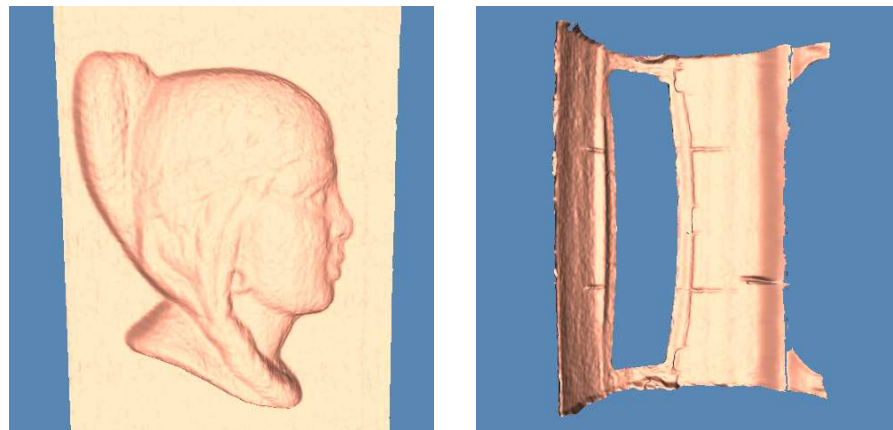
this color system. Figure 7.4 (a) shows the results measured by the traditional phase shifting system composed of one color projector and one color camera. Even though the same compensation methods were used, significant errors still appear on the reconstructed 3D models. Figure 7.4 (b) shows the results obtained by the combined phase shifting and stereovision system where no obvious systematic errors can be observed. The phase errors caused by the nonlinearity of the projector's gamma curve, color imbalance, and color coupling are mostly eliminated.

To show the system's capability of measuring objects in motion, a plaster statue of a girl's profile and the white painted plastic part were measured by the B/W system and the color system both based on the combined phase shifting and stereovision method, while being quickly moved in front of the systems.

As shown in Figure 7.5 (b), the measurement results obtained by the color system are not obviously influenced by the motion, while the results obtained by the B/W system shown in Figure 7.5 (a) have large distortions. The exposure time of the color cameras was set at approximately 5ms in this case, but it could be adjusted depending on the brightness of the illumination and sensitivity of the cameras. It is possible to adjust the exposure time freely because that the cameras no longer need to be synchronized with the projector. Compared to the total acquisition time of 13.9 ms required by B/W system, the color system is more than twice as fast. Besides, this speed advantage will be even more significant if the exposure time is further reduced with higher brightness of the projector or higher sensitivity of the cameras.



(a)



(b)

Figure 7.5: Measurement results of objects in motion by combined phase shifting and stereovision systems. (a) Results obtained by B/W system. (b) Results obtained by color system.

7.3.4 Discussion

The results obtained by the color system showed a lower resolution than those from the B/W system. This was because the color cameras used in this research are single-CCD Bayer cameras, which has 50% pixels for green and 25% each for red and

blue channels. When a color image from such a camera is separated into three grayscale images, the missing pixels are filled by interpolation. Figure 7.6 (a) is the red channel of a color fringe image taken by a Bayer camera. The noise level is obviously higher than the image taken by a 3-CCD camera, which is much clearer and smoother as shown Figure 7.6 (b). Using 3-CCD cameras, the measurement results are expected to be significantly improved. However, a 3-CCD camera is typically much more expensive than a single-CCD camera.

The color system is also sensitive to ambient light and object surface textures. During the measurement, all the indoor lights need to be turned off for accurate results. In addition, the objects measured so far all have white and diffuse surfaces.

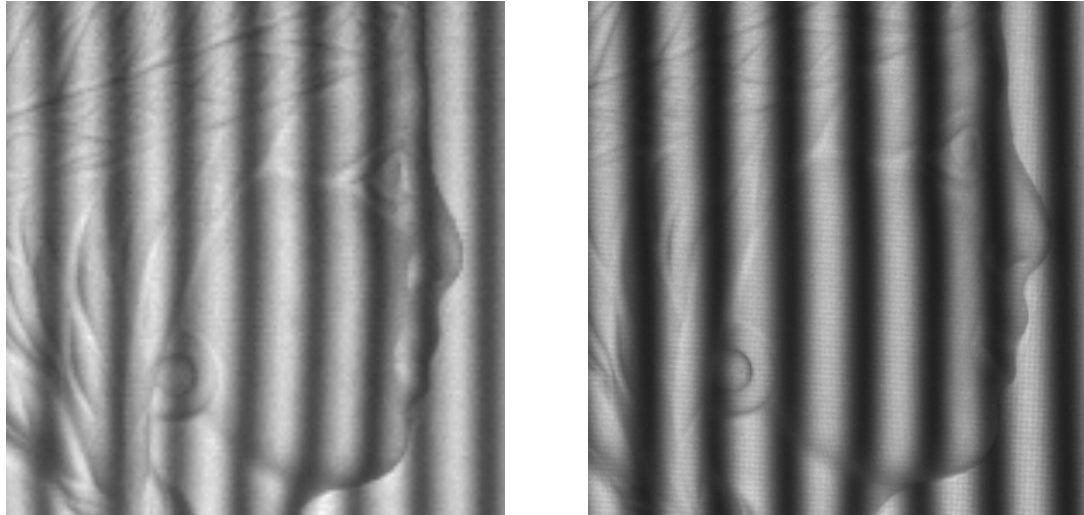


Figure 7.6: Red channels of two color images taken by different color cameras. (a) Image taken by single-CCD camera. (b) Image taken by 3-CCD camera.

7.4 Summery

In this Chapter, a color system composed of two color cameras and one color projector was proposed to further improve the image acquisition speed for the combined phase shifting and stereovision method. With the use of these color devices, only one fringe image is required for each camera to reconstruct a 3D model. As a result, the errors caused by object motions were significantly reduced. Experimental results were presented and compared. Moving objects were measured by different systems to show the resistance of the color system to object motions. The color system has a relatively lower resolution since the color cameras used are single-CCD Bayer cameras. The measurement results can be improved by using more expensive 3-CCD cameras.

Chapter 8 Portable 3D Measurement System

The usual fringe projection systems have a disadvantage that blind areas not captured by cameras or shading areas not illuminated by projection can not be reconstructed. Problems also exist when measuring large objects. When the measured object is larger than the system's field of view, multiple data pieces need to be acquired from different perspectives to cover the whole object. To stitch these data pieces together, registration methods are required

In this Chapter, a portable 3D shape measurement system based on the combined phase shifting and stereovision method is proposed to measure objects with large sizes [96]. Simple registration procedure is also designed for stitching local views.

8.1 Principles

8.1.1 System setup and measurement strategy

The schematic diagram of the system layout is shown in Figure 8.1. The basic system setup is the same as introduced in Section 6.2.1 which includes two B/W cameras, one DLP projector working in B/W mode, and one computer. The visibility-modulated fringe pattern is also utilized.

During the measurement, the projector must be located at the same position and relatively fixed to the object. The two pre-calibrated cameras as a whole part can be moved to as many positions as needed to obtain enough local views that cover the whole

object. Each local view should have overlapping areas with other adjacent views. The 3D models are reconstructed in their own local coordinate systems. The projector is fixed during the measurement procedure, which means that the fringe pattern appearing on the object is not changed, so that the phase and fringe visibility values of the pixels in the overlapped areas is consistent and can be used to find the transformation between the local views. Finally, all of the local views can be transformed into one global coordinate system to form a complete 3D model.

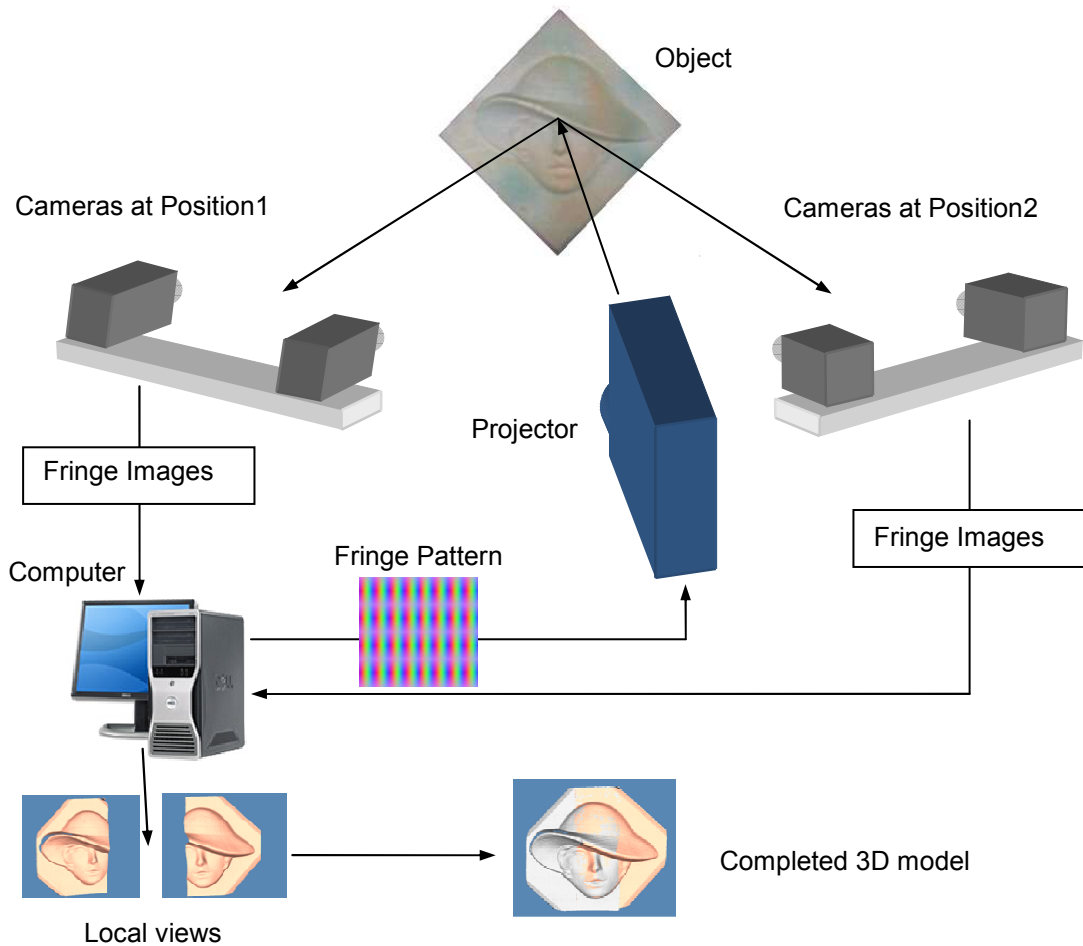


Figure 8.1: Schematic diagram of the portable system.

To build a portable system, the measurement speed needs to be as fast as possible, because any small positional change of the measurement system caused by hand motions during the sequential image acquisition process will result in motion errors in the reconstructed 3D model. By using the visibility-modulated fringe pattern, which is fully introduced in Section 6.3, a local view can be captured in 13.9 ms which is fast enough for the speed requirement.

8.1.2 Data Registration

An efficient data registration procedure is designed to stitch the local views. To show this procedure, a plaster statue of woman face is measured in two views, each containing a different part of the statue with some overlapping areas with the other. The two images shown in Figure 8.2 were taken by the same camera but at different positions. The reconstructed areas for each view are highlighted and the original 3D coordinates are represented in their own local coordinate systems.

The short red line in each image is the centerline detected as a 30 degree phase jump, which is used to calculate the absolute phase map. Since the projector and the object are not moved during the whole procedure, the patterns projected on the object in these two images are identical. With the absolute phase map and the fringe visibility map, the corresponding pixels in the overlapping area could be found (shown as “x” markers in Figure 8.2). Using the phase and fringe visibility values to assist pixel matching, no physical markers or surface textures are required. Once the pixel matching is completed, the 3D point pairs could be used to calculate the transformation between these two local views.

A pattern containing more reference lines, shown in Figure 8.3, is used in order to obtain a wider measurement range for even larger objects. For any two views, if an identical reference line is found, the absolute phase map can be calculated based on that line for stereo matching.

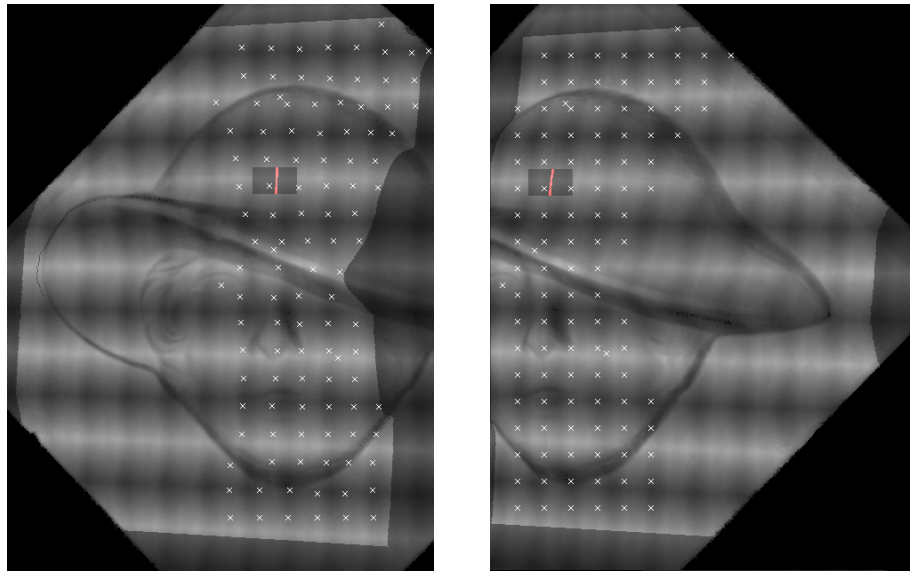


Figure 8.2: Finding corresponding pixel pairs for two local views.

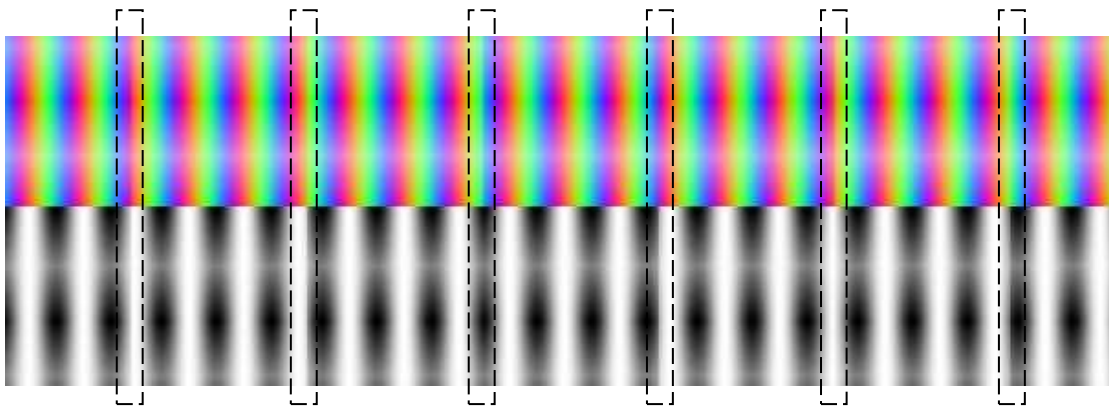


Figure 8.3: Pattern with multiple reference lines.

8.2 Experimental Results

The reconstructed 3D models of the plaster statue are shown in Figure 8.4. Figure 8.4 (a) and (b) are the two local views. Figure 8.4 (c) shows the two local views displayed together before coordinate transformation. Figure 8.4 (d) is the complete 3D model after the coordinate transformation. It can be seen clearly that the two local views have been accurately merged together by using this method.

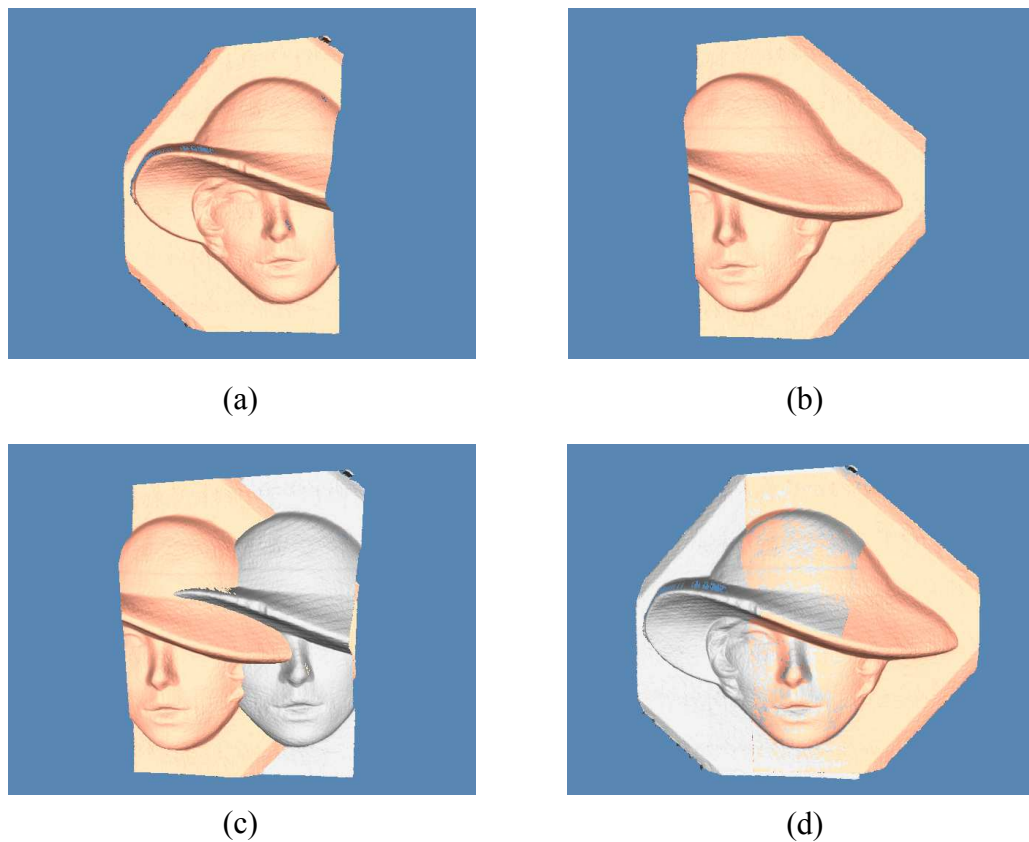


Figure 8.4: Experimental results of a plaster statue. (a) The first local view. (b) The second local view. (c) Local views before coordinate translation. (d) Merged local views after coordinate translation.

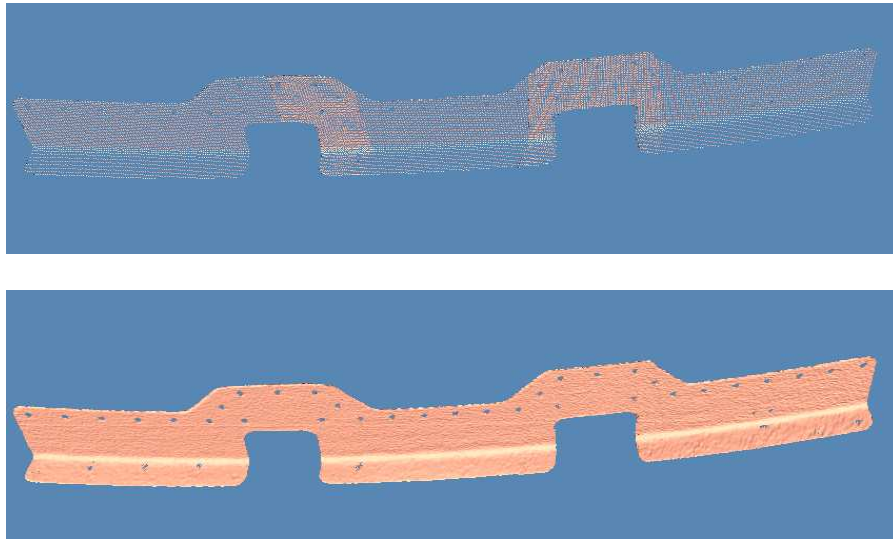


Figure 8.5: Measurement results of a metal part.

Figure 8.5 shows the measurement results of a long metal part. Three local views were taken for this part and the 3D models were transformed into the same global coordinate system. The upper picture shows the point cloud of the three local views, in which the overlapping areas are clearly seen. The lower picture is the stitched 3D model of the whole part.

A plaster seahorse attached to a flat white board was also measured in 9 local views and the results are shown in Figure 8.6. Figure 8.6 (a) shows the point clouds with different local views displayed in different colors. Figure 8.6 (b) is the stitched 3D model. It can be seen that using the proposed registration method, all the pieces can be successfully merged together to form the whole model without the help of any physical

markers or surface textures. Figure 8.6 (c) and (d) are the zoom-in view of the central part and its corresponding position in the whole model.

Finally, Figure 8.7 shows the measurement results of a car fender. Figure 8.7 (a) shows the whole 3D model with colored local views. Figure 8.7 (b) is the whole model displayed in a slightly different angle with the same color. This car fender is painted with diffuse white color, since its original color is black and light reflecting which can not be easily measured by optical techniques.

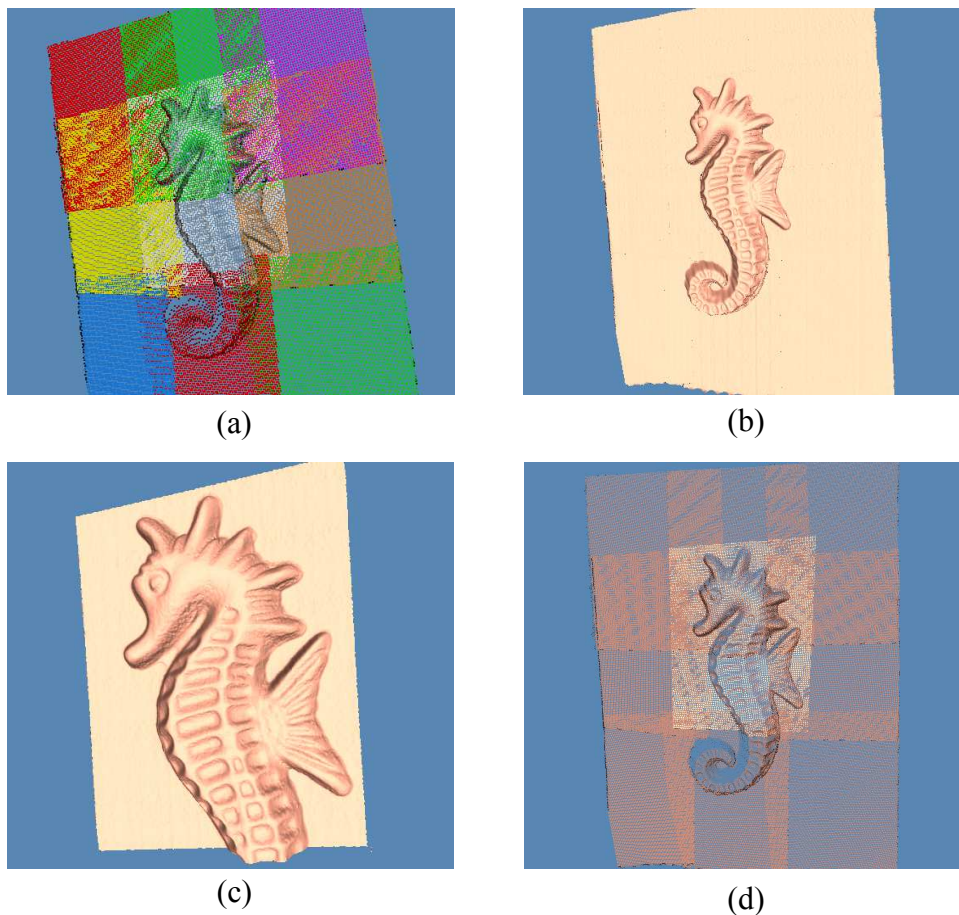


Figure 8.6: Measurement results of a plaster seahorse attached on a flat board. (a) Point clouds of 9 local views. (b) The whole 3D model. (c) The central local view. (d) The central local view in the whole model.

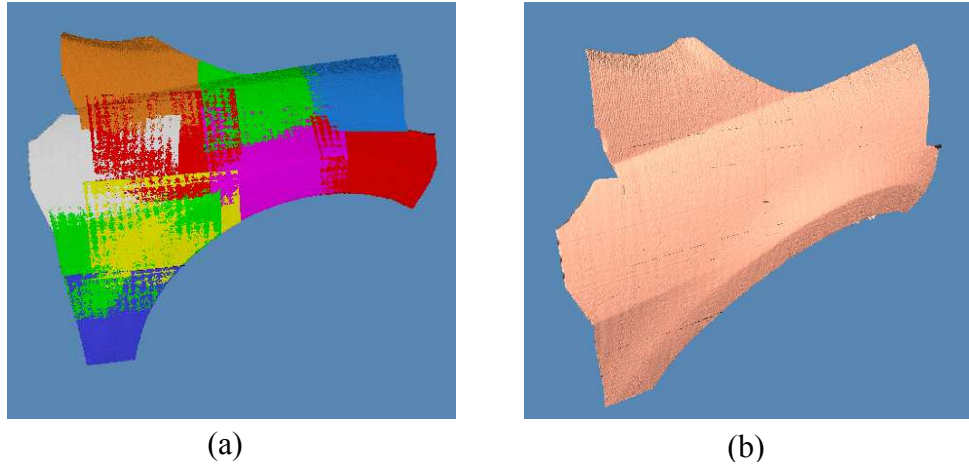


Figure 8.7: Experimental results of a fender. (a) The whole 3D model with colored local views. (b) The whole 3D model shown in one color.

8.3 Summary

In this chapter, we introduced a portable 3D shape measurement system based on the combined phase shifting and stereovision method, which can measure large objects. During the measurement, the movable part is just the two cameras connected by a metal frame, which is small and light enough to be held in hand. The image acquisition time is approximately 13.9 ms for a single local view, which is short enough to avoid motion errors. The coordinate transformations between these local views could be determined by identifying corresponding point pairs in the overlapping areas without the need of any physical markers and surface textures. Several measurement results were presented to show the feasibility of this portable 3D shape measurement system.

Chapter 9 Conclusions and Future Works

9.1 Conclusions

This dissertation research is focused on improving the performance of the 3D shape measurement system. In the first part of this research, nonlinear calibration methods have been developed to improve the accuracy of the 3D shape measurement system based on the phase shifting method. The second-order symmetric radial distortion model, which considers only the first term of radial distortion coefficients, was chosen as the nonlinear camera model. All the intrinsic and extrinsic parameters were calculated based on this model via a Matlab camera calibration toolbox. After applying the nonlinear calibration method on the camera itself, the measurement error caused by lens distortion was reduced by more than 56 percent, particularly, the RMS value was reduced from more than 1.4 mm to approximately 0.61 mm. After applying the nonlinear calibration model on both the camera and the projector, the RMS was reduced to 0.35 mm, which gave a reduction of more than 75 percent.

In order to implement this nonlinear calibration method in real-time measurement system, a marker, which has a slightly different data modulation, was added in the fringe pattern. By using this marker as a reference, the absolute phase value could be calculated based on every three consecutive fringe images. So that, the reconstructed 3D coordinates are absolute 3D coordinates instead of the relative coordinates which was used in the previous real-time system. A sequence of human face expression models were shown as a

sample result of the absolute-coordinates real-time measurement system. A new generation of real-time system was also introduced, which has a higher speed by using new high speed camera. The new camera is faster in speed, simpler in connection and smaller in size. The new system can realize a 60 Hz measurement speed which doubles the previous speed and has a simpler design as well.

To rectify the problem caused by phase ambiguity, the concept of quality map guided phase unwrapping was introduced and a new flood-fill phase unwrapping algorithm was applied to eliminate these ambiguities. The pixels were stored into several groups according to their “qualities”, and then the highest-quality pixels were process first followed by the relatively low-quality pixels, and so on. The 3D “jump” errors caused by phase ambiguities were mostly removed by this new phase unwrapping method.

In the second part of this research, a novel method, namely the combined phase shifting and stereovision method, was proposed for more accurate 3D shape measurement. This method requires the use of two cameras and one projector. The two cameras are set up for stereovision and the projector is used to projecting fringe patterns. Since the two cameras produce phase maps with the same phase errors, any errors due to inaccurate phase measurement could be significantly cancelled. Since the projector no longer takes part in the stereo matching procedure, this method could also help us get rid of the projector calibration, which typically involves a time-consuming and complex procedure,. Experimental results showed that with this new proposed method, the measurement error was reduced by approximately 9 times and the typical periodic errors

due to projector nonlinear gamma curve and huge color contrast was almost completely eliminated.

The use of a visibility-modulated fringe pattern was introduced in the same chapter. The purpose is to reduce the number of fringe images for 3D reconstruction and therefore realize the measurement of moving objects. Experimental results demonstrated that, by using this new fringe pattern, only three images were needed for 3D model reconstruction and the total image acquisition time could be reduced to 13.9ms. Experimental results also showed that with the proposed method, measurement error was reduced by 5 times comparing to the error of the traditional phase shifting method.

A color system based on the combined phase shifting and stereovision method has also been developed to further improve the measurement speed and reduce the motion errors. The special issues, such as color imbalance and color coupling, were solved with proper compensation methods. Measurement results of this color system were compared with the results taken by the B/W system and the traditional phase shifting system. Experiments showed that, the color system is much less sensitive for motions. However, the single-CCD cameras used in this system have lower resolution than the B/W cameras, due to which, the 3D results have relatively rougher surface and less details. Using 3-CCD color cameras can promisingly improve this situation, but that kind of cameras are much more expensive.

Finally, a portable 3D shape measurement system based on the combined phase shifting and stereovision method was introduced, which can measure large objects. During the measurement, the two cameras were moved around the object to obtain as many local views as necessary. The image acquisition time for a local view is

approximately 13.9 ms, which is fast enough to avoid measurement errors caused by slight hand motions. The coordinate transformations between the local views could be determined by identifying corresponding point pairs in the overlapping areas. Without any need of physical markers or surface textures, the registration procedure could be done by the assisting of the fringe patterns and all the local views could be transformed into a common global coordinates system to form a completed 3D model of the whole object. Measurement results were presented to show the feasibility of this system and the proposed registration method.

9.2 Future Works

Besides the topics included in this dissertation, there are still many applications and issues could be further explored. The following are several challenging but potentially feasible ones:

1) Design faster real-time systems

The current B/W real-time system can record video sequences at 60 frames per second, in other words, 180 fringe images are taken per second. To further improve the measurement speed, there are basically two ways. One way is to use color cameras. The pros and cons are discussed in Chapter 7.

The other way is to shrink the image acquisition interval of the B/W system. As can be seen in Figure 4.9, the projection frequency is actually twice the speed as the image acquisition frequency. If we use a camera can capture 360 images per second and synchronize it with the projector in an effective way, higher measurement speed can be achieved. The challenge is that, a projection channel can not be fully captured if we use only one camera, because the camera always needs a short interval between two

exposures. By carefully designing the exposure time, acquisition timing signal and leaving short intervals between two exposures, we can make a partial capture for every projection channel to conquer this challenge.

2) Develop 360 degree measurement system

The portable system introduced in Chapter 8 can measure large objects. However, it can only measure the areas illuminated by the projector. To measure an object in 360 degree, multiple projectors placed around the object are needed to illuminate the whole object. And then the portable system can be moved to take local views all the way around the object. Since the projections may overlap, the projectors need to be turned on and off one by one. Photogrammetry techniques, such as bundle adjustment, can be used for data registration and parameter calculation for more accurate results.

3) Explore more applications

High speed measurement systems have a lot of potential applications. In the past, we have used this kind of systems for medical treatment systems, face and speech recognition and robotic vision. By using tiny acquisition and projection units, the measurement system can be integrated into other mobile devices such as cell phones for further use. There are more and more applications are waiting to be explored with the development of image projection systems, high speed cameras, wireless data transmission, and computer technology, etc.

Bibliography

- [1]F. Chen, G. M. Brown, and M. Song, "Overview of Three-Dimensional Shape Measurement Using Optical Method," *Opt. Eng.* 39(1), pp.10-22 (2000).
- [2]S. Zhang and P. Huang, "High-resolution, real-time three-dimensional shape measurement", *Opt. Eng.* 45(12), 123601(2006).
- [3]Z. Zhang, H. Guo, G. Nejat and P. Huang, "Finding Disaster Victims: A Sensory System for Robot-Assisted 3D Mapping of Urban Search and Rescue Environments", 2007 IEEE International Conference on Robotics and Automation, (10-14), pp. 3889 – 3894 (2007).
- [4]U. Dhond and J. Aggarwal, "Structure from Stereo-A Review," *IEEE Trans. Systems, Man, and Cybernetics* 19(6), pp. 1489-1510 (1989).
- [5]A. Fusiello, V. Roberto, and E. Trucco, "Efficient Stereo with Multiple Windowing," in *IEEE Int'l Conference on Computer Vision and Pattern Recognition*, pp. 858-863 (1997).
- [6] C. Sun, "A Fast Stereo Matching Method," in *Digital Image Computing: Techniques and Applications*, pp. 137-148 (1997).
- [7]J. Weng, N. Ahuia, and T. S. Huang, "Matching Two Perspective Views," *IEEE Trans. on Pattern Analysis and Machine Intelligence* 14, 917-924 (1992).
- [8]P. J. Burt, "The Laplacian Pyramid as a Compact Image Code," *IEEE Trans. on*

Communications 31(4), 532-540 (1983).

- [9] A. Koschan and V. Rodehorst, "Dense Depth Map by Active Color Illumination and Image Pyramids," in *Advances in Computer Vision*, pp. 137-148 (1997).
- [10] L. Zhang, B. Curless, and S. Seitz, "Spacetime Stereo: Shape Recovery for Dynamic Scenes," in *Proc. Computer Vision and Pattern Recognition* (2003).
- [11] I. Moring, H. Ailisto, V. Koivunen and R. Myllyla, "Active 3D vision system for automatic model-based shape inspection," *Opt. Lasers Eng.* 10, 3-4 (1989).
- [12] J. S. Massa, G. S. Buller, A. C. Walker, S. Cova, M. Umasuthan, and A. M. Wallace, "Time of Flight Optical Ranging System Based on Time-Correlated Single-Photo Counting," *Appl. Opt.* 37(31), 7298-7304 (1998).
- [13] T. E. Carlsson, "Measurement of three dimensional shapes using light-in-flight recording by holography," *Opt. Eng.* 32, 2587-2592 (1993).
- [14] N. Abramson, "Time reconstruction in light-in-flight recording by holography," *Appl. Opt.* 30, 1242-1252 (1991).
- [15] B. Nilsson and T. E. Carlsson, "Direct three dimensional shape measurement by digital light-in-flight holography," *Appl. Opt.* 37(34), 7954-7959 (1998).
- [16] C. S. Fraser, "Photogrammetric measurement to one part in a million," *Photogramm. Eng. Remote Sens.* 58(3), 305-310 (1992).
- [17] B. Triggs, P. F. McLauchlan, R. I. Hartley and A. W. Fitzgibbon, "Bundle Adjustment — A Modern Synthesis", *Vision Algorithms'99*, LNCS 1883, 298-372 (2000).

- [18] P. Fua. "Using model-driven bundle-adjustment to model heads from raw video sequences", Proceedings of the 7th International Conference on Computer Vision, pages 46–53, Corfu, Greece, Sept. 1999. IEEE Computer Society Press.
- [19] V. Kirschner, W. Schreiber, R. Kowarschik, and G. Notni, "Self-calibrating shape-measuring system based on fringe projection," Proc. SPIE 3102, 5–13 (1997).
- [20] M. Pollefeys, R. Koch and L. V. Gool, "Self-Calibration and Metric Reconstruction In spite of Varying and Unknown Intrinsic Camera Parameters", International Journal of Computer Vision, Volume 32, Number 1, 7-25 (1999).
- [21] W. Schreiber and G. Notni, "Theory and arrangements of self-calibrating whole-body three-dimensional measurement systems using fringe projection technique", Opt. Eng. 39(1), 159–169 (2000).
- [22] G. Notni, P. Kühmstedt, M. Heinze, and C. Munkelt, , "The concept of virtual landmarks in 3D-multi-view fringe projection", Proc. SPIE 6762, 676208, (2007).
- [23] Z. Ji and M. C. Leu, "Design of Optical Triangulation Devices," Opt. Laser Technology 21(5), 335-338 (1989).
- [24] C. P. Keferstein and M. Marxer, "Testing Bench for Laser Triangulation Sensors," Sens. Rev. 18(3), 183-187 (1998).
- [25] T. Matsumoto, Y. Kitagawa, M. Adachi, and A. Hayashi, "Laser moiré topography for 3D contour measurement," Proc. SPIE 1332, 530–536 (1991).
- [26] J. E. A. Liao and A. S. Voloshin, "Surface topography through the digital enhancement of the shadow moiré," SEM Proc. 506–510 (1990).

- [27] K. Yuen, I. Inokuchi, M. Maeta, S. Manabu, and Y. Masuda, "Dynamic evaluation of facial palsy by moiré topography video: second report," *Proc. SPIE* 2927, 138–141 (1996).
- [28] T. Matsumoto, Y. Kitagawa, and T. Minemoto, "Sensitivity variable moiré topography with a phase shift method," *Opt. Eng.* 35~6!, 1754– 1760 (1996).
- [29] T. Yoshizawa and T. Tomisawa, "Shadow moiré topography by means of the phase shift method," *Opt. Eng.* 32(7), 1668–1674 (1993).
- [30] T. Yoshizawa and T. Tomisawa, "Moiré topography with the aid of phase shift method," *Proc. SPIE* 1554B, 441–450 (1991).
- [31] Y. Z. Dai and F. P. Chiang, "Moiré Interferometry Applied to Topographic Contour Measurement," in *Proc. SPIE*, vol. 954 of *Optical Testing and Metrology II*, pp. 153-157 (1988).
- [32] J. F. Cardenas-Garcia, S. Zheng, and F. Z. Shen, "Projection moiré as a tool for the automated determination of surface topography," *Proc. SPIE* 1554B, 210–224 (1991).
- [33] H. Takasaki, "Moiré topography," *Appl. Opt.* 9, 1467–1472 (1970).
- [34] R. Harding and R. Tait, "Moiré techniques applied to automated inspection of machined parts," in *Proc. SME Vision '86 Conf.*, Detroit, MI (1986).
- [35] B. E. Truax, "Fast Interferometers Bring Precision to Tough Applications," *Photonics Spectra*, 96–99 (1994).
- [36] A. J. P. van Haasteren and H. J. Frankena, "Real-time displacement measurement using a multicamera phase stepping speckle interferometer," *Appl.*

- Opt. 33(19), 4137–4142 (1994).
- [37] K. Bieman and K. Harding, “3D imaging using a unique refractive optic design to combine moiré and stereo,” Proc. SPIE 3204, 2–10 (1997).
- [38] L. H. Bieman, “Survey of Design Consideration for 3D Imaging System,” in Proc. SPIE, vol. 1005 of Optics, illumination, and image sensing for machine vision III, pp. 138-144 (1988).
- [39] K. A. Haines and B. P. Hildebrand, “Contour generation by wavefront construction,” Phys. Lett. 19, 10–11 (1965).
- [40] K. Creath, Y. Y. Cheng, and J. Wyant, “Contouring aspheric surface using two-wavelength phase shifting interferometry,” Opt. Acta 32(12), 1455–1464 (1985).
- [41] Y. Yu, T. Kondo, T. Ohyama, T. Honda, and J. Tsujiuchi, “Measuring gear tooth surface error by fringe scanning interferometry,” Acta Metrol. Sin. 9(2), 120–123 (1986).
- [42] J. Y. Wang, “Imaging laser radar—an overview,” in Proc. 9th Intl. Conf. Laser '86, pp. 19–29 (1986).
- [43] J. C. Marron and K. S. Schroeder, “Three dimensional lensless imaging using laser frequency diversity,” Appl. Opt. 31, 255–262 (1992).
- [44] J. C. Marron and T. J. Schulz, “Three dimensional, fine resolution imaging using laser frequency diversity,” Opt. Lett. 17, 285–287 (1992).
- [45] B. K. P. Horn and M. J. Brooks, Shape from Shading (MIT Press, Cambridge, MA, (1989).
- [46] R. A. Jarvis, “A Perspective on Range Finding Techniques for Computer

- Vision,” IEEE Trans. Pattern Analysis and Machine Intelligence 5(2), 122-139 (1983).
- [47] E. Krotkov, “Focusing”, Int'l J. of Computer Vision 1, 223-237 (1987).
- [48] P. Besl, “Active Optical Range Imaging Sensor,” Machine Vision and Applications 1, 127-152 (1988).
- [49] P. S. Huang, C. Zhang, and F. P. Chiang, “High speed 3D Shape Measurement Based on Digital Fringe Projection,” Opt. Eng. 42(1), 163-168 (2003).
- [50] Huang, P. S., Zhang, S., “Fast three-step phase shifting algorithm”, Appl. Opt. 45, 5086-5091(2006).
- [51] D. Malacara, ed., Optical Shop Testing (John Wiley and Sons, NY, 1992).
- [52] P. Vuylsteke and A. Oosterlinck, “Range Image Acquisition with a Single Binary-Encoded Light Pattern”, IEEE Transactions on Pattern Analysis and Machine Intelligence. 12(2). 148-164 (1990).
- [53] J. L. Posdamer and M. D. Altschuler, “Surface Measurement by Space-encoded Projected Beam Systems,” Computer Graphics and Image Processing 18(1), 1-17 (1982).
- [54] J. Salvi, J. Pages, and J. Batlle, “Pattern codification strategies in structured light systems,” Pattern Recognition 37(4), 827-849 (2004).
- [55] D. Caspi, N. Kiryati, and J. Shamir, “Range Imaging with Adaptive Color Structured Light,” IEEE Trans. on Pattern Analysis and Machine Intelligence 20(5), 470-480 (1998).

- [56] E. Horn and N. Kiryati, "Toward Optimal Structured Light Patterns," *Image and Vision Computing* 17(2), 87-89 (1999).
- [57] J. Pan, P. Huang, and F. Chiang, "Color-coded binary fringe projection technique for 3D shape measurement", *Opt. Eng.* 44(2), 623606 (2005).
- [58] K. G. Harding, "Color encoded moiré contouring", in *Optics, Illumination, and image Sensing for Machine Vision III*, Proc. SPIE 1005, 169-178 (1988).
- [59] L. Zhang, B. Curless, and S. M. Seitz, "Rapid shape acquisition using color structured light and multi-pass Dynamic programming", *3dpvt*, pp.24, First International Symposium on 3D Data Processing Visualization and Transmission (3DPVT'02), (2002).
- [60] M. S. Jeong, and S. W. Kim, "Color grating projection moiré with time-integral fringe capturing for high speed 3D imaging," *Opt. Eng.* 41(8), 1912–1917 (2002).
- [61] J. Pan, P. Huang, and F. Chiang, "Color phase shifting technique for three-dimensional shape measurement", *Opt. Eng.* 45(1), 013602 (2006).
- [62] P. Huang, Q. Hu, F. Jin, and F. Chiang, "Color-encoded digital fringe projection technique for high speed three-dimensional surface contouring", *Opt. Eng.* 38(6), 1065-1071 (1999).
- [63] X. Su, and W. Chen, "Fourier transform profilometry: a review", *Optics and laser in Engineering* 35, 263-284 (2100).
- [64] H. Guo, and P. Huang, "3D shape measurement by use of a modified Fourier transform method," *Proc. SPIE* 7066, 70660E (2008).
- [65] B. Carrihill and R. Hummel, "Experiments with the Intensity Ratio Depth

- Sensor,” *Computer Vision, Graphics and Image Processing* 32, 337-358 (1985).
- [66] G. Chazan and N. Kiryati, “Pyramidal Intensity-Ratio Depth Sensor,” Tech. Rep. No. 121, Israel Institute of Technology, Technion, Haifa, Israel (1995).
- [67] M. Sjudahl and P. Synnergren, “Measurement of shape by using projected random patterns and temporal digital speckle photography,” *Appl. Opt.* 38(10), 1990–1997 (1999).
- [68] Huang, P. S., Zhang, S. and Chiang F., “Trapezoidal phase shifting method for three-dimensional shape measurement”, *Opt. Eng.* 44(12), 123601(2005).
- [69] Z. J. Geng, “Rainbow 3D Camera: New Concept of High speed Three Vision System,” *Opt. Eng.* 35, 376-383 (1996).
- [70] M. Takeda and K. Mutoh, “Fourier Transform Profilometry for the Automatic Measurement of 3D Object Shape,” *Appl. Opt.* 22(24), 3977-3982 (1983).
- [71] S. Rusinkiewicz, O. Hall-Holt, and L. Marc, “Real-Time 3D Model Acquisition,” *SIGGRAPH*, vol. 1281 of 3D acquisition and image based rendering, pp. 438- 446 (ACM Press, 2002).
- [72] O. Hall-Holt and S. Rusinkiewicz, “Stripe Boundary Codes for Real-Time Structured-Light Range Scanning of Moving Objects,” *The 8th IEEE International Conference on Computer Vision*, pp. II: 359-366 (2001).
- [73] R. Legarda-Sáenz, T. Bothe, and W. P. Jäuptner, “Accurate Procedure for the Calibration of a Structured Light System,” *Opt. Eng.* 43(2), 464-471 (2004).

- [74] Q. Hu, P. S. Huang, Q. Fu, , and F. P. Chiang, "Calibration of a 3D Shape Measurement System," *Opt. Eng.* 42(2), 487-493 (2003).
- [75] C. C. Slama, C. Theurer, and S. W. Henriksen, *Manual of Photogrammetry*, American Society of Photogrammetry, 4th ed. (Falls Church, VA, 1980).
- [76] C. S. Fraser, "Photogrammetric Camera Component Calibration: A Review of Analytical Techniques," *Calibration and Orientation of Camera in Computer Vision*, A. Gruen and T. S. Huang, eds., pp. 95-136 (Springer-Verlag, Berlin Heidelberg, 2001).
- [77] F. J. Cuevas, M. Servin, O. N. Stavroudis, and R. Rodriguez-Vera, "Multi-layer Neural Networks Applied to Phase and Depth Recovery From Fringe Patterns," *Opt. Commun* 181(4), 239-259 (2000).
- [78] D. C. Brown, "Close-range Camera Calibration," *Photogrammetric Engineering* 37(8), 855-866 (1971).
- [79] J. Weng, P. Cohen, and M. Herniou, "Camera Calibration with Distortion Models and Accuracy Evaluation," *IEEE Trans. on Pattern Analysis and Machine Intelligence* 14(10), 965-980 (1992).
- [80] W. Faig, "Calibration of Close-range Photogrammetry System: Mathematical Formulation," *Photogrammetric Engineering and Remote Sensing* 41(12), 1479-1486 (1975).
- [81] R. Y. Tsai, "A Versatile Camera Calibration Technique for High-accuracy 3D Machine Vision Metrology using Off-the-shelf TV Camera and Lenses," *IEEE Int. J. Robot. Automat.* RA-3 3(4), 323-344 (1987).

- [82] G. Wei and S. Ma, "Implicit and Explicit Camera Calibration: Theory and Experiments," IEEE Trans. on Pattern Analysis and Machine Intelligence 16(5), 469-480 (1994).
- [83] Zhang, S. and Huang, P. S., "Novel method for structured light system calibration", Opt. Eng. 45(8), 083601(2006).
- [84] Huang, P. S. and Han, X. "On improving the accuracy of structured light systems," Proc. SPIE 6382, 63820H (2006).
- [85] T.E. Choe, I. Cohen, "Registration of multimodal fluoresce in images sequence of the retina," ICCV 2005, pp. 106-113, (2005).
- [86] P. Besl and N. McKay "A method for registration of 3D shapes," IEEE Transactions on Pattern Analysis and Machine Intelligence, 14(2) pp.239-255, (1992).
- [87] M. Halioua, R. S. Krishnamurthy, H. C. Liu, and F. P. Chiang, "Automated 360° profilometry of 3D diffuse objects," Appl. Opt. 24, 2193–2196 (1985).
- [88] X. X. Cheng, X. Y. Su, and L. R. Guo, "Automated measurement method for 360° profilometry of diffuse objects," Appl. Opt. 30, 1274–1278 (1991).
- [89] C. Reich, R. Ritter, and J. Thesing, "3D shape measurement of complex objects by combining photogrammetry and fringe projection", Opt. Eng. 39(1), 224-231(2000).
- [90] D. C. Ghiglia and M. D. Pritt, Two-Dimensional Phase Unwrapping: Theory, Algorithms, and Software (John Wiley and Sons, Inc, 1998).
- [91] S. Zhang and P. Huang, "Phase error compensation for a 3D shape

measurement system based on the phase shifting method”, Opt. Eng. 46(6), 063601(2007).

- [92] S. Zhang and S. Yau, “Generic nonsinusoidal phase error correction for three-dimensional shape measurement using a digital video projector”, Appl. Opt. (46), 36-43(2007).
- [93] X. Han and P. Huang, "Combined phase shifting and stereovision method: a new approach for 3D shape measurement," Proceedings of SPIE Vol. 7389, 7389-125 (2009).
- [94] X. Han and P. Huang, "Combined phase shifting and stereovision method: use of a visibility-modulated fringe pattern," Proceedings of SPIE Vol. 7389, 7389-131 (2009).
- [95] X. Han and P. Huang, "Combined Phase shifting and stereovision Method: Use of a Color Visibility-Modulated Fringe Pattern," Proceedings of SPIE Vol. 7432, 7432-32 (2009).
- [96] X. Han and P. Huang, "A Portable 3D Shape Measurement System Based on the Combined Phase shifting and stereovision Method," Proceedings of SPIE Vol. 7432, 7432-36 (2009).